2017

Evaluation Of Multicarrier Air Interfaces In The Presence Of Interference For L-Band And C-Band Air-Ground Communications

Hosseinali Jamal
University of South Carolina

Recommended Citation

Jamal, H.(2017). *Evaluation Of Multicarrier Air Interfaces In The Presence Of Interference For L-Band And C-Band Air-Ground Communications.* (Doctoral dissertation). Retrieved from https://scholarcommons.sc.edu/etd/4456

EVALUATION OF MULTICARRIER AIR INTERFACES IN THE PRESENCE OF INTERFERENCE FOR L-BAND AND C-BAND AIR-GROUND COMMUNICATIONS

by

Hosseinali Jamal

Bachelor of Science
Tafresh University, 2008

Master of Science
Shahid Beheshti University, 2012

Submitted in Partial Fulfillment of the Requirements

For the Degree of Doctor of Philosophy in

Electrical Engineering

College of Engineering and Computing

University of South Carolina

2017

Accepted by:

David Matolak, Major Professor

Mohammod Ali, Committee Member

Srihari Nelakuditi, Committee Member

Xiaofeng Wang, Committee Member

Cheryl L. Addy, Vice Provost and Dean of the Graduate School

DEDICATION

I dedicate my dissertation work to my family. A special feeling of gratitude to my loving parents, Moloud and Hassan Jamal whose words of encouragement and push for tenacity ring in my ears. My sisters Narges, Neda and Nadia and my brother Farzin have never left my side and are very special. I also dedicate this dissertation and give special thanks to my advisor Dr. David Matolak.

ACKNOWLEDGEMENTS

First I wish to thank my committee members who were more than generous with their expertise and precious time. Thank you Dr. Mohammod Ali, Dr. Srihari Nelakuditi, and Dr. Xiaofeng Wang for agreeing to serve on my committee. A special thanks to Dr. David Matolak, my major professor for his countless hours of reflecting, reading, encouraging, and most of all patience throughout my entire study. I would also like to thank Dr. Ruoyu Sun for his collaboration during some part of my studies. Their excitement and willingness to provide feedback made the completion of this research and dissertation an enjoyable experience.

ABSTRACT

The use of aeronautical vehicles and systems is continuously growing, and this means current aeronautical communication systems, particularly those operating in the very high frequency (VHF) aviation band, will suffer from severe congestion in some regions of the world. For example, it is estimated that air-to-ground (AG) communication traffic density will at least double by 2035 over that in 2012, based on the most-likely growth scenario for Europe. This traffic growth (worldwide) has led civil aviation authorities such as the FAA in the USA, and EuroControl in Europe, to jointly explore development of future communication infrastructures (FCI). According to international aviation systems policies, both current and future AG communication systems will be deployed in L-band (960-1164 MHz), and possibly in C-band (5030-5091 GHz) because of the favorable AG radio propagation characteristics in these bands. During the same time period as the FCI studies, the use of multicarrier communication technologies has become very mature for terrestrial communication systems, but for AG systems it is still being studied and tested.

Aiming toward future demands, EuroControl and FAA sponsored work to define several new candidate AG radio systems with high data rate and high reliability. Dominant among these is now an L-Band Digital Aeronautical Communication Systems (L-DACS): L-DACS1. L-DACS1 is a multicarrier communication system based on the popular orthogonal frequency division multiplexing (OFDM) modulation technique. For airport surface area communication systems used in C-band, EuroControl and FAA also proposed another OFDM communication system based on the IEEE 802.16e standard, termed aeronautical mobile airport communication system (AeroMACS). This system has been proposed to provide the growing need of communication traffic in airport environments.

In this dissertation, first we review existing and proposed aviation communication systems in VHF-band, L-band and C-band. We then focus our study on the use of multicarrier techniques in these aviation bands. We compare the popular and dominant multicarrier technique OFDM (which is used in cellular networks such long-term evolution (LTE) and wireless local area networks such as Wi-Fi) with the filterbank multicarrier (FBMC) technique. As far as we are aware, we are the first to propose and evaluate FBMC for aviation communication systems.

We show, using analysis and computer simulations, along with measurement based (NASA) air-ground and airport surface channel models, that FBMC offers advantages in performance over the OFDM schemes. Via use of sharp filters in the frequency domain, FBMC reduces out of band interference. Specifically, it is more robust to high-power distance measurement equipment (DME) interference, and via replacement of guard bands with data-bearing subcarriers, FBMC can offer higher throughput than the contending L-DACS1 scheme, by up to 23%. Similar advantages over AeroMACS pertain in the airport surface channel. Our FBMC bit error ratio performance is comparable to that of the OFDM schemes, and is even better for our “spectrally-shaped” version of FBMC. For these improvements, FBMC requires a modest complexity increase.

Our final contribution in this dissertation is the presentation of spectrally shaped FBMC (SS-FBMC). This idea allocates unequal power to subcarriers to contend with non-white noise or non-white interference. Our adaptive algorithm selects a minimum number of guard subcarriers and then allocates power accordingly to remaining subcarriers based on a “water-filling-like” approach. We are the first to propose such a cognitive radio technique with FBMC for aviation applications. Results show that SS-FBMC improves over FBMC in both performance and throughput.

TABLE OF CONTENTS

LIST OF TABLES

LIST OF FIGURES

LIST OF ABBREVIATIONS

1090ES	1090 MHz Extended Squitter
AAC	Airline Administrative Control
ACARS	Aircraft Communications Addressing and Reporting System
ACI	Adjacent Channel Interference
ADC	Analog-to-Digital
ADL	Airport Data Link
ADS-B	Automatic Dependent Surveillance Broadcast
AG	Air-to-Ground
AM	Amplitude Modulation
AMCP	Aeronautical Mobile Communications Panel
AeroMACS	Aeronautical Mobile Airport Communication System
AOC	Aeronautical Operational Control
APNT	Alternative Positioning, Navigation, and Timing
ASA	Airport Surface Area
A-SMGCS	Airport Surface Movement Guidance and Control System
ATC	Air Traffic Control
ATM	Air Traffic Management
ATS	Air Traffic Services
AWGN	Additive White Gaussian Noise
B-AMC	Broadband Aeronautical Multi-carrier Communications System

BER	Bit Error Ratio
BS	Base Station
BW	Bandwidth
B-VHF	Broadband VHF System
CC	Common Control
CC	Correlation Coefficient
CCDF	Complementary Cumulative Distribution Function
CDMA	Code Division Multiple Access
CE2R	Curved Earth Two Ray
CFR	Code of Federal Regulations
CIM	Correlative Interference Mitigation
CIR	Channel Impulse Response
CNPC	Control and Non-Payload Communications
CPM	Continuous Phase Modulation
CP-OFDM	Cyclic Prefix OFDM
CR	Cognitive Radio
D8PSK	Differential 8-phase Shift Keying
DAC	Digital-to-Analog
dBi	Decibels Relative to Isotropic Antenna Gain
dBm	Decibels Above one milliwatt
DC	Dedicated Control
DLR	German Aerospace Center
DME	Distance Measuring Equipment

DPPs	Deformed Pulse Pairs
DSB-AM	Double-Sideband Amplitude Modulation
EIA	Electronic Industry Association
EU	European Union
FAA	Federal Aviation Administration
FCI	Future Communication Infrastructures
FE2R	Flat Earth Two Ray
FFB	Fast Filter Bank
FFT	Fast Fourier Transform
FIR	Finite Impulse Response
FL	Forward Link
FBMC	Filterbank Multicarrier
FDD	Frequency-Division Duplexing
FDM	Frequency Division Multiplexing
FT	Flight Track
GMSK	Gaussian Minimum Shift Keying
GPS	Global Positioning System
GS	Ground Site
GS	Ground Station
GSM	Global System for Mobile Communications
HPA	High-Power Amplifier
ICAO	International Civil Aviation Organization
ICI	Inter-Carrier Interference

IFFT	Inverse Fast Fourier Transform
IOTA	Isotropic Orthogonal Transform Algorithm
ISI	Inter-Symbol Interference
ITU	International Telecommunication Union
IMPC	Intermittent Multipath Components
L-DACS	L-Band Digital Aeronautical Communication Systems
L-DACS1	L-band Digital Aeronautical Communication System of Type 1
L-DACS2	L-band Digital Aeronautical Communication System of Type 2
LNA	Low-Noise Amplifier
LOS	Line of Sight
LS	Least-Square
Long-Term Evolution	LTE
MC	Multi-Carrier
MC-CDMA	Multi-Carrier Code Division Multiple Access
MIA	Miami International Airport
MIMO	Multiple Input, Multiple Output
MISO	Multiple Input, Single Output
MLS	Microwave Landing System
MRC	Maximal Ratio Combining
MSK	Minimum-Shift Keying
NASA	National Aeronautics and Space Administration
NextGen	Next Generation Air Transportation System
NLOS	Non-Line-of-Sight

OFDMA	Orthogonal Frequency-Division Multiple Access
OOB	Out-of-Band
OQAM	Offset QAM
P34	Project 34
PAM	Pulse Amplitude Modulated
PAPR	Peak to Average Power Ratio
PB	Pulse Blanking
PDP	Power Delay Profile
PHY	Physical-Layer
ppps	Pulse Pairs Per Second
PSD	Power Spectral Density
QAM	Quadrature Amplitude Modulated
QPSK	Quadrature Phase Shift Keying
RC	Raised Cosine
Ref	Reflected
RL	Reverse Link
RMS-DS	Root Mean Square Delay Spread
RRC	Root Raised Cosine
RTCA	Radio Technical Commission for Aeronautics
SD	Stationarity Distance
SEM	Spectrum Emission Mask
SESAR	Single European Sky ATM Research
SIMO	Single Input, Multiple Output

SINR	Signal-to-Interference plus Noise Ratio
SIR	Signal-to-Interference Ratio
SMT	Staggered Modulated Multitone
SNR	Signal-to-Noise Ratio
SS-FBMC	Spectrally Shaped FBMC
SSR	Secondary Surveillance Radar
TDD	Time-Division Duplexing
TDL	Tapped Delay Line
TDMA	Time Division Multiple Access
TIA	Telecommunications Industry Association
TMA	Terminal Management Area
UAS	Unmanned Aircraft Systems
UAT	Universal Access Transceiver
Tx	Transmitter
VDL	VHF Digital Link
VHF	Very High Frequency
VSB	Vestigial Side-Band
WiMAX	Worldwide Interoperability for Microwave Access
WRAN	Wireless Regional Area Networks

CHAPTER 1

INTRODUCTION

1.1 BACKGROUND: AIR-TO-GROUND AND AIRPORT SURFACE COMMUNICATION SYSTEMS

Air traffic is continuing to grow. Safely managing significantly larger air traffic densities in the future will require more capable communication systems. One of the best known—but certainly not the only aeronautical communication system—is the system used for air traffic control (ATC). Communications between air traffic controllers and pilots currently use the VHF aeronautical band. These links use Double-Sideband Amplitude Modulation (DSB-AM) and are deployed in the VHF aviation band from 118 to 137 MHz (only 19 MHz entire world). This band is becoming very congested in many busy airspace segments worldwide. Thus, civil aviation authorities recognized the need to look for additional or alternative spectral bands for handling a larger amount of communication traffic in the future. The nearly daily increase of air traffic and associated AG communication system traffic makes it inevitable to require new technologies and communication techniques in future AG communication systems.

Multi-carrier (MC) modulations have been shown to be promising candidates to obtain high data rate transmission in frequency selective and time varying channels, so various organizations have begun studies of these for the AG application. Within the European Commission co-funded project B-VHF (Broadband VHF System), a complete design for a so-called overlay system for the VHF-band based on multi-carrier technology has been developed, investigated, and demonstrated. An overlay system operates simultaneously with the existing legacy VHF systems, sharing portions of the aeronautical VHF spectrum. As a result of this activity, B-VHF has been recognized as a promising technology within the FCI study that was jointly performed by Federal Aviation Administration (FAA) and EUROCONTROL.

Today's narrowband VHF technologies are using the VHF spectrum allocated for aeronautical safety communications in a highly inefficient manner. Air-traffic control to pilot communication employs analog AM with "manual" channel allocation via frequency division multiplexing (FDM). The B-VHF project investigated the feasibility of broadband MC technology combined with code division multiple access (CDMA) for VHF aeronautical communications. The high-level goal of the B-VHF project was to prove the feasibility of the broadband MC-CDMA technology and demonstrate the benefits of this technology to the aeronautical community. The preferred B-VHF deployment concept anticipates that the new system would be initially operated in parallel with the legacy narrowband VHF systems, virtually using the same part of the VHF spectrum without inter-system interference and without requiring additional spectral resources [1].

The FCI concept jointly developed by FAA and EUROCONTROL foresees the VHF-band as the primary means to support ATC voice communication. Future aeronautical data link communication, however, shall be preferably implemented in the L-band. Based on this reasoning, EUROCONTROL tasked the B-AMC (Broadband Aeronautical Multi-carrier Communications System) consortium to adapt the B-VHF system to L-band use and perform investigations to determine if and how a possible B-

VHF like system could be operated in L-band. The system design for this L-band MC system is described in [2]. B-AMC is based on frequency-division duplexing (FDD) and uses orthogonal frequency-division multiple access (OFDMA) technique instead of MC-CDMA. As part of our work in this dissertation we investigate the potentials of MC systems in C-band both in airport surface or AG mode communications.

As an extension of B-AMC systems, L-DACS1 was proposed as an L-band AG multicarrier system partly based on successful terrestrial broadband MC communication systems such as WiMAX. L-DACS1 uses cyclic prefix OFDM (CP-OFDM) technique. CP-OFDM is an efficient MC modulation technique to combat multi-path fading channels. Technical details will be described in next chapter. L-DACS1 robustness comes from adding guard intervals in the time and frequency domains to combat ISI due to multi-path fading, and Doppler shifts and adjacent channel interference, respectively, but these guard intervals decrease spectral efficiency. In L-DACS1 the time duration of symbols is extended by a significant fraction of the useful symbol time for insertion of a cyclic prefix, and a large number of subcarriers are used as guard bands, which further decreases the AG communication system spectral efficiency. This observation brought the idea of using new technologies and modulation techniques to cope with the challenges of deploying L-DACS1. Disadvantages of L-DACS1 are its relatively low spectral efficiency and high out-of-band (OOB) power, and its low resistance to the OOB power emissions from interference signals, especially DME.

In the quest for better multicarrier modulation schemes for AG systems, we studied FBMC [3], [4] and showed its significant advantages when applied to AG communication systems. The FBMC technique was invented many years ago [5], [6], but has seen renewed interest in recent years because of technological advances and for some of its favorable properties. These properties include very low OOB power and consequent higher spectral efficiency when the number of guard subcarriers is reduced. The lower OOB power makes it more robust in the presence of (adjacent-channel) interference signals such as DME. In our FBMC systems we based the designs on L-DACS1. Our FBMC AG communication systems satisfy essentially all the requirements of L-DACS1. The FBMC systems have similar physical layer parameters as L-DACS1 (e.g., equal total number of subcarriers, subcarrier spacing, and total bandwidth, total transmit power, etc.). The main difference between FBMC and L-DACS1 is the use of prototype filters on each subcarrier; use of this filtering technique produces all the FBMC advantages. The main drawback of FBMC is its complexity: because of the more complex filtering processing at all subcarriers, complexity is larger than that of L-DACS1. Yet in FBMC by using polyphase network technique we can reduce the complexity significantly, but still it is in the order of four times higher than CP-OFDM techniques such as L-DACS1. But by today's faster processors the complexity of using FBMC is a minor issue.

Airport surface areas (ASAs) also have seen significant growth in traffic and communication needs. A key early work in the area of ASA networking is [7]. This NASA report compared multiple candidate technologies for a range of applications and multiple frequency bands. In [7] the IEEE 802.16e [8] standard technologies were identified as being well-suited to ASA networking due to their flexibility, high data rates, range of selectable bandwidths, and other features. The IEEE 802.16 wireless standard is also known as WiMAX. Since 2010, the Radio Technical Commission for Aeronautics (RTCA) has developed a version of the 802.16 standard specifically tailored for airport operation [9]. This "aviation profile" defines specifics of the 802.16e standard for airport surface use, and is denoted AeroMACS [26]-[28].

Although AeroMACS has been rapidly expanding worldwide, as in other areas of communication, such as cellular, new developments and improvements continue. For cellular, so called 5th generation (5G) systems are being planned. These new systems aim at improving spectral efficiency and increasing data rate via multiple techniques, including large antenna arrays, new spectral allocations, and new physical-layer (PHY) techniques [10]. It is the latter area we consider here for the ASA. Therefore in this dissertation, we also consider the use of more spectrally-efficient FBMC instead of the OFDM employed in AeroMACS.

Regarding ASA systems, worth noting is in early stages of ASA communication system studies, the suitability of the microwave landing system (MLS) extension band (E-MLS) from 5.091-5.15 GHz was studied for airport mobile networking. This was also considered at a prior World Radio Conference. The MLS was designed for the terminal management area (TMA) and airport surface applications. The MLS is an all-weather, precision radio guidance system used at some large airports to assist aircraft in landing. It provides information about the aircraft approach azimuth, optimal angle of descent and the distance, as well as data about the reverse course in case of an unsuccessful landing approach. The advancement of the GPS satellite navigation was the reason the MLS installation of new devices halted and finally in 1994 completely canceled by the FAA. MLS installations are still operating at various airports throughout the world, but they are somewhat rare. Hence this E-MLS band is being used for AeroMACS, and would also be used for any new systems that might supplement or replace AeroMACS. As part of C-band investigations we also design similar technique communication systems based on CP-OFDM and FBMC with 5 MHz bandwidth. We named the CP-OFDM C-band system C-DACS which has the same subcarrier spacing and total symbol length as L-DACS1. And we also designed similar FBMC based system as C-DACS for C-band. We will explain C-DACS and C-band FBMC systems later in detail.

1.2 L-BAND AND C-BAND AERONAUTICAL COMMUNICATION SYSTEMS CHALLENGES AND NEW SOLUTIONS

In 2002 the International Civil Aviation Organization (ICAO) recognized the need to improve the aeronautical communication system for air traffic management (ATM) and air traffic control (ATC) in civil aviation communication systems [11]. After this, both American and European researchers in industry and universities began to develop plans for new aeronautical communication systems in support of ICAO to develop the so-called FCI. The FCI comprises several links, including air to ground and satellite communication links, and may later include air to air communication. Initially the development of the FCI was part of two programs: the Single European Sky ATM Research (SESAR) supported by EUROCONTROL, the European Union (EU), and the Next Generation Air Transportation System (NextGen), led by the US Federal Aviation Administration (FAA) and supported by the National Aeronautics and Space Administration (NASA) [11]. Significant changes in aviation technology have historically taken place *much* more slowly than in commercial and consumer applications, hence technologies for FCI are still being researched and developed today. Traditionally, developing AG communication systems depends on the accessibility of available spectrum. It is expected that at least some future AG communication systems will be deployed in the L-band (960-1164 MHz), allocated by the International Telecommunication Union (ITU).

Here we describe the L-band spectrum and the communication and navigation systems allocated in the aeronautical L-band, with which any L-DACS or FBMC system must coexist. Figure 1.1-a shows the overall view of the current communication systems that use the L-band. As noted, it was decided to allocate the L-DACS channels in an "inlay" approach with respect to the existing DME system (Figure 1.1-b). This means that L-DACS channels lie *between* DME channels in frequency. As we see in Figure 1.1-a, major portions of this L-band spectrum have been allocated to the DME signals. DME signals are used for radio navigation purposes, and they are still being studied as the main candidate for future Alternative Positioning, Navigation, and Timing (APNT) systems (where "alternative" here means alternative to GPS) [12]. Each DME channel has a 1 MHz bandwidth (BW), and the DME signal is generated using Gaussian shaped pulses. In Figure 1.1-a, there are also additional transponder systems known as legacy systems: secondary surveillance radar (SSR), Universal Access Transceiver (UAT), Galileo/GPS satellite signals. Any new FCI system must inter-operate with these systems.

For flight safety, the FCI candidate systems must be able to operate in the presence of interference from all these systems, and also cause minimum interference to these existing systems. Since DME is the dominant communication system in this band, in this dissertation we concentrate on DME as the main interfering signal to the studied L-band communication systems.

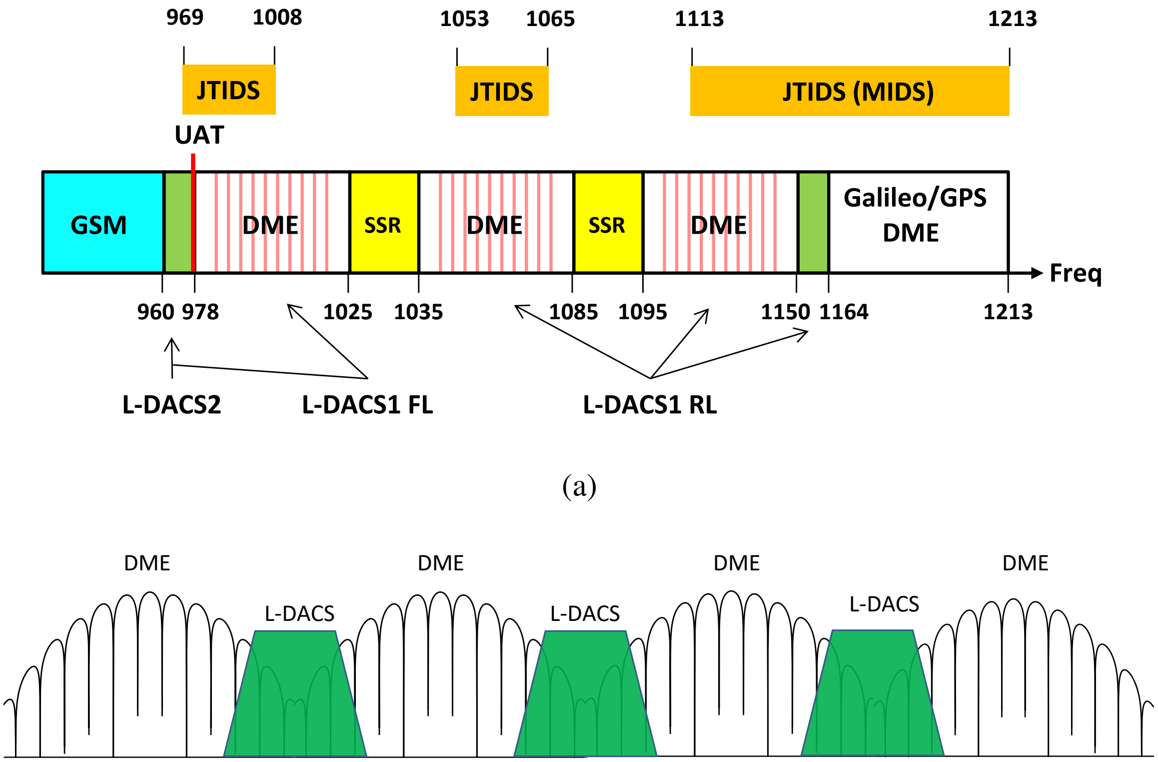

(a)

(b)

Figure 1.1. L-band systems spectral occupancy, (a) Overall view, (b) L-DACS inlay diagram (between DME channels).

As mentioned, there are at present two FCI proposals for this L-band spectral region, L-DACS1 [13] and L-DACS2 [14]. These waveforms may also be used for unmanned aircraft systems (UAS) which are seeing explosive growth in both commercial and consumer use. These UAS have a large variety of applications, and integration of them into the worldwide airspace will require reliable and spectrally-efficient waveforms. As noted, the L-DACS1 system is similar to IEEE 802.16 and the physical layer is based on the CP-OFDM modulation technique.

L-DACS2 is a single carrier communication system similar to the GSM, the physical layer of which uses Gaussian Minimum Shift Keying (GMSK) modulation. In-depth studies have been done to compare L-DACS1 and L-DACS2 [15]-[23]. In this dissertation we also study and compare L-DACS2 systems' physical layer performance with our new FBMC designs.

C-band aeronautical communication systems have also been studied and adapted for AG communication systems, especially for airport surface communications purposes. In next chapter we will provide a review of existing and proposed, and our new L-band and C-band systems, and the potentials of using new waveform such as FBCM in this band.

1.3 DISSERTATION OBJECTIVES

In this section, a list of the dissertation objectives is presented.

1. [Chapter 2] Perform a literature review of air-to-ground communication systems in VHF, L-band and C-band. In this chapter we provide a table and list all existing or proposed communication systems in these bands.
2. [Chapter 3] Describe the details about the AG environments and communication systems channels. We also provide more technical information about FCI systems in this chapter.
3. [Chapter 4] In chapter 4 we compare L-DACS and FBMC and the performance of their C-band counterparts in different AG channel environments. We provide simulation results of the performance of the L-band systems as the scenario of being transmitted between DME channels to see the DME interference impact on their performance. We also study the cellular concept of AG communication systems at L-band by providing an example based on real scenario with multiple existing DME channels.

4. [Chapter 5] Chapter 5 contains some part of our work to study the potentials of using dual antenna multicarrier communication system in L-band.
5. [Chapter 6] In this chapter we investigate the FBMC system proposal for airport surface environment and compare it with current communication standard; AeroMACS.
6. [Chapter 7] In chapter 7 we show the details and results of our spectrally shaped FBMC system as part of performance enhancement of our conventional FBMC system in non-white noise situation across the channel (such as coexistent with DME channels as inlayed scenario). In this chapter we also study the potentials of using SS-FBC as a cognitive radio approach for AG systems.
7. [Chapter 8] Chapter 8 contains the conclusions and future work.

1.4 DISSERTATION CONTRIBUTIONS

The project "Unmanned Aircraft Systems (UAS) Research: The AG Channel, Robust Waveforms, and Aeronautical Network Simulations," started in 2011 and ended in 2016. We have 1 published IEEE journal paper and 11 conference papers published or submitted[1]. Currently we are working on another journal paper which will contain some part of the results in the final chapter. In addition to the NASA project, I have three papers focusing on FBMC and cognitive radio systems.

[J1] **H. Jamal**, D.W. Matolak, "FBMC and LDACS Performance for Future Air to Ground Communication Systems," *IEEE Transactions on Vehicular Technology*, vol. 66, no. 99, pp. 5043-5055, June 2017.

[C1] **H. Jamal**, D. W. Matolak, "Spectrally Shaped Filter Bank Multicarrier Systems for

---

[1] The notation J denotes journal paper, C denotes conference paper.

L-band Aeronautical Communication Systems," *IEEE Aerospace Conference*, pp. 1-15, Big Sky, MT, 4-11 March, 2017.

[C2] **H. Jamal**, D. W. Matolak, "Performance of L-band Aeronautical Communication System Candidates in the Presence of Multiple DME Interferers," *IEEE/AIAA 35th Digital Avionics Systems Conference* (DASC), Sacramento, CA, September, 2016. **(*Won the best of session paper award*).**

[C3] **H. Jamal**, D. W. Matolak, "Multicarrier Air to Ground MIMO Communication System Performance," *IEEE 84th Vehicular Tech. Conference* (VTC Fall), Montréal, September, 2016.

[C4] **H. Jamal**, D. W. Matolak, "Channel Estimation in an Over-water Air-Ground Channel Using Low Complexity OFDM-OQAM Modulations," *IEEE Consumer Communications and Networking Conference* (CCNC), Las Vegas, NV, USA, 13-17 January, 2016.

[C5] **H. Jamal**, D. W. Matolak, R. Sun "Comparison of LDACS and FBMC Performance in Over-Water Air-Ground Channels," *IEEE/AIAA 34th Digital Avionics Systems Conference* (DASC), pp. 2D6-1-2D6-9, Prague, CZ, 13-17 September, 2015.

[C6] **H. Jamal**, D. W. Matolak, R. Sun "Enhanced Airport Surface Multi-carrier Communication Systems: Filterbank Advantages over AeroMACS OFDM," *IEEE Military Communications Conference (MILCOM)*, Baltimore, MD, October 2017.

[C7] D. W. Matolak**,** R. Sun, **H. Jamal**, W. Rayess, "L- and C-Band Airframe Shadowing Measurements and Statistics for a Medium-Sized Aircraft," *11th European Conference on Antennas and Propagation* (EuCAP), pp. 1429-1433, Paris, 19-24 March 2017.

[C8] N. Schneckenburger, T. Jost, U. G. Fiebig, G. D. Galdo, **H. Jamal**, D. W.

Matolak, R. Sun, “Modeling the Air-Ground Multipath Channel,” *11th European Conference on Antennas and Propagation (EUCAP)*, pp. 1434-1438, Paris, France, 19-24 March 2017.

[C9] N. Schneckenburger, et al. “A Geometrical-Statistical Model for the Air-Ground Channel”, to appear, *IEEE/AIAA 36th Digital Avionics Systems Conference* (DASC), 17-21 September, St. Petersburg, FL, USA, 2017. **(*Won the best of session paper award*).**

[C10] D. W. Matolak, **H. Jamal**, R. Sun, “Spatial and Frequency Correlations in Two-Ray Air-Ground SIMO Channels”, *IEEE International Conference on Communications* (*ICC*), Paris, France, 21-25 May 2017.

[C11] D. W. Matolak, **H. Jamal**, “Aviation Multicarrier Communication System Performance in Several 5 GHz Band Air-Ground Channels”, submitted to *IEEE 87th Vehicular Tech. Conference* (*VTC-Spring*)*, Porto, Portugal, 3–6 June, 2018.*

CHAPTER 2

AIR-TO-GROUND COMMUNICATION SYSTEMS LITERATURE REVIEW

2.1 VHF AND L-BAND AG COMMUNICATION SYSTEMS

Some of the typical air-ground aeronautical communications systems and technologies are listed in Table 2.1. The aircraft communications addressing and reporting system (ACARS) may be viewed as one of the pioneers for modern AG communications systems. It was developed in 1978 to be used in the very high frequency (VHF) band. Its modulation technique is amplitude modulation (AM) [29]. It was implemented to transmit voice signals over radios with bandwidth of approximately 3 kHz and to provide communications for flight services and operational activities such as air traffic control (ATC), aeronautical operational control (AOC), and airline administrative control (AAC) system functions.

Table 2.1. Typical Air-Ground Aeronautical Communication, Navigation, and Surveillance Systems.

Name	**Band**	**BW**	**Modulation/ Multiple Access**	**Data Rates**	**Designer**	**Year**	**Comments**
Distance Measuring Equipment (DME) [36]	L-band, 960-1215 MHz	1 MHz/ channel	Gaussian shaped pulses	50-3600 pulse pairs per second (ppps)	Invented by James Gerrand	1950s	Transponder-based radio navigation technology that measures slant range distance
ATC Voice	VHF, 118-137 MHz	8.22 or 25 kHz (760 channels each 25 kHz)	Analog AM				Push to talk system for voice and air traffic control (ATC)
Aircraft Communications Addressing and Reporting (ACARS) [29]	VHF, 118-137 MHz	3 kHz/ channel	AM and Minimum-Shift Keying (MSK)	2.4 kbps	ARINC Inc. (now part of Rockwell Collins Inc.)	1978	A pioneer “modern” aeronautical communication system

VHF Digital Link (VDL) Mode 2,3 and 4 [31]	VHF, 118-137 MHz	19 MHz (25kHzX760 channels)	D8PSK/ TDMA	31.5 kbps	Aeronautical Mobile Communications Panel (AMCP) under EUROCONTROL [33]	1990s	Upgraded from ACARS. For aeronautical operational control (AOC) and air traffic services (ATS) data services. VDL Mode 4 aircraft to aircrafts communications
Universal Access Transceiver (UAT) [34]	L-band, 978 MHz	1 MHz	CPFSK (GMSK)/ TDMA	1 MHz		2002	Designed for surveillance, Automatic Dependent Surveillance — Broadcast (ADS-B)
1090ES (1090 MHz Extended Squitter) or Secondary surveillance radar (aka Mode-S) [34]	L-band, 1030, 1090 MHz	3 MHz	CPFSK (GMSK)/ TDMA	1 MHz		2002	A multi-functional surveillance and communication system designed as a surveillance improvement for Mode A/C secondary surveillance radar (SSR)
Project 34 (P34) [35]	767-773 MHz (Forward Link) 797-803 (Reverse Link)	5.4 kHz/sub-channel X 8, 16, 24 channels = 50, 100,150 kHz	OFDM	100-500 kbps	Electronic Industry Association (EIA) & Telecommunications Industry Association (TIA)	2003	Designed for public safety; candidate for future aeronautical communications (not implemented to date)
Broadband VHF (B-VHF) [32]	VHF, 118-137 MHz	2 kHz/ subcarrier	MC-CDMA+OFDM/ FDD, TDD		European 6th Framework (FP6) program	2006	For providing ATS, ATC, ATM and AOC voice and data link services simultaneously. (not implemented to date)
Broadband Aeronautical Multi-Carrier System (B-AMC) [37]	L-band, 980-1140 MHz	10.416 kHz/ kHz/sub-carrier × 48 sub- carriers = 500 kHz	OFDM/ FDD	270 kbps-1.4 Mbps	FAA & EUROCONTROL	2007	Upgraded from B-VHF (not implemented to date)
L-band Digital Aeronautical Communication System of Type 1 (L-DACS1) [38],[39]	L-band, 960-1164 MHz	9.76 kHz/sub-carrier × 51 sub-carrier = 498 kHz each	OFDM/ FDD	~ 0.2-1.37 Mbps	EUROCONTROL	2009	One of the FCI candidates for AG systems. Based on B-AMC & P34, similar to WiMAX (not

							implemented to date)
L-band Digital Aeronautical Communication System of Type 2 (L-DACS2) [40]	L-band, 960-975 MHz	200 kHz/ channel	GMSK/ TDD	~ 270 kbps	EUROCONTROL	2009	One of the FCI candidates for AG systems. Based on GSM, UAT and VDL Mode 2 (not implemented to date)
Microwave Landing System (MLS) [41]	C-band, 5031-5090.7 MHz	300 kHz	Differential Binary Phase Modulation		FAA, NASA & US DOD	1980s	All-weather, precision but short range landing system. Advancement of GPS forced MLS installation to be halted and finally in 1994 completely canceled by the FAA organization.
Advanced Airport Data Link (ADL) [24]	5146.5 MHz	8.192 MHz	MC-CDMA	128 kbps/ user	German aerospace center (DLR)	2002	Provide the information exchange necessary to establish advanced airport surface movement guidance and control system (A-SMGCS). (not implemented to date)
AeroMACS [42], [43]	C-band, 5095-5145 MHz	5 MHz/ channel	OFDM/ TDMA	Max 25 Mbps	Radio Technical Commission for Aeronautics (RTCA)	2010	all-IP network system designed to support mobile speeds up to 370 km/h for airport surface communication systems
C-DACS [102]	5 GHz	15 kHz subcarriers, 960 MHz total Channel	OFDM, SC-FDMA		EuroControl, DLR	2017	Not implemented to date.
Control and Non-Payload Communications (CNPC)	L-band, 960-977 MHz & C-band, 5030-5091 MHz	Being designed			Radio Technical Commission for Aeronautics (RTCA) under US DOT		Designed for UAS integration into NAS

For increasing the capacity and improving the performance of AG communication systems, the VHF digital link or VHF data link (VDL) standards were defined by the aeronautical mobile communications panel (AMCP) under EUROCONTROL in the 1990s [31]. The 19 MHz bandwidth allocated to aeronautical communications in the VHF band (118-137 MHz) is also used for VDL applications. VDL systems use differential 8-phase shift keying (D8PSK) modulation with the time division multiple access (TDMA) technique. The VHF band for VDL is divided into 760 channels with 25 kHz for each channel [31].

Universal access transceiver (UAT) and 1090 MHz Extended Squitter (1090ES), also known as Mode S, are two link solutions in the physical layer for automatic dependent surveillance - broadcast (ADS-B) services. ADS-B is a surveillance technology in which an aircraft determines its position via satellite navigation and periodically broadcasts it, enabling it to be tracked. The information can be received by air traffic control ground stations as a replacement for secondary radar. It can also be received by other aircraft to provide situational awareness and allow self-separation [34]. ADS-B is “automatic” in that it requires no pilot or external input. It is “dependent” in that it depends on data from the aircraft’s navigation system.

Project 34 (P34) [35] was designed for public safety purposes and was another candidate for future aeronautical communications, but which has not been implemented to date. Its air interfaces use multiple sub-channels in OFDM modulation with root raised cosine (RRC) filtering.

A more sophisticated multicarrier based aeronautical system is the broadband VHF (B-VHF) aeronautical communication system, which is based on the multi-carrier code division multiple access (MC-CDMA) technique [32]. B-VHF multicarrier technique uses subcarrier spacing of 2 kHz. The B-VHF system has not been implemented.

EUROCONTROL and FAA tasked the broadband aeronautical multi-carrier communications system (B-AMC) consortium to adapt the B-VHF system to L-band use and perform investigations to determine if and how a possible B-VHF like system could be operated in L-band. The preferable B-AMC L-band deployment is between successive DME channels, i.e., with 500 kHz offset from the regular DME channel assignments [37]. DME is a transponder-based radio navigation technology that measures slant range distance by timing the propagation delay of VHF or UHF radio signals [36]. In most of our work in this dissertation we studied and simulated DME as main interference signal to investigate FCI systems in different situations and scenarios.

As an up-to-date version of L-band avionic systems, L-DACS systems have been redefined by EUROCONTROL in 2009 [38]-[40]. L-DACS1 is a promising OFDM based communication system draft based on B-AMC technology for aeronautical communication systems deployment between successive DME channels. L-DACS2 has been proposed for L-band communication systems as a single carrier communication system approach. Its modulation is Gaussian minimum shift keying (GMSK). Existing OFDM based L-DACS1 has small spectrum utilization efficiency due to use of cyclic prefix and high out-of-band power emission. Hence, an efficient alternative to L-DACS1 is needed since L-DACS1 may not be an efficient choice for multicarrier and multiuser dense FCI networks, where multiple aircraft and ground terminals share L-band spectrum simultaneously. Also, L-DACS1 link performance in existence with adjacent DME channels is not always acceptable. In this dissertation, for improving the L-band aeronautical communication systems' spectrum utilization efficiency and performance, we study an FBMC based communication link based on L-DACS1, and investigate its advantages as a promising communication system for FCI.

Here we review some of the main studies regarding L-DACS systems and FBMC. In [15], [16] specification of the L-DACS1 physical layer is presented, covering both the deployment as an inlay and as a non-inlay system. Inlay means that the L-DACS channels lie between adjacent DME channels, whereas "non-inlay" means that the L-DACS channel center frequencies are selected without regard to DME (or other) systems. In addition to the transmitter design, the design of the L-DACS1 receiver was addressed, including methods for mitigating interference from DME systems. The results in [15] show that L-DACS1, properly configured, is capable of operating even under severe interference conditions, hence confirming the feasibility of the inlay concept. Yet, improvements to L-DACS1 can be made in several areas that we address in our work. Reference [16] shows the advantages of L-DACS1 over current legacy systems used for today's voice communication in the VHF-band; the conclusion is that current legacy systems are incapable of meeting the demands of increasing air traffic and its associated communication load.

In [17], [18] the German Aerospace Center (DLR) L-DACS1 physical layer laboratory demonstrator development was described. The main goal of the lab demonstrator was to perform compatibility measurements between L-DACS1 and legacy L-band systems, where both interference from L-DACS1 to the legacy systems as well as interference from the legacy systems to the L-DACS1 receiver is considered. These legacy systems are: DME, SSR, UAT, Galileo/GPS satellite signals. In [17] the L-DACS1 laboratory demonstrator implementation was described. Functional tests showed proper working of the baseband unit, and preliminary RF tests indicated that the final demonstrator is capable of fulfilling the L-DACS1 specifications. In [18], investigations of the L-DACS1 system performed by computer simulations have shown the suitability of the L-DACS1 design even for the challenging inlay scenario, hence L-DACS1 is expected to work based on the requirements without causing harmful interference to the legacy L-band systems. Still, as noted, improvements can be made. With the developed implementation of the L-DACS1 physical layer lab demonstrator in [18], tests (at the IF level) have also shown both the functionality of the hardware implementation and the accuracy of the implementation with respect to spectral mask and signal constellation requirements.

In [19] the authors provide a comparison between L-DACS1 and L-DACS2. The authors compared the two proposals in terms of their scalability, spectral efficiency, and interference resistance. According to these analyses L-DACS1 is more scalable than L-DACS2. Although as specified, both L-DACS1 and L-DACS2 use fixed spectral width, L-DACS1 can be much more easily scaled up to fit any available bandwidth. L-DACS1 also has better spectral efficiency because it can use adaptive modulation depending upon the noise and interference conditions, whereas GMSK based L-DACS2 cannot. The multi-carrier design of L-DACS1 is also more flexible in terms of spectrum placement. The multicarrier design of L-DACS1 is also more suitable for interference avoidance and co-existence than L-DACS2. The TDD design of L-DACS2 does more easily allow for asymmetric data traffic. The FDD design of L-DACS1 is suitable for symmetric voice traffic but less suitable for data. Terrestrial GSM base stations may cause significant interference with the L-DACS systems as well. Again L-DACS2 is more susceptible to such interference because its spectrum is very close to that of GSM. The effect of multiple GSM transmitters near the L-DACS ground stations remains to be analyzed.

In [20] the authors studied the impact of L-DACS2 on the DME system. They quantified the impact of an L-DACS2 interferer on the performance of a DME victim receiver, via computer simulations and laboratory measurements. Simulation results derived the required signal-to-interference ratio (SIR) for L-DACS2 not to cause harmful interference to the DME system.

In [21], the issues with L-DACS1 and L-DACS2 for use in Unmanned Aircraft Systems (UAS) were discussed. The authors discussed several issues in UAS datalink design including availability, networking, preemption, and chaining. They also proposed ways to mitigate interference with other L-band systems. Their conclusion is that a design with multi-carrier modulation and time-division duplexing would be more suitable than either L-DACS versions. Finally they showed how multiple aeronautical applications using the same L-band can co-exist and avoid interference using collaborative and non-collaborative strategies.

The authors of [22] investigated the synchronization process in L-DACS1, when deploying it as an inlay system in the spectral gaps between two adjacent DME channels. They showed how the synchronization suffers from DME interference. They also described interference mitigation techniques and their influence on synchronization.

In [23], [45] the authors described a pulse blanking (PB) technique to mitigate DME interference to L-DACS. They also proposed compensation of the PB effect by reconstructing and subtracting inter-carrier interference (ICI), which of course increases receiver complexity. In [23], ICI induced by PB is subtracted based on a reconstruction of the subcarrier spectra after PB and an estimation of the transmitter data symbols and the channel coefficients of each subcarrier. In [45] the authors derived a model for characterizing the DME impact on L-DACS1, without carrying out extensive simulations, and their results showed good agreement with detailed realistic simulations. They noted that careful frequency planning is still needed under certain conditions.

In [46] the authors proposed a fast filter bank (FFB)-based channelizer for L-DACS1. Their work does not consider any attempt to shape the spectrum of the transmitted signal as we propose in this work, but rather they applied filtering to the received signal to lower the OOB power levels to suppress interference from neighboring L-DACS1 or DME signals. They show that use of FFB reduces complexity by 49% to 85% over conventional filtering methods, and also offers faster filtering without compromising filtering performance.

Recently most of the research related to L-DACS systems has been concentrated on DME interference effects on L-DACS systems and methods to mitigate the effect of DME interference on L-DACS systems, [47]-[50]. This highlights the importance of our FBMC based communication system that can better suppress the DME interference than L-DACS systems.

In [47], [48] a novel and practical DME pulse pairs mitigation approach for L-DACS1 is proposed based on system identification. The approach adopts only time domain methods to mitigate interference, so it will not affect the subsequent frequency domain signal processing. At the receiver, the proposed approach can precisely reconstruct the deformed pulse pairs (DPPs), which are often overlapped and have various parameters. First, a filter bank and a correlation scheme are jointly used to detect non-overlapped DPPs, and a weighted average scheme is used to automatically measure the waveform of DPP. Second, based on the measured waveform, sparse estimation is used to estimate the precise positions of DPPs. Finally, the parameters of each DPP are estimated by a non-linear estimator. Numerical simulations show that compared with existing work, the proposed approach is more robust, closer to an DME interference free environment and L-DACS1 bit error rate is reduced compared to when no DME mitigation technique were applied. But this method costs very high complexity at receiver.

To improve the performance of the L-DACS1 receiver, a time-domain Correlative Interference Mitigation (CIM) aiming at DME impulse suppression is proposed in [58]. This proposed method could be expected to detect and mitigate the DME interference by utilizing strong auto-correlation of DME signals and weak cross-correlation with L-DACS1 signals. In CIM, correlative analysis and time-domain filtering is applied to obtain the cyclostationary features and information of DME pulses, instead of defining any thresholds (such as amplitude thresholds in PB technique) to remove DME pulses. Simulation results illustrate that CIM effectively improves the bit error ratio (BER) performance and achieves lower BER compared with PB. Furthermore, CIM can maintain its stability and effectiveness in certain transmission rates and power levels of DME pulse pairs. Comparing to PB the main disadvantage of this technique is due to its more complex processing at the receiver.

In [50], taking LTE as an example of prospective technology for aeronautical radio communications, the authors establish an aeronautical LTE communication link model and study the DME impact on it through analyzing their coexistence. This article adopts the Monte-Carlo simulation method to perform the co-existence interference study, and results show how the performance of the aeronautical LTE system is affected.

We now turn to a literature review focused on FBMC. Different classes of FBMC systems have been studied in the literature. The first proposal was done by Chang in the 1960s [5], who presented the conditions required for signaling a parallel set of pulse amplitude modulated (PAM) symbols through a bank of overlapping vestigial side-band (VSB) modulated filters. A year after Chang's work, Saltzberg extended the idea and showed how Chang's method could be modified for quadrature amplitude modulated (QAM) symbols [6]. In 1980, Hirosaki proposed an efficient polyphase implementation for the Saltzberg method [51].

The method proposed by Saltzberg is referred to as OFDM based on offset QAM or OFDM/OQAM, which has been widely cited in current FBMC system literature, and which we also employ in our proposed systems. A book on filter banks and multirate systems, including the mathematical signal processing, is [52].

One of the pioneers in implementing fast FBMC systems studied a discrete-time analysis of OFDM/OQAM multicarrier modulation in [53], based on methods studied in [52]. Fast implementation schemes of the OFDM/OQAM modulator and demodulator were proposed to reduce the complexity, and a large set of design examples was presented for OFDM/OQAM systems with a large number of subcarriers.

A review comparing OFDM and FBMC systems exists in [54]. In this article, the author addressed the shortcomings of OFDM in different applications and showed that FBMC could be a more effective solution. Applications were primarily terrestrial and cognitive radio. Based on [54] FBMC systems outperform OFDM in the following areas:

- In the uplink of an OFDMA network, an almost perfect carrier synchronization of signals from different transmitting nodes is necessary. FBMC systems achieve signal separation through filtering, thus avoiding the need for (close to) perfect carrier synchronization. Separation of the different users' signals through a filtering process also avoids the need for any timing synchronization between the users.
- In cognitive radio applications, FBMC can outperform OFDM because of using well-localized subcarrier filtering to fill the spectrum holes.
- OFDM is known to be sensitive to fast variations of the communication channels. FBMC systems, on the other hand, can be designed to be equally robust to channel time and frequency spreading. Such designs are based on isotropic orthogonal transform algorithm (IOTA) prototype filters.

On the other hand, OFDM has a number of desirable features, including lower complexity of implementation. Moreover, while OFDM can be easily adopted for MIMO channels, development of MIMO-FBMC systems/networks requires more signal processing.

Studies of different aspects of FBMC systems in different scenarios have been accelerating in recent years [55]-[59]. Recently in [55] the authors studied FBMC and two existing CP based FBMC systems and proposed a new CP based system with good spectrum shape with lower out of band power. Actually the idea of using CP in FBMC was proposed to mitigate the channel delay spread in very highly frequency selective channels with long multipath delays. Based on studies in the literature, adding a CP to FBMC is not as straightforward as in OFDM. In order to add a CP to FBMC we need to change the structure of the FBMC system. It is known that after adding a CP to FBMC the "perfect" spectral shape of FBMC is significantly degraded. Authors in [55] showed that their newly proposed CP-based FBMC system has the best power spectral density (PSD) shape with lowest out of band power among the all CP based FBMC systems that they reviewed in the paper, and this is at the cost of larger data overhead.

In [59] the authors directly optimized the FBMC filter impulse-response coefficients to minimize stopband energy and constrain the inter-symbol interference (ISI) and inter-carrier interference (ICI). Their numerical results showed that the optimized filters achieve significantly lower stopband energy than those attained by other popular techniques such as frequency sampling and windowing based techniques.

In our first published papers [3], we proposed a new communication system for FCI systems, according to L-DACS requirements. This communication system is based on the FBMC technique, and to the best of our knowledge it was the first study to propose use of FBMC for AG applications. In this dissertation we investigate this system in depth and compare it with the L-DACS candidates based on our publications [3], [4], [60]-[65].

2.2 C-BAND SYSTEMS

The limited spectrum available in L-band may not satisfy the demand of services like videos and high data rate communications that may be desired for UAS. The idea dual-band links that employ both C-band and L-band are of interest. In this configuration, the L-band can transmit low rate messages and provide large coverage while the C-band is used to transmit higher data rate signals such as video at relatively short distances.

The microwave landing system (MLS) [41] may be the earliest C-band aviation application. It was designed in the 1980s and uses a signal bandwidth as large as 300 kHz. Advancements of the global positioning system (GPS) forced MLS installation to be halted and finally in 1994 completely canceled by the FAA organization, although as noted, some MLS systems are still in use.

As one of the first C-band multicarrier systems, advanced airport data link (ADL) has been proposed by the German Aerospace Center (DLR) [24]. The ADL has to provide the information exchange necessary to establish an advanced surface movement guidance and control system (A-SMGCS). For efficient operation, A-SMGCS requires a communication link between the air traffic control tower and aircraft, which can guarantee the necessary data transfer between controllers and pilots. A transmission bit rate of at least 128 kbit/s per user is required to provide the necessary transmission capability for surveillance, taxi management and additional services. At least 100 simultaneously active users (aircraft and ground vehicles) should be served by the ADL in order to fulfill future airport capacity requirements. Since such a high capacity, high rate data link requires relatively large bandwidth, it cannot be realized within the VHF band, which is already extensively used. Thus, alternative frequency bands have to be identified. Therefore the radio frequency band 5.1465 GHz has been selected for ADL. ADL proposes the MC-CDMA communication technique, which is a combination of

OFDM with the Code Division Multiple Access (CDMA) technique. This system has not been implemented.

Airport surface area networks have been deployed at large and small airports [25]. As mentioned, since 2010, RTCA has developed a version of the 802.16 standard specifically tailored for airport operation [9]. This "aviation profile" defines specifics of the 802.16e standard for airport surface use, and is denoted AeroMACS. AeroMACS, time domain symbols are modulated using the cyclic-prefix OFDM (CP-OFDM) technique.

CHAPTER 3

AIR-TO-GROUND ENVIRONMENTS, CHANNELS AND FCI COMMUNICATION SYSTEMS

3.1 ENVIRONMENTS AND CHANNEL MODELS

The AG channel models we employ in our studies and simulations are based upon measurements conducted by NASA Glenn Research Center for different environments in the USA: over-sea (Oxnard, CA), mountainous (Telluride, CO) and hilly/desert suburban terrains (Palmdale, CA, and Latrobe, PA) [66]-[70]. In this dissertation we also use the channel model of a large size airport in Ohio [86] which was modeled based on one of these NASA measurements. For AG case all measurements were made using a medium-sized aircraft, at altitudes ranging from approximately 500 m to 1.9 km, with a ground site (GS) antenna height of 20 m. Aircraft antennas were monopoles mounted on the aircraft underside. Measurements were made in both the aeronautical L- and C-bands simultaneously. Flight paths were at nearly constant altitude and velocity (which ranged from approximately 90-100 m/s). See [66]-[70] for more detail on the measurements.

Here we describe the AG channel models developed based on these measurements results. These channel models are time-varying channel impulse response (CIR) models for the different environments. In AG channels, similar to terrestrial channels, we can have some reflected and scattered signals from obstacles that exist in the environment of the transmitter and receiver. According to the measurement results, most of the time the receivers had a line of sight (*LOS*) to the GS transmitter (Tx), resulting in a strong LOS component in the received signals. The second strongest component was usually the reflected signal from the earth surface. This surface reflection is very strong in over-water channels but is significantly attenuated in rough terrain environments such as mountain and woodland environments. Other reflected signals with relatively higher delays due to intermittent multipath components (*IMPC*) from reflections were also observed; these are incorporated in the simulated channel models. These intermittent multipath components generally have a low probability of occurrence, hence for more "open" settings with a strong surface reflection (such as over-water), the CIR or power delay profile (PDP) of the channel is very similar to the two-ray channel model [66]. In Figure 3.1 we show a general view of the channel environment in AG communication systems.

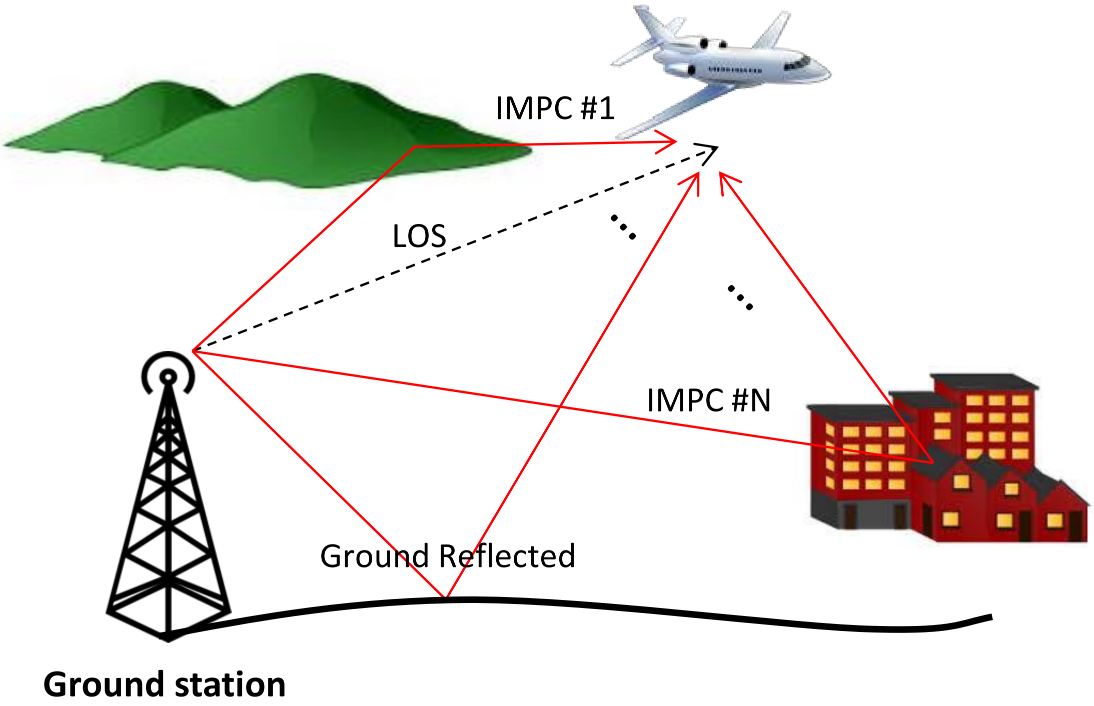

Figure 3.1. AG Communication Systems Wideband Channel Model.

In a LOS setting, we can calculate the path loss or received power (assuming known transmitter power) based on Friis transmission equation. Followed by NASA measurements, empirical path loss as a function of link range (R) is found by [67],

$$PL(R) = P_t + G_t + G_r + G_{HPA} + G_{LNA} - L_C - P_r(R) \tag{3.1}$$

where P_t denotes transmitted power in decibels above one milliwatt (dBm); G_t and G_r are the dynamic GS antenna and aircraft antenna gains as functions of azimuth and elevation angles in decibels relative to isotropic antenna gain (dBi); G_{HPA} and G_{LNA} denote the gains of the Tx high-power amplifier (HPA) and the Rx low-noise amplifier (LNA), respectively in decibels; L_C is the cable loss in decibels; and $P_r(R)$ denotes the measured received power at link range R in dBm. The classic log-distance path loss model follows [67]:

$$PL(R) = A_0 + 10nlog_{10}\left(\frac{R}{R_{min}}\right) + X \tag{3.2}$$

where A_0 in decibels denotes the path loss at the minimum link range $R_{\min}$, n is the dimensionless path loss exponent, and X denotes a zero-mean Gaussian random variable with standard deviation σ_X. These parameters and values were presented in [66]-[68] for different AG environments.

In our AG communication systems the CIR between each transmitter and receiver antenna pair is defined as function $h(\tau; t)$ which represents the response of the channel at time t to an impulse input at time $t - \tau$ [66], here in complex baseband form,

$$h(\tau; t) = \sum_{k=0}^{N-1} z_k(t)\alpha_k(t)e^{j\varphi_k(t)}\delta[\tau - \tau_k(t)] \tag{3.3}$$

where N denotes the total number of multipath components including the *LOS* and earth surface reflected signal. For the kth time varying multipath component, $\alpha_k(t)$ represents the received amplitude, $\tau_k(t)$ the time-varying delay, $\varphi_k(t)$ the phase and $z_k(t) \epsilon \{0,1\}$ denotes the presence or absence of an MPC, i.e., z describes the *on/off* (birth/death) effect of kth multipath component. The *on* probability of $z_k(t)$ generally decreases as the delay, or tap (*k*) index increases. In (3.3) the phase is given by,

$$\varphi_k(t) = \omega_{D,k}(t)[t - \tau_k(t)] - \omega_c \tau_k(t), \tag{3.4}$$

which depends on the time varying Doppler shift of the kth MPC, $\omega_{D,k}(t) = v(t) f_c \cos[\theta_k(t)]/c$, where $v(t)$ is the relative velocity of the aircraft, $\theta_k(t)$ is the aggregate phase angle of all components arriving in the *k*th delay bin (modeled as uniformly distributed over [0, 2π] for $k>2$), and *c* is the speed of light. Using CIR model (3.3), for different environment we can define a tapped delay line (TDL) model that we use in our simulations in order to estimate AG communication system performance. The TDL is a time-varying, linear, finite impulse response (FIR) filter. For the CIR in (3.3) there is another parameter reported in [66]-[68]; MPC duration (D_k). This parameter describes the "on" duration of an IMPC, and this can be expressed in either time or distance units (as they are related by flight velocity).

In (3.3), the first and second components (*k*=0, *k*=1) refer to the *LOS* and earth surface reflected (*Ref*) signals. Earth surface reflections are not only present in smooth, e.g., over-sea, environments, but were also observed for some portions of the hilly, mountainous, and suburban terrains. Since the LOS was almost always present in these AG channels, the small-scale fading is well characterized by the Ricean distribution, and this distribution is concisely described by the Ricean or K-factor. The K-factor is the ratio of power in the dominant component to that in all the other MPCs. *K*-factor values in decibels were modeled in [66]-[68] versus link range in kilometers for different environments as,

$$K(R) = K_0 + n_K(R - R_{min}) + Y, \qquad (3.5)$$

where K_0 denotes $K(R)$ at the minimum link range $R_{\min}$, n_K denotes the slope, and Y denotes a zero-mean Gaussian random variable with standard deviation σ_Y. We note that based on these measurements K-factor values are different for L-band and C-band with C-band values approximately twice those of L-band (in dB).

In (3.3), the higher-indexed (k>2) components refer to *IMPCs,* which usually have much smaller relative powers. Based on analysis and results in [66]-[70] each IMPC has different duration and probability of occurrence as a function of distance, and we can employ these features in our CIR model of each environment.

The parameters z_k, τ_k and D_k are functions of the GS local environments and were found to exponentially change over link range R. Based on aggregate results of two C-band receivers and multiple flight tracks in each environment, the values of *on* probability and statistics (maximum, median, and mean) of D_k and τ_k were collected for 1-km link range bins of each multipath component in [66]-[68]. The authors proposed a linear model to quantify the variation of these parameters, which follows:

$$log_{10}(y) = C_0 + n_y R + Z, \qquad (3.6)$$

where y denotes either the on probability of the kth tap ($\mathrm{P}(z_k) = 1$), τ_k, or D_k; C_0 denotes the value at minimum range $R_{\min}$; n_y is the slope; and Z is a zero-mean Gaussian random variable with standard deviation σ_Z. In this dissertation we used this model to simulate the IMPCs in our TDL channel models.

In multipath wireless channels, the root mean square delay spread (RMS-DS) is one important parameter that describes the delay or time spreading severity of the channel. In discrete time processing of RMS-DS first we align CIRs so that the LOS component has zero delay. With this CIR delay initialization, the RMS-DS is calculated as follows,

$$\sigma_\tau = \sqrt{\frac{\sum_{k=0}^{N-1} \alpha_k^2 \tau_k^2}{\sum_{k=0}^{N-1} \alpha_k^2} - \mu_k^2}, \tag{3.7}$$

where μ_τ is the mean excess delay and is given by,

$$\mu_\tau = \frac{\sum_{k=0}^{N-1} \alpha_k^2 \tau_k}{\sum_{k=0}^{N-1} \alpha_k^2} \tag{3.8}$$

For calculating the reflected signal over the earth surface in (3.3), we have two deterministic geometric models: the flat earth two ray (*FE2R*) and curved earth two ray (*CE2R*) models [66]. In the *FE2R* model we assume the ground is a flat surface, but the *CE2R* model is more realistic, particularly as link distance increases, since it accounts for the curvature of the earth. In all parts of our simulations the *Ref* component is calculated based on the *CE*2*R* model. Therefore the *LOS* and surface reflected components are computed via the link geometry and electrical parameters of the earth's surface; these two components are hence mostly deterministic.

The IMPC power values (α_k), over all environments, were found to have relative powers well modeled by a Gaussian distribution, with relative mean value denoted $\mu_k = 10log(\frac{\alpha_k^2}{\alpha_{LOS}^2})$ dB, and standard deviation denoted σ_k dB [66]-[68]. Table 3.1 lists the IMPC Gaussian power parameter values, maximum number of MPCs (*N*), maximum RMS-DS (σ_τ), maximum IMPC duration (D_{max}) (typically for the third component), and the maximum probability of occurrence (P_{max}) of the IMPCs for different studied environments based on measurement results. In chapter 4 we provide more details about these channels.

Table 3.1. AG channels IMPC statistical parameters values

Environments	μ	σ	N	**Max σ_τ (ns)**	D_{max} (s)	P_{max}
Over-sea, Oxnard (CA) [66]	27.4	3.0	3	364.7	0.06	0.027
Mountainous Telluride (CO) [67]	26.4	3.6	7	177.4	1.16	0.176
Suburban Hilly Latrobe (PA) [68]	30.3	4.1	9	1190.8	-	-
Suburban Desert Palmdale (CA) [68]	23.3	5.1	9	4242.9	-	-

The following 10 steps describe the algorithm of generating the TDL model MPC samples for the AG channel models, from [67] and [68]:

1. Initialize $D_k = 0$ for all values of k (3, 4, . . . , N).
2. For a given value of link range R or time t, implement the LOS and ground reflection component if present [the first and second terms in (3.3)]. Note that the ground reflection is often very weak in the hilly/mountainous terrain.
3. For $k = 3$ to N (each tap index), if k=3 go to step 4; if $k \geqslant 4$ and $z_{k-1}(R) = 0$, go to step 2 and update link range R for that tap index; if $k \geqslant 4$ and $z_{k-1}(R) = 1$, go to step 4.
4. If $D_k = 0$, go to step 5; if $D_k > 0$, go to step 7.
5. From a distribution specified by (3.2) and tables exist in [66]-[68] for different environments, generate random variable $z_k(R)$. If $z_k(R) = 0$, the kth ray is not present, so go to step 2 and update link range R for that tap index; if $z_k(R) = 1$, go to step 6.

6. From a distribution specified by (3.2) and tables exist in [66]-[68], generate the kth ray's duration D_k. (if needed, convert duration in meters to time or symbol units), set $R_k = R$.
7. Draw a Gaussian random variable with mean μ and standard deviation σ from table 3.1, to set the kth ray relative amplitude (α_k). Select the kth ray phase (θ_k) from a uniform distribution on $[0, 2\pi)$.
8. From the distribution specified by (3.2) and tables exist in [66]-[68], set the kth ray relative delay $\tau_k(R)$.
9. Check D_k with respect to R to maintain the kth ray for duration D_k, if $D_k = R - R_k$ (reached), set $D_k = 0$ and go to step 10; if $D_k < R - R_k$ (not reached), go to step 10 directly).
10. If $k < N$, go to step 3; if $k =$ N, end of the loop.

In our simulation models we assume conditions comparable to those in the flight tests. We assume the GS antenna height is 20 m above the surface level and the aircraft height is that flown in the different measurement environments. As an example in Figure 3.2 we show two snapshots of PDPs ($\alpha^2(t)$ in (3.3)), translated to distance, for two segments of short and long distance ranges in the suburban hilly Latrobe, PA environment. In this figure the yellow part represents the LoS signal which always exists with normalized amplitude $\cong 1$.

We point out that the dispersive AG channel models were developed for C-band, and hence our L-band models must be viewed as approximate. The MPC delays, durations, and probabilities of occurrence should be nearly identical for both bands, and it is primarily the MPC amplitudes that will differ between the two bands.

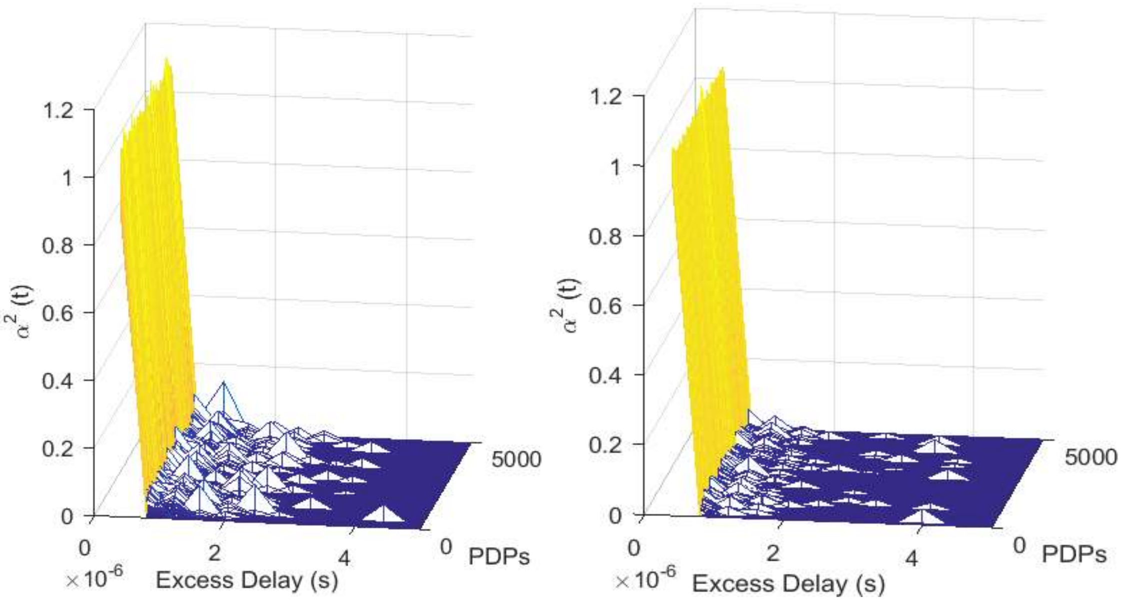

(a) (b)

Figure 3.2. Two snapshots of PDPs for different distance ranges in Latrobe: (a) distance 1.5 km; and (b) distance 20 km. (The total number of PDPs, 5000 here, is an example, and can be translated to distance via aircraft velocity and PDP sampling rate, i.e., *v*~90 m/s and PDP update rate~3 kHz yields a distance range of ~ 150 m for these PDP sequences.).

Comparing Figures 3.2 (a) and (b) we see that—consistent with measurement results—at the larger distance the IMPCs' probability of occurrence (probability of $z_k(t)$ where $k>2$), becomes smaller and that is why in Figure 3.2 (a) IMPCs are more dense and with larger amplitudes than at longer distances (Figure 3.2 (b)).

Figure 3.3 shows an example of the typical two-ray path loss vs. link distance for the over-sea channel model in Oxnard, CA. In two ray models, small-scale Ricean fading, attributable to sea surface scattering, is also present (K~12 dB) for L-band [66]. This figure shows the importance of the CE2R model with respect to the less accurate FE2R model.

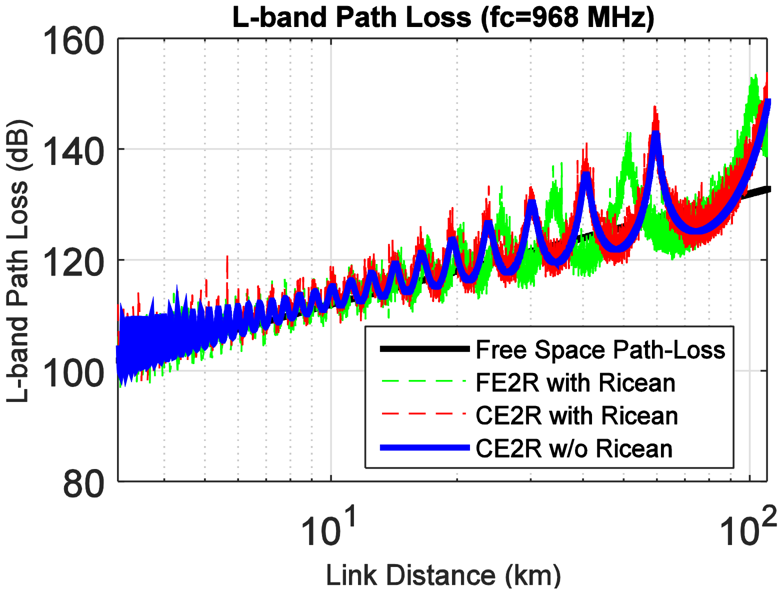

Figure 3.3. Path Loss vs. distance for the over-sea channel model in Oxnard, CA.

Another important parameter in communication system performance calculations is signal to noise ratio (SNR). Based on the described channel models we can calculate SNR values at different distances and conditions based on following procedure. First we calculate the received power at distance R, $P_r(R)$ based on (3.1). Then we calculate the total noise power (P_N) based on transmitted signal bandwidth, B Hz at the receiver assuming a noise figure of N_F dB and system double-sided additive white Gaussian noise (AWGN) power density of N_0 dBm/Hz. Therefore total noise power is calculated from,

$$P_N = N_0 + 10\log(B) + N_F \tag{3.9}$$

where N_0 is calculated based on,

$$N_0 = kT \tag{3.10}$$

where k is Boltzmann’s constant equals 1.381×10^{-23} J/K (joules per degree Kelvin), and T is the receiver system noise temperature in kelvins. Then after calculating P_N, SNR in dB at distance R is calculated based on,

$$SNR(R) = P_r(R) - P_N \tag{3.11}$$

For the over-sea channel environment the SNR versus link range is plotted in Figure 3.4 for both FE2R and CE2R models. These SNRs are plotted considering transmit power and bandwidth of 10 W and 0.5 MHz, respectively, antenna gains of 5 dB for both transmitter and receiver, total cable loss of 4 dB and receiver noise figure 3 dB at system noise temperature of 290 K. Again in these results we used small-scale Ricean fading, attributable to sea surface scattering (*K*~12 dB). These results show the importance of using more accurate CE2R model which has different SNR values versus distance. In our communication systems we can use these SNR values to estimate the bit error ratio (BER) of any (narrowband) communication system at each distance.

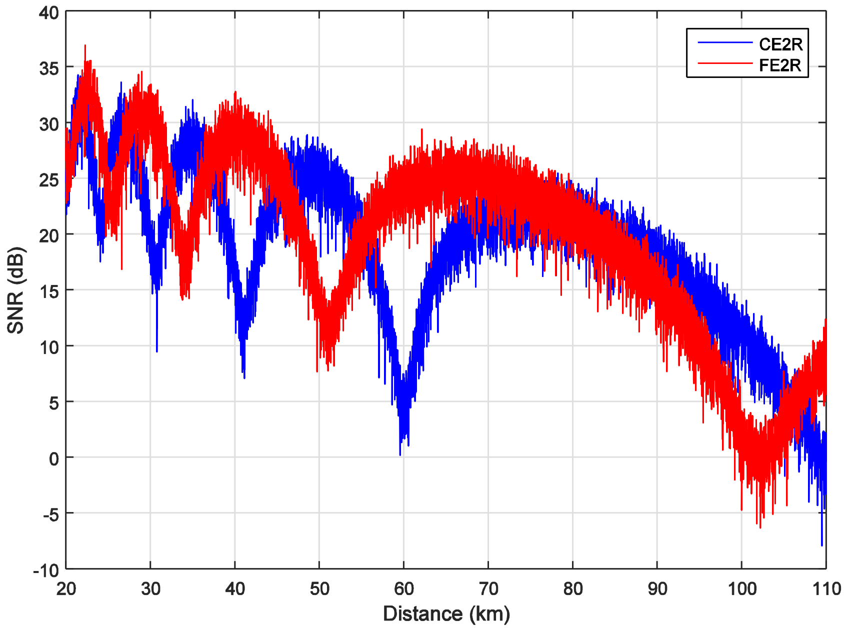

Figure 3.4. SNR vs. distance for the over-sea channel model in Oxnard CA.

3.2 COMMUNICATION SYSTEMS TECHNICAL DETAILS

In this section we describe the technical details of the L-DACS (LDCAS1, L-DACS2) and FBMC based AG communication systems. We compare L-DACS1 and FBMC physical layers as two similar multicarrier communication systems for L-band.

Due to potential lack of spectrum resources at L-band, and associated regulatory challenges, we will discuss later that these systems could also be designed for C-band operation. For L-DACS systems the desired frequency range is L-band 960-1164 MHz. Currently, L-band channels are largely occupied by high power DME signals which will be interference to these FCI systems. In the following sections first we review the DME signal characteristics since it is the main interference signal to FCI systems, then we describe L-DACS1, L-DACS2, FBMC, and SS-FBCM as FCI system candidates.

3.2.1 DME INTERFERENCE SYSTEM MODEL

DME signals operate throughout the frequency range of L-band (Figure 1.1), with different assigned frequencies for different geographic locations. This part of the spectrum is highly congested with DME signals. This led us to the idea of using communication systems such as FBMC, with better spectral shaping in the frequency domain, to decrease the interference between L-band channels. DME is a transponder-based radio navigation technology that measures slant range distance by timing the propagation delay of L-band radio signals. Similar to the concept of frequency allocation in cellular terrestrial networks, DME base stations (BS) are distributed widely geographically. Every DME channel occupies 1 MHz bandwidth, with 1 MHz separation throughout the 960 to 1150 MHz band.

There are about 152 DME channels being used on more than 1100 DME ground stations in the U.S. DME signals are high power pulsed signals with maximum 1000 W peak power for ground station transmitters and 300 W peak power for aircraft. DME transmitters send pulse pairs. The pulse pair transmission rate of DME systems varies: the maximum rate from ground station to aircraft is 2700 pulse pairs per second (ppps), and from aircraft to ground station is 150 ppps. Each DME BS transmits sequences of the signal pulse pair defined in (3.12). The signal in (3.12) pertains to baseband, and these signals are modulated to different allocated passband frequencies for different channels:

$$S_{pulse\_pair}(t) = e^{-\frac{\alpha t^2}{2}} + e^{\frac{-\alpha(t-\Delta t)^2}{2}} \tag{3.12}$$

where $\alpha = 4.5 \times 10^{11}\ s^{-2}$, $\Delta t = 12 \times 10^{-6}\ s$. Each DME signal is a sequence of pairs of Gaussian-shape pulses separated by Δt. The start time of each pulse pair is modeled statistically, based on Poisson process. The constant α determines the pulse width. After taking the Fourier transform of (3.12), the DME pulse-pair signal spectrum is obtained, and is expressed in (3.13). Figure 3.5 illustrates single DME pulse pair time and frequency domain simulation results.

$$S_{pulse\_pair}(f) = \sqrt{\frac{8\pi}{\alpha}}\, e^{(-\frac{2\pi^2 f^2}{\alpha})} e^{(j\pi f \Delta t)} \cos(\pi f \Delta t) \tag{3.13}$$

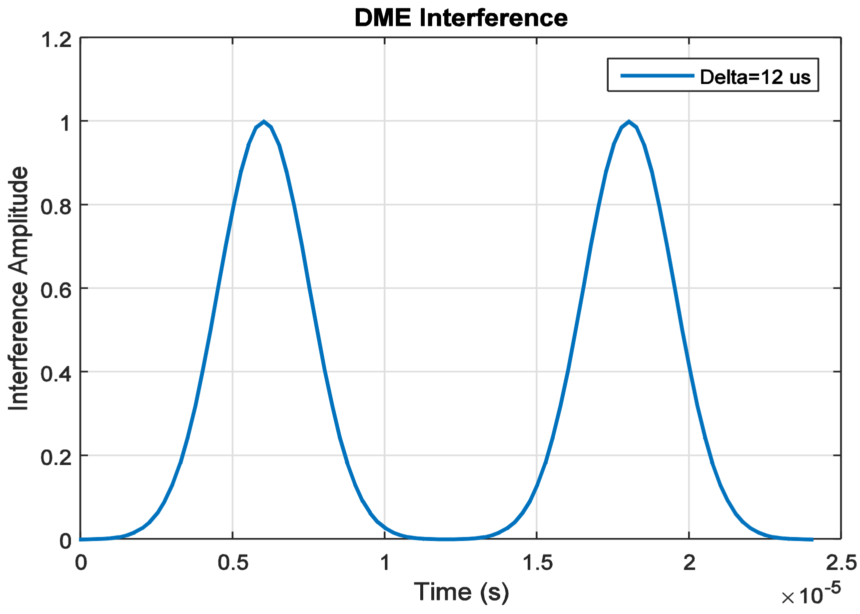

(a)

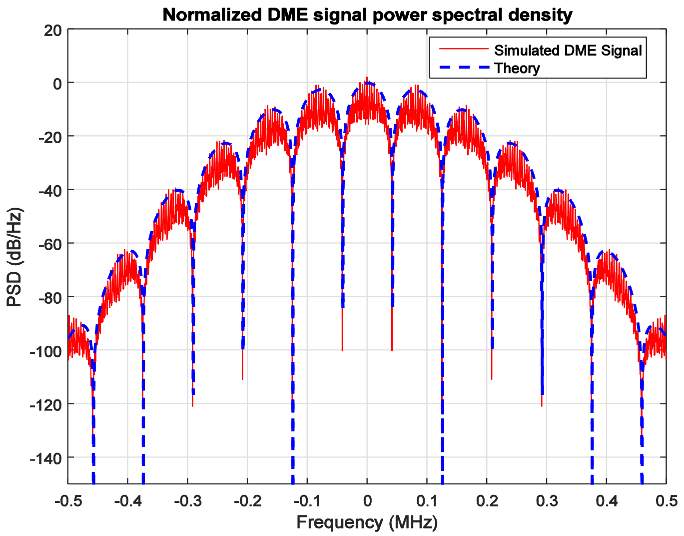

(b)

Figure 3.5. Simulated DME signal in (a) time domain, (b) frequency domain.

We assume that the signal observed at any receiver is composed of signals from N_I DME BSs operating in the same or different DME channels. The signal sequence transmitted by the i^{th} DME BS is described by $N_{i,u\;,u=0,\dots,M_i-1}$ pulse pairs in a given time interval, where M_i is the total number of pulse pairs in the signal sequence of i^{th} DME station.

As mentioned the beginning times $t_{i,u\;,u=0,\dots,M_i-1}$, of the $N_{i,u}$ pulse pairs are modelled as a Poisson process that well shows the random character of DME pulse pairs in the time domain. The resulting aggregate interfering of all DME signals from all DME stations at the L-band communications receiver is,

$$i(t) = \boldsymbol{Real}\left(\sum_{i=0}^{N_I-1}\sum_{u=0}^{M_i-1} A_i^{DME} S_{pulse\_pair}\left(t-t_{i,u}\right)e^{j2\pi f_{c,i}t+j\varphi_{i,u}}\right) \qquad (3.14)$$

where the phases $\varphi_{i,u}$ are uniformly distributed in the interval [0,2π]. The received DME signal peak amplitude for each pulse pair is $A_i^{DME} = \sqrt{\psi_i^{DME}}\;, i = 0,\dots,N_I-1$, where

ψ_i^{DME} denotes the peak power of the i^{th} DME received signal, which is calculated based on the following Friis transmission equation,

$$\psi_i^{DME} = P_I^i G_{GS}^i\left(EL^i\right) L_{free}^i G_{air}^i\left(-EL^i\right) \tag{3.15}$$

The parameter P_I^i is DME pulse transmitted peak power, which can be as large as 1 kW EIRP (transmitter power minus cable losses plus antenna gains) for DME BSs. $G_{GS}^i\left(EL^i\right)$, is GS antenna gain at elevation angle EL^i, and $G_{air}^i\left(-EL^i\right)$ is the aircraft antenna gain at elevation angle $-EL^i$, and L_{free}^i is the free space path loss. Equation 3.14 shows the aggregate passband DME signals at each L-band receiver. According to 3.14 if we assume N_I as the total number of DME stations at each L-band receiver, then by adding all DME pulse pairs ($N_{i,u\ \ ,u=0,\dots,M_i-1}$) of each DME BS ($i$=0:$N_I$-1) we can calculate the DME received signal.

More details about DME signals basics and operations are provided in [71]. In our DME link simulations in this dissertation we consider two communication links, the forward link (FL) and reverse link (RL). In the FL, signals are transmitted from GS to the aircraft, and in the RL from aircraft to GS. In this dissertation, as we suggested in [60], for increasing communication ranges in FBMC based AG communication systems, we assume that both DME and FBMC transmitters are located at the same location on GS and aircraft.

DME transmitted signals have very high peak powers in comparison to the L-DACS1 maximum transmitting power (10 W). Therefore the L-DACS1 systems can suffer significantly from DME interference. As will be shown later via our simulation results, one way to mitigate the DME interference significantly in L-DACS1 is using a well-known simple pulse blanking (PB) technique [45]. PB is well-known as an approach to combat pulsed interference; it has already been applied to DME interference in the E5 and L5-bands used by satellite navigation systems [72], and for mitigation of impulsive noise in OFDM systems [73]. In short, PB operates by "blanking" or zeroing-out receiver signal samples that exceed a pre-set threshold. The drawback of PB is that it also zeros the desired signal, hence the threshold should be selected such that the signal impairment is tolerable. In our later results we show that one of the FBMC systems advantages is that we do not need to use PB to attain system performance better than that of L-DACS1 (even after applying PB with perfect threshold optimization for L-DACS).

3.2.2 L-DACS1

L-DACS1 operates in the AG mode as a cellular point-to-multipoint system and this AG mode assumes a star-topology as shown in Figure 3.6.

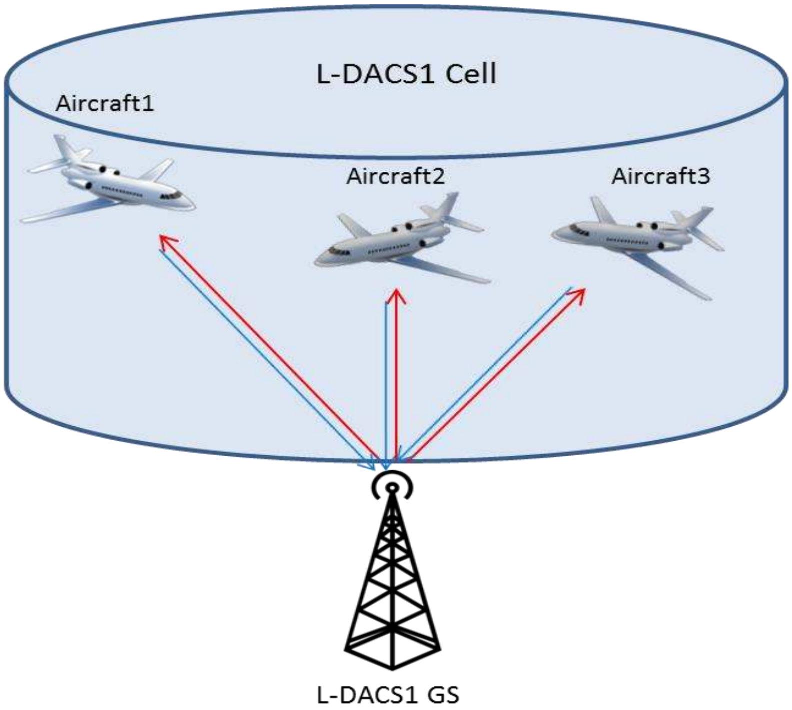

Figure 3.6. L-DACS1 point-to-multipoint communication system.

The red lines are the FLs which indicate the channels from GS to the aircraft, and blue lines indicate RL channels. The L-DACS AG communication systems must support propagation guard times sufficient for aircraft operation at a maximum link distance of 370 kilometers from the GS. But in real scenarios and as we will see in the performance results, this range may not always be achievable according to interference from adjacent DME channels. L-DACS1 channels are generated based on OFDM modulation. In OFDM a large number of closely spaced orthogonal sub-carrier signals are used to carry data on several parallel data streams or channels. Each sub-carrier is modulated with a conventional modulation scheme (such as quadrature amplitude modulation or phase-shift keying) at a low symbol rate, maintaining total data rates similar to conventional single-carrier modulation schemes in the same bandwidth. The primary advantage of OFDM over single-carrier schemes is its ability to cope with some severe channel conditions (for example, narrowband interference and frequency-selective fading due to multipath) without complex equalization filters. Channel equalization is simplified because OFDM may be viewed as using many slowly modulated narrowband signals rather than one rapidly modulated wideband signal. The low symbol rate makes the use of a guard interval between symbols affordable, making it possible to eliminate ISI and utilize multipath “echoes” and time-spreading to achieve a diversity gain, i.e., a signal-to-noise ratio improvement [74].

The structure of the typical L-DACS1 forward and return link OFDM symbols in the frequency domain is depicted in Figure 3.7-a for FL. Based on this structure seven sub-carriers on the left and six sub-carriers on the right of the signal spectrum are assigned as guard bands. There is null subcarrier at center frequency. In OFDM and

OFDMA physical layers, the DC subcarrier is the subcarrier whose frequency is equal to the RF center frequency of the transmitting station. In order to simplify the digital-to-analog (DAC) and analog-to-digital (ADC) converter operations, the DC subcarrier is nulled. In this subcarrier structure of L-DACS1 we also have pilot subcarriers for channel estimation and equalization purposes. Figure 3.7-a shows the structure in RL.

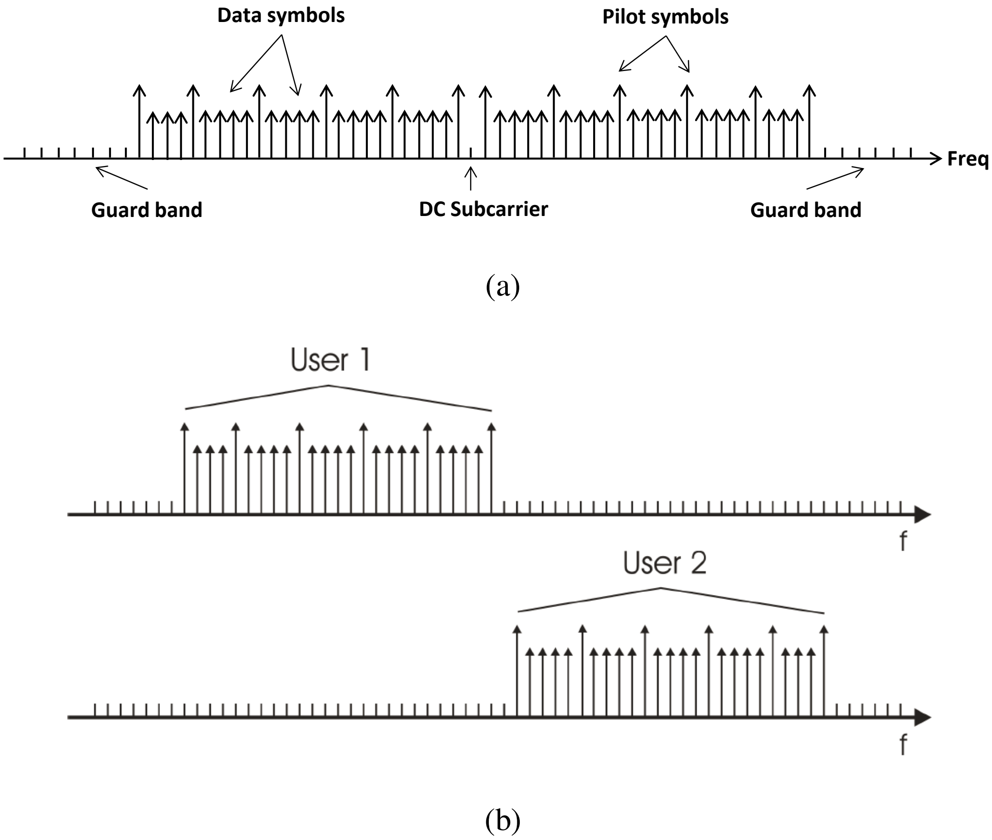

Figure 3.7. L-DACS1 subcarriers structure in frequency domain, (a) FL, (b) RL

Note that in the RL, the (joint) time-frequency domain is segmented into “tiles” assigned to different aircraft or users. Actually L-DACS1 RL transmission is based on an OFDMA-TDMA burst structure, where a time period is assigned to different users on demand. One tile spans a half of the total number of sub-carriers available in the RL (25 contiguous sub-carriers) and six contiguous OFDM symbols. One tile is assigned to only one user, but the following tile in the time direction can be used by another user. Thus, subsequent received OFDM symbols belonging to different tiles can carry data from different users.

In the time domain the duration of the inverse (fast) Fourier transform (*IFFT*) of this signal is referred to as the useful symbol time (T_u). A copy of the last T_{cp} samples of the useful symbol period, termed the cyclic prefix, is added in front of this signal. The first T_w samples of this useful period are also added to the end of signal for windowing purposes (also known as cyclic postfix). Therefore the L-DACS1 total symbol length is T_s=T_u+T_g+T_w.

This OFDM structure is known as cyclic prefix-OFDM (CP-OFDM), which by adding CP we can deal with the delay spread of the channel in the time domain and hence ISI. In CP-OFDM systems we apply windowing over each cyclic prefixed symbol. Windowing is a popular method of reducing the out of band power or spectral side-lobes of OFDM by smoothing transitions. A popular window usually used for this purpose in the raised cosine (RC) window, because of its tapered and smooth edges. In the L-DACS1 structure we also use the RC window with roll-off factor of $\alpha = 0.107$. The L-DACS1 RC window equation is,

$$w(t) = \begin{cases} \frac{1}{2} + \frac{1}{2}\cos\left(\pi + \frac{\pi t}{T_w}\right) & 0 \leq t < T_w \\ 1 & T_w \leq t < T_s \\ \frac{1}{2} + \frac{1}{2}\cos\left(\frac{\pi(t-T_s)}{T_w}\right) & T_s \leq t < T_s + T_w \\ 0 & else \end{cases} \tag{3.16}$$

where $T_w = \frac{(T_u+T_g)\alpha}{(1-\alpha)}$.

Figure 3.8 shows the process of generating these cyclic prefix-OFDM (CP-OFDM) symbols in L-DACS1. A portion T_g of this signal provides a tolerance for symbol time synchronization errors and resistance to ISI due to the delay spread incurred through actual channels. The block diagram for the main part of the L-DACS1 communication system in the physical layer is depicted in Figure 3.9. Note that details related to the frame structure such as channel coding, interleaving, and peak to average power ratio (PAPR) reduction, synchronization, and pilot subcarrier assignments at the transmitter, and synchronization and equalization process at the receiver are not shown in Figure 3.9. CP-OFDM based communication system equations and analysis for the modulated symbols and demodulations are widely available in the literature [75], [76].

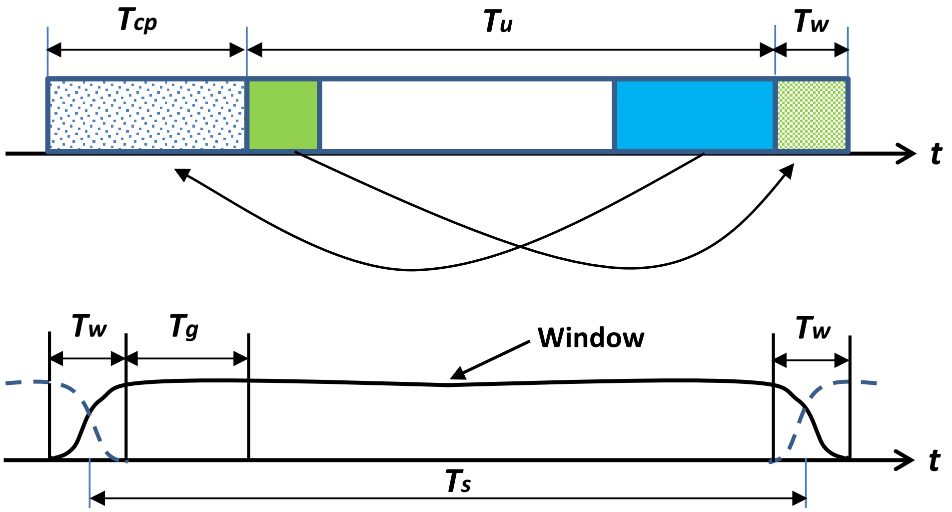

Figure 3.8. L-DACS1 CP-OFDM symbol structure in time domain with T_s=120 μs.

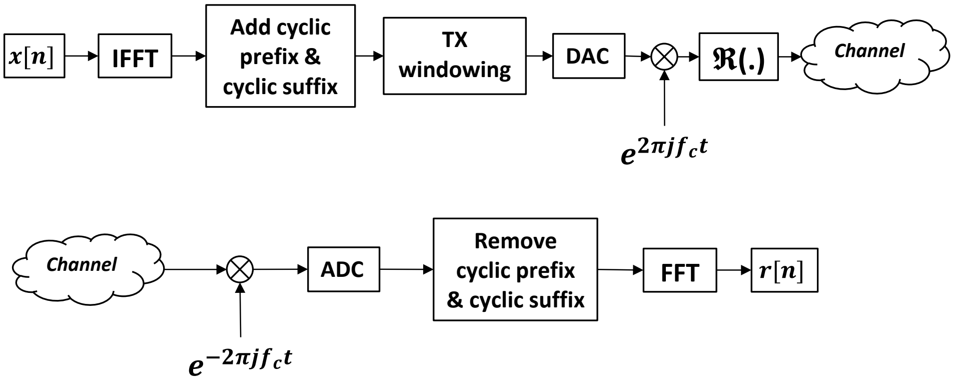

Figure 3.9. L-DACS1 communication system (physical layer).

The structure of an FL Data/Common Control (CC) frame is depicted in Figure 3.10. This frame contains 54 OFDM symbols (with lengths N=120 μs) resulting in a frame duration of 6.48 ms. The first two OFDM symbols contain synchronization sequences. The remaining 52 OFDM symbols contain data symbols and pilot symbols.

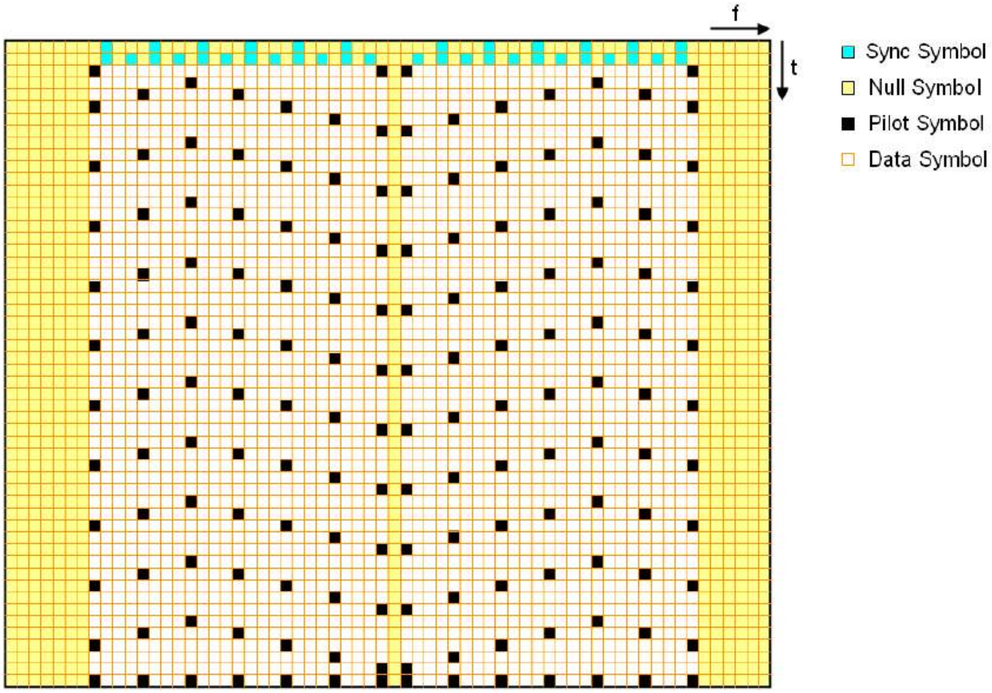

Figure 3.10. L-DACS1 FL frame structure with 6.48 ms duration (54 L-DACS1 symbols).

To realize multiple access via OFDMA-TDMA in the RL, the transmission is organized in segments and tiles rather than in OFDM frames and sub-frames as in the FL. In the RL, data segments consist of tiles. One tile spans 25 symbols in frequency and 6 symbols in the time domain and is illustrated in Figure 3.11. Each tile comprises 4 PAPR reduction symbols and 12 pilot symbols. This leads to a data capacity of 134 symbols per tile, representing the smallest allocation block in the RL. The structure of a RL Dedicated Control (DC) and RL Data segments are depicted in Figure 3.11. More details related to the framing structures for FL and RL and also coding and modulation schemes of L-DACS1 exist in [13].

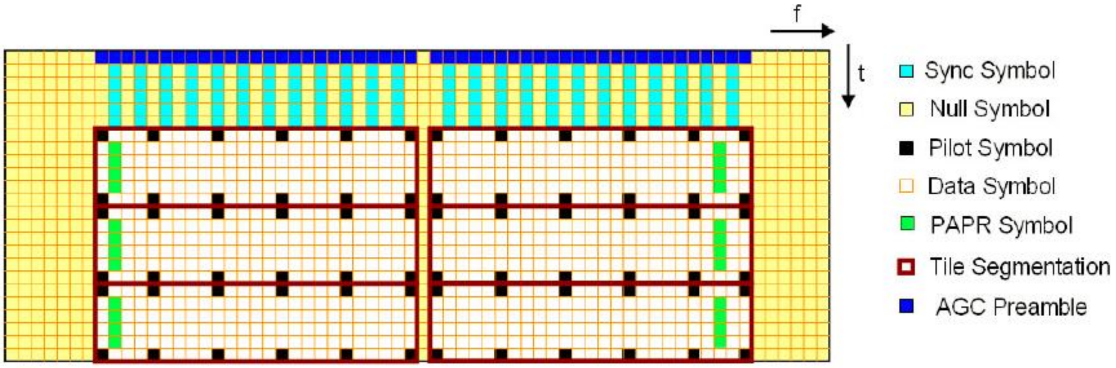

(a)

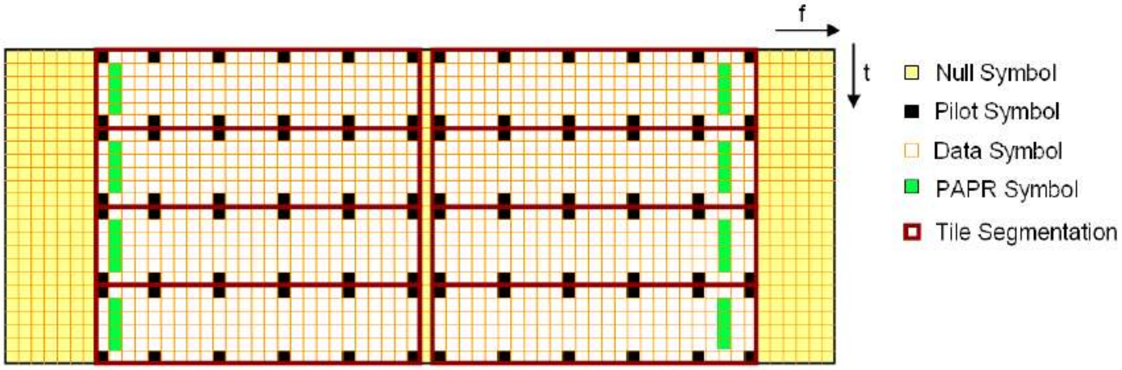

(b)

Figure 3.11. L-DACS1 RL frame segments structure, (a) DC segment, (b) Data segment.

As a summary, in Table 3.2 we list some of the main parameter values related to the L-DACS1 physical layer. Note that for L-DACS1 channels due to the inserted guard bands, an occupied RF bandwidth of $B = (N_u + 1) \times \Delta f$ is obtained, where N_u is the number of used subcarriers.

Table 3.2. L-DACS1 physical layer parameters

Total channel bandwidth (kHz)	625
Occupied Bandwidth, $\boldsymbol{B}$ (kHz)	498
Total # of subcarriers ($\boldsymbol{N_{FFT}}$)	64
Total # of used sub-carriers ($\boldsymbol{N_u}$)	50
Total # of guard band sub-carriers ($\boldsymbol{N_g}$)	13
Subcarrier spacing, $\boldsymbol{\Delta f=B/(N_u+1)}$ (kHz)	9.765
Total Symbol duration $\boldsymbol{T_s}$ (µs)	120
Symbol duration w/o CP, T_{FFT} (µs)	102.4
Total guard time $\boldsymbol{T_g}$ due to CP (µs)	4.8
Raised Cosine (RC) windowing time, T_w (µs)	12.8
Cyclic prefix time, $T_{cp}=T_g+T_w$ (µs)	17.6
RC windowing roll-off factor	0.107
FL frame length (ms)	6.48

3.2.3 L-DACS2

L-DACS2 uses techniques similar to those used in the terrestrial cellular system GSM [14]. It is a narrowband single-carrier system with 200 kHz transmission bandwidth that uses time-division duplexing (TDD). Its modulation is a special case of continuous phase modulation (CPM) that is called Gaussian minimum shift keying (GMSK). In CPM modulations the phase of the signal is constrained to be continuous across symbol boundaries, which results in interesting advantages such as constant signal power with ideal peak to average ratio (PAPR) equal to 1. In GMSK, a logical 1 bit changes the carrier phase to increase by 90° over a bit period and a logical 0 bit causes the carrier phase to decrease by 90°. This phase change is simply produced by instantaneously switching the carrier frequency between two different values, as in conventional MSK modulation. In L-DACS2 GMSK, the modulation is similar to European digital cellular communication system GSM, we have Gaussian filter with modulation index h=0.5 and

B_3T product of 0.3, where B_3 is the 3 dB bandwidth of the filter and T is the symbol duration. The symbol (and bit) rate is $1/T = 270.833$ ksymbols/s.

There is no higher order modulation available in L-DACS2 as exists in L-DACS1; higher order CPM would require high complexity at the receiver, and this is a main disadvantage of L-DACS2 in comparison with multicarrier FCI candidates. Referring to Figure 1.1, radio frequencies of L-DACS2 are restricted to the lower L-band, from 960 – 978 MHz, which is very close to the GSM900 band. In our L-DACS2 studies we used the well-known reference [77] for modeling and simulating GMSK.

Different demodulation techniques exist for GMSK signals. In this dissertation we investigate two L-DACS2 receivers, a trellis-based ("Viterbi") receiver, and a low-complexity receiver based on a differential decoder. In most of the L-DACS2 simulations we use the differential decoder because of its simplicity and good results in the AG channels. The L-DACS2 communication link block diagram appears in Figure 3.12. This is also a general view of the L-DACS2 communication system, and we did not include other features such as channel coding, equalization, etc.

In the L-DACS2 differential decoder technique, the bit decision for even and odd symbols will be made based on the sign of two multiplications: $Real\left(r\big((n-1)T\big)\right) \times Imag\big(r(nT)\big)$ and $Real\left(r\big((n+1)T\big)\right) \times Imag\big(r(nT)\big)$, where $r(t)$ is the received signal after Gaussian filtering and n and T are the discrete time sample index of the signal and symbol period, respectively.

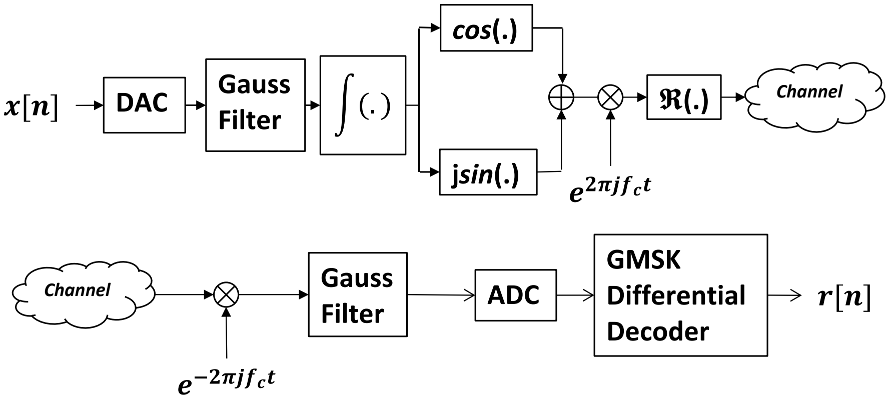

Figure 3.12. L-DACS2 communication system (physical layer).

We now briefly compare the L-DACS1 and L-DACS2 systems. L-DACS2 has almost half of the bandwidth of the L-DACS1 and it cannot support higher order modulations, therefore the spectral efficiency of L-DACS1 is higher than that of L-DACS2. As a multicarrier communication system L-DACS1 uses more advanced physical layer techniques, such as pilot scattering for channel equalization and pilot based synchronization, and these are all included in the L-DACS1 frame structure. In terms of PAPR, L-DACS2 is the best candidate because it is a single-carrier constant-envelope modulation.

3.2.4 FBMC

FBMC communication techniques were first developed in the mid-1960s before OFDM development in industry. Although FBMC methods have been studied by a number of researchers, and some even before the invention of OFDM, only recently has FBMC been seriously considered by a few standard committees. FBMC has seen renewed interest in recent years because of technological advances and faster processor platforms and for some of its favorable properties. These properties include very low out-of-band (OOB) power and consequent higher spectral efficiency when the number of guard subcarriers is reduced. According to its advantages FBMC has been also investigated as one of 5G strong waveform candidates [94], [95]. OFDM has inefficient spectral shaping on its subcarriers and this is because it uses prototype filters with rectangular impulse responses, which leads to undesirable magnitude responses with large spectral side lobes. This follows immediately from the fact that the Fourier transform of a rectangular pulse is a sinc ($sin(\pi fT)/(\pi fT)$) function, and it is well known that the side lobes of a sinc pulse are relatively large: the peak of the first side lobe is only 13 dB below the peak of its main lobe [54]. In order to unify formulation for OFDM and FBMC and to better understand the basics, the block diagrams for FBMC transmitter and receiver, which are also applicable to OFDM, is provided in Figure 3.13. We note that although the transmitter and receiver filter banks and signals are implemented in discrete time, we present them in continuous time for simplicity of illustration. The inputs in Figure 3.13 are the data signals defined as,

$$s_k(t) = \sum_n s_k[n]\delta(t - nT), \tag{3.17}$$

where $s_k[n]$ is the nth data symbol on subcarrier k, and T is the symbol time.

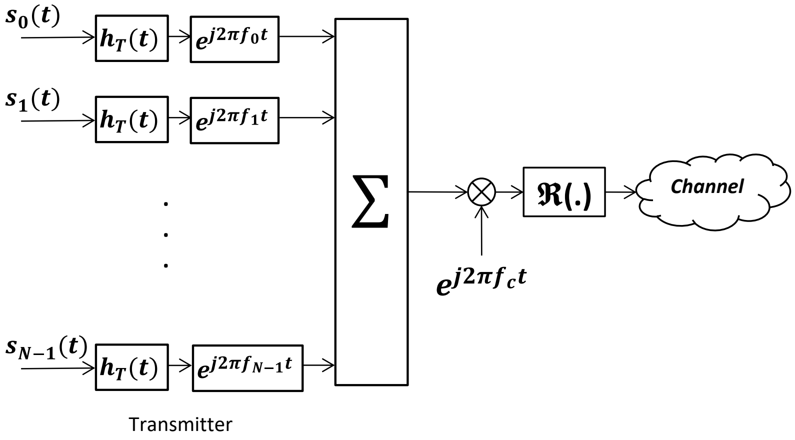

(a)

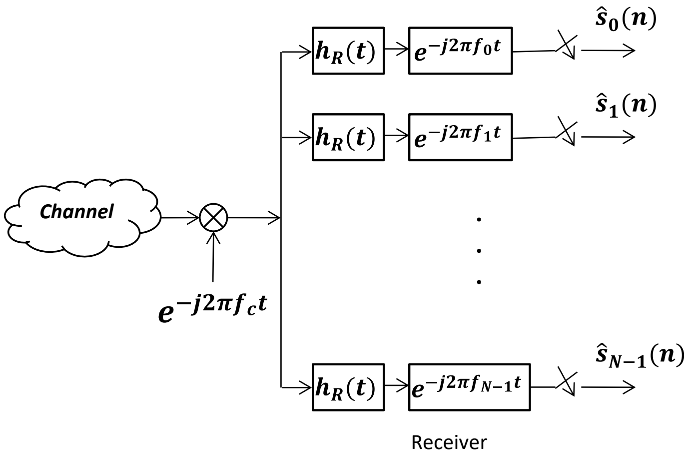

(b)

Figure 3.13. Block diagram of FBMC transceiver (applicable to OFDM), (a) Transmitter, (b) Receiver.

The exponential components at transmitter and receiver represent the frequency up and down conversions, respectively. This can be shown to be equivalent to a discrete Fourier transform. Recall that the continuous time Fourier transform of signal $g(t)$ is,

$$\mathcal{F}\{g(t)\} = G(f) = \int_{-\infty}^{\infty} g(t)e^{-j2\pi ft}\,dt \tag{3.18}$$

Therefore for efficiently implementing the transceivers in Figure 3.13—on discrete samples—we can use the fast Fourier transform (FFT) and its inverse (IFFT) as was shown in Figure 3.9 for L-DACS1.

The difference between OFDM and FBMC lies in the choice of T and the transmitter and receiver prototype filters, $h_T(t)$ and $h_R(t)$, respectively. In a conventional OFDM, both $h_T(t)$ and $h_R(t)$ are rectangular pulses $h_T(t)$ and $h_R(t)$ with length of $T_{FFT}=T$, and subcarrier spacing of $\Delta F = 1/T_{FFT}$. (We note that the notation T_{FFT} is used since in implementation this is equal to the time duration over which the received signal is sampled and passed through an FFT block). Actually in Figure 3.13 for all systems, subcarrier frequencies are $f_k=k/T_{FFT}$ for k=0 to N-1 with N the number of subcarriers. In

CP-OFDM the length of the transmitting symbol sequence is increased by the length of the CP ($T_s=T_{cp}+T_{FFT}$) to combat the channel delay spread effect at receiver. Therefore the length of $h_T(t)$, T_s is longer than $h_R(t)$, T_{FFT}. As an example of an OFDM transmitted signal Figure 3.14 shows the spectrum of the subcarriers (rectangular pulse filters on subcarriers lead to sinc spectra at different frequencies). This figure shows the orthogonality of subcarriers in the frequency domain. The orthogonality means at the center (peak) of each subcarrier there is no inter-carrier interference (ICI) from other subcarriers. In the time domain these subcarriers represent sinusoids with different frequencies. This means that when subcarriers are spaced properly in frequency, there is no inter-subcarrier interference. This comes about by having the subcarrier spacing equal to the reciprocal of the symbol time (or an integer multiple thereof, but the integer one yields the best spectral efficiency).

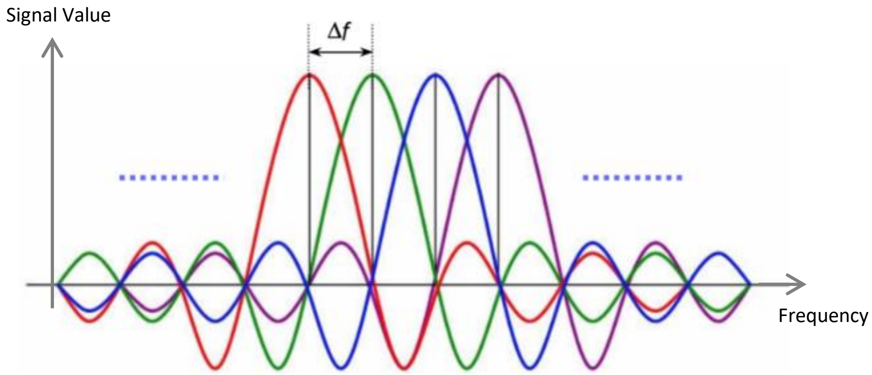

Figure 3.14. OFDM orthogonal subcarriers.

The main idea of FBMC systems is to use well shaped prototype filters to shape the spectrum of the subcarriers and therefore that of the overall transmitted signal. In order to have subcarriers with sharper frequency response—or, faster roll-off in frequency outside the main lobe—and lower subcarrier side lobes, one should use non-rectangular pulse shapes and expand the length of the prototype filters. This is of course a well-known communications engineering technique, traditionally employed in single carrier systems as well (with the root-raised cosine response being almost universally employed). By using well-shaped prototype filters FBMC systems do not need to add a CP at the transmitter for most channels and this is the reason FBMC systems have much larger bandwidth efficiency. FBMC can be used without a CP because of its well-localized filters in the time and frequency domains.

In FBMC systems $T_s = T_{FFT} = 1/\Delta F$, however the duration of $h_T(t)$ and $h_R(t)$ are greater than T_{FFT} (usually an integer multiple of T_{FFT} which is called the overlapping factor—in traditional single carrier systems this is just called the filter IR length). Hence in FBMC the successive data symbols overlap. One instructive tool, as we explore the bandwidth efficiency of FBMC systems and compare them with OFDM transmission, is the so-called time–frequency phase-space lattice representation. Figure 3.15 presents the time–frequency phase-space lattice associated with an OFDM system.

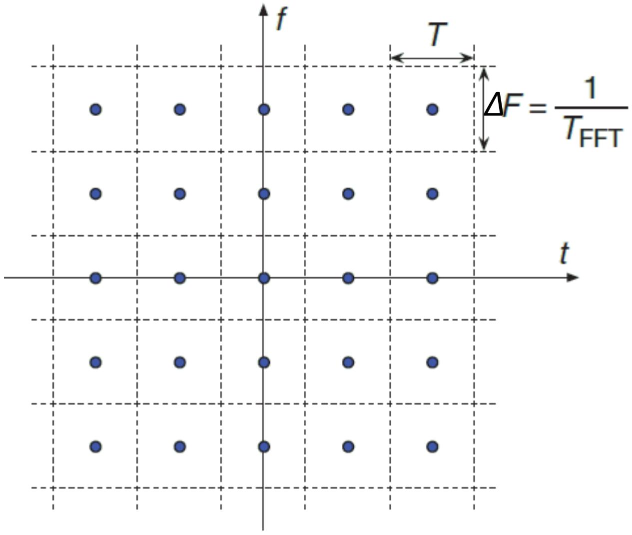

Figure 3.15. Time–frequency phase-space lattice representation of an OFDM system.

As shown in OFDM the data symbols are transmitted every T seconds (T=T_{FFT}+Tcp) and also spread along the frequency axis at the spacing ΔF=1/T_{FFT}. Therefore there is one symbol in each rectangle of area $T \times \Delta F = T/T_{FFT}$. Hence, the data symbol “density” is

$$\frac{1}{T\Delta F} = \frac{T_{FFT}}{T} \leq 1 \tag{3.19}$$

The upper limit 1 in (3.19) can only be achieved in an ideal channel, i.e., a channel with a transient period of zero, which means there is no cyclic prefix at the transmitter and T=T_{FFT}. Indeed this is unrealistic. Therefore it is fair to say that OFDM can only achieve a symbol density of less than one.

In FBMC a set of parallel data symbols $s_k[n]$ are transmitted through a bank of modulated filters as in Figure 3.14, and thus the transmit signal is generated according to following equation,

$$x(t) = \sum_n \sum_{k\epsilon K} s_k[n] h_T(t - nT) e^{j2\pi(t-nT)f_k} \tag{3.20}$$

where K denotes a set of active subcarrier indices. There are different FBMC classes depending on selection of the type of data symbols and $h_T(t)$ and $h_R(t)$ filters. In order to show the requirements of having received signal equal the transmitted signal in an ideal channel we can reorder (3.20) as in the following equations,

$$x(t) = \sum_{k\epsilon K} x_k(t) \tag{3.21}$$

where

$$x_k(t) = \sum_n s_k[n] h_{T,k}(t - nT) \tag{3.22}$$

and

$$h_{T,k}(t) = h_T(t) e^{j2\pi t f_k} \tag{3.23}$$

The filter $h_{T,k}(t)$ is obtained by modulating the prototype filter $h_T(t)$. Alternatively (3.20) may be written as,

$$x(t) = \sum_n \sum_{k \epsilon K} s_k[n] h_{T,k}(t - nT) \tag{3.24}$$

Assuming an ideal channel the data symbols $s_k[n]$ for $k \epsilon K$, and all values of n will be separable if,

$$\langle h_{T,k}(t - mT), h_{R,l}(t - nT) \rangle = \delta_{kl} \delta_{mn}, \tag{3.25}$$

where

$$\langle h_{T,k}(t - mT), h_{R,l}(t - nT) \rangle = \int_{-\infty}^{\infty} h_{T,k}(t - mT) h_{R,l}^{*}(t - nT)\, dt, \tag{3.26}$$

Sign * denotes a complex conjugate, and δ_{kl} is the Kronecker delta function defined as,

$$\delta_{kl} = \begin{cases} 1, & k = l, \\ 0, & k \neq l, \end{cases} \tag{3.27}$$

Actually (3.26) is the inner product of two signals or functions and for obvious reasons we refer to (3.25) as the orthogonality condition. Recall that for OFDM in the absence of a channel, a trivial choice of $h_T(t)$ and $h_R(t)$ is a pair of rectangular pulses with equal durations. But in the presence of a channel, each transmitted subcarrier tone will undergo a transient before reaching a steady state. To accommodate the transient period, the duration of $h_T(t)$ is extended by an interval greater than the duration of the channel impulse response, and at the receiver, $h_R(t)$ is time aligned with the transmitted tone after it has reached steady state. The duration of $h_T(t)$ is extended by the process of adding a CP to each OFDM symbol.

To satisfy (3.25) and ISI free transmission in FBMC as first requirement the receiver should use a prototype filter that is matched to the transmit filter, i.e., $h_R(T)=h_T(-t)$ (actually in general we have a complex conjugate also, but since these filters use real symbols we need not have that). As another requirement to satisfy the orthogonality of transmitted signal prototype filters should satisfy the square-root Nyquist criterion [79]. Digital transmission is based on the Nyquist theory which means the impulse response of the transmission filter must cross the zero axis at all the integer multiples of the symbol period [92]. Actually in FBMC symbols overlap in the time domain. This overlapping is similar to the conventional efficient single carrier transmission where interference between the symbols is avoided if the channel filter satisfies the Nyquist criterion. This fundamental principle is readily applicable to multicarrier transmission such as FBMC [79]. After choosing prototype filters with square-root Nyquist criterion, then assuming $k=l$ and $m=n$, (3.25) will be satisfied if we consider symmetric prototypes filters such that $h_T(-t)=h_T(t)$. Note that since $h_T(t)=h_T(-t)=h_R(t)$, in the rest of this article, we drop the subscripts and use $h(t)$ to denote a prototype filter. Therefore to achieve the ISI free transmission $h(t)$ must be square-root Nyquist and symmetric pulse shape.

Depending on the location of a data symbol on time–frequency phase-space lattice and the choice of $h(t)$, different classes of FBMC signals have been studied in the literature [54]. The first proposal came from Chang in the 1960s [5], who presented the conditions required to transmit a parallel set of pulse amplitude modulated (PAM) symbol sequences through a bank of overlapping vestigial side-band (VSB) modulated filters. A year later, Saltzberg extended the idea and showed how Chang's method could be modified for transmission of quadrature amplitude modulated (QAM) symbols without using VSB modulation [6]. Saltzberg showed that a perfect reconstruction FBMC system can be implemented using a half-symbol space delay between the in-phase and the quadrature components of QAM symbols and by proper transmit and receive pulse-shapes in a multichannel QAM system, and this yielded the maximum spectral efficiency. In the 1980s, Hirosaki continued the work on FBMC and proposed an efficient polyphase implementation for the Saltzberg method [51]. More details about these FBMC classes exist in the literature.

The method proposed by Saltzberg is referred to as OFDM based on offset QAM (OQAM) or OFDM-OQAM. The offset comes from the half symbol shift between the in-phase and quadrature parts of each QAM symbol with respect to each other. In the literature this method is referred to as staggered modulated multitone (SMT), where the word staggered refers to the fact that the in-phase and quadrature components in each QAM symbols are time staggered, [54] and [78]. Saltzberg showed that by choosing a root-Nyquist-filter with symmetric impulse response for pulse-shaping at the transmitter and using the same for matched filtering at the receiver in a multichannel QAM system, and by introducing a half symbol space delay between the in-phase and quadrature components of QAM symbols, it is possible to achieve symbol-rate spacing between adjacent subcarrier channels and still recover the information symbols, free of ISI and ICI. As noted, this scheme also has the maximum possible bandwidth efficiency.

Note that in the first class of FBMC systems in order to transmit PAM symbols we need VSB modulation, which increases the complexity of the system, therefore in our FBMC based AG communication system model we used the second class (SMT) technique.

In the SMT transmission system, shown in Figure 3.16, N parallel complex data streams are passed through N subcarrier filters. The outputs of the filters are then modulated by N subcarrier modulators with $1/T$ carrier frequency spacing. According to the time and frequency shifting of each symbol, known as a staggering process [54], we can build a lattice representation of real symbols in time and frequency phase-space in which adjacent real symbols have a relative phase difference of $\pi/2$. Figure 3.17 shows the time–frequency phase-space lattice representation of an SMT system. The points where even and odd factors of $\pi/2$ phase are applied to the respective symbols are indicated as ● and ○, respectively. Note that comparing to Figure 3.15 of OFDM the data symbol density for SMT system is,

$$\frac{1}{TF} = \frac{T}{\frac{T}{2}} = 2 \qquad (3.28)$$

But these symbols are real symbols extracted from complex QAM symbols. Therefore the data density for SMT system is same as OFDM without CP.

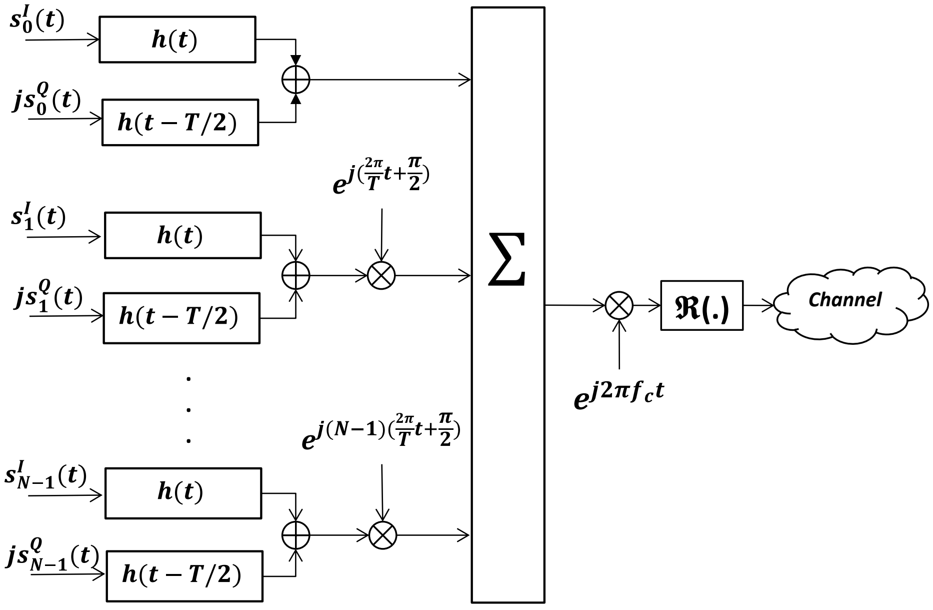

(a)

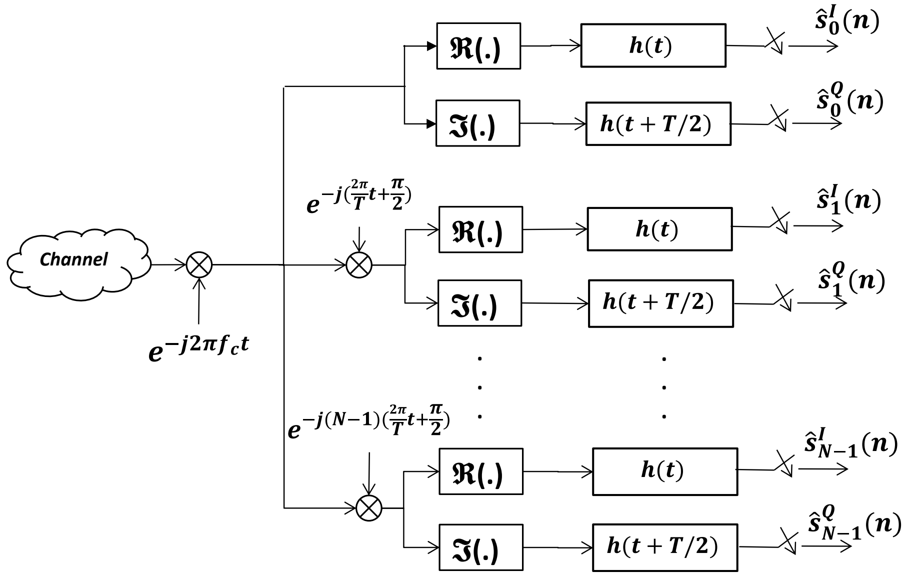

(b)

Figure 3.16. SMT based FBMC Block Diagram (physical layer), (a) Transmitter (b) Receiver.

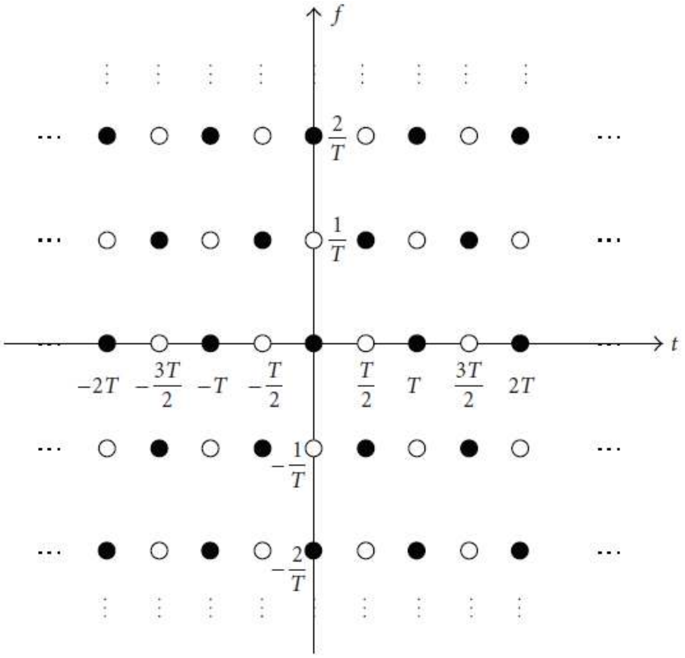

Figure 3.17. Time–frequency phase-space lattice representation of an SMT system.

To formulate the transmitted signal in SMT suppose that we have complex input symbols according to,

$$s_k[n] = s_k^I[n] + js_k^Q[n] \tag{3.29}$$

where $s_k^I[n]$ and $s_k^Q[n]$ are the real and imaginary parts of the *n*th symbol of the *k*th subcarrier, respectively. Now using Dirac delta functions we have,

$$s_k^I(t) = \sum_n s_k^I[n]\delta(t - nT) \tag{3.30}$$

$$s_k^Q(t) = \sum_n s_k^Q[n]\delta(t - nT) \tag{3.31}$$

Then the complex-valued SMT modulated signal is defined as,

$$x(t) = \sum_{k=0}^{N-1} x_k(t) \tag{3.32}$$

where

$$x_k(t) = \sum_{n=-\infty}^{\infty}(s_k^I[n]h(t - nT) + js_k^Q[n]h(t - nT - \frac{T}{2})e^{jk(\frac{2\pi t}{T}+\frac{\pi}{2})} \tag{3.33}$$

Equation 3.32 could be reformulated if we apply the staggering to real valued symbols before applying to the equation. It means we define $a_{n,k}$ as real valued symbols obtained from staggering of real and imaginary components of each complex QAM symbol $s_k[n]$ as described below,

$$\left[a_{1,k}, a_{2,k}, \dots, a_{2n,k}\right]=\left[s_k^I[1], s_k^Q[1], s_k^I[2], s_k^Q[2], \dots, s_k^I[n], s_k^Q[n]\right] \tag{3.34}$$

Then we can reformulate (3.30) as,

$$x(t) = \sum_{k=0}^{N-1}\sum_{n=-\infty}^{\infty} a_{k,n}h(t - nT)e^{\frac{j\pi kt}{T}}e^{\frac{j\pi}{2}(k+n)} \tag{3.35}$$

In this equation $e^{\frac{j\pi}{2}(k+n)}$ is the additional phase term to apply the $\frac{\pi}{2}$ phase shift between real and imaginary parts of the complex QAM symbols to satisfy the orthogonality condition. Equations (3.32) and (3.35) show that the SMT symbols are overlapped together by interval *T* with an overlapping factor. Here we explain the overlapping factor of prototype filters. For example using a prototype filter with overlapping factor 4 means the length of the filter is 4*T*. Therefore 4 FBMC symbols are overlapped together (see Figure 3.18).

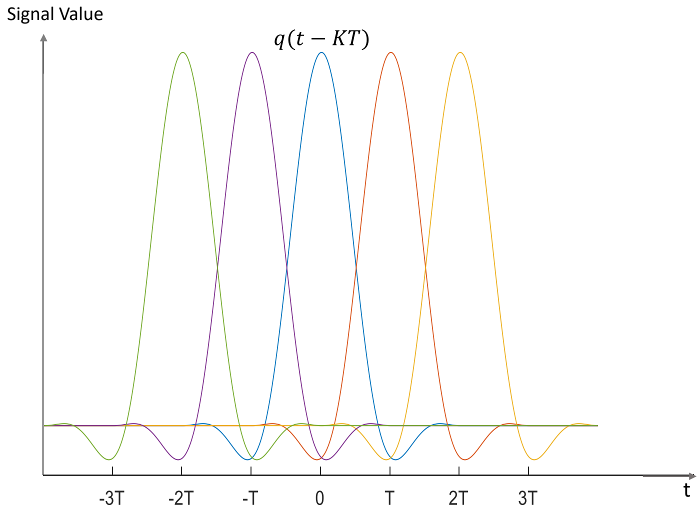

Figure 3.18. FBMC prototype filters with overlapping factor *K*=4.

In our L-band FBMC system design based on L-DACS1 requirements we chose the same number of total subcarriers 64, but due to better spectral shaping of subcarriers we reduce the number of subcarriers to 2. Note that in FBMC system the single symbol lengths are *K* time larger than L-DACS1 and after overlapping the length of FBCM frame would be comparable to L-CADS1. After choosing 54 symbols in each frame similar to L-DACS1 frame structure (Figure 3.10) the total frame length of FBMC system would be $54T+3T$ = 5.8368 ms where the second part ($3T$) is due to the two tails of the filters on both sides of the FBMC frame. Therefore as another advantage of FBMC comparing to L-DACS1 frame length (6.48 ms) FBMC frames are 683.2 μs smaller. In Table 3.3 we listed the designed FBMC based L-band physical layer parameters. Also note that comparing to L-DACS1 the number of used subcarriers are increased to from 50 to 61 which will improve the overall spectral efficiency of the L-band AG communication system as well.

Table 3.3. L-band FBMC system physical layer parameters

Total channel bandwidth (kHz)	625
Occupied Bandwidth, $\boldsymbol{B}$ (kHz)	595.6
Total # of subcarriers ($\boldsymbol{N_{FFT}}$)	64
Total # of used sub-carriers ($\boldsymbol{N_u}$)	61
Total # of guard band sub-carriers ($\boldsymbol{N_g}$)	2
Subcarrier spacing, $\boldsymbol{\Delta f=B/(N_u+1)}$ (kHz)	9.765
Total Symbol duration before overlapping $\boldsymbol{T_s}$ (μs)	409.6
Symbol duration after overlapping $\boldsymbol{T}$ (μs)	102.4
Cyclic prefix time, T_{cp} (μs)	0
FBMC FL frame length (ms)	5.8368

For implementation of SMT the main disadvantage of the block diagram depicted in Figure 3.16 is its high complexity due to the large number of multiplications, especially for a large number of subcarriers. In order to reduce the complexity we can use the polyphase network structure of filters and IFFT and FFT blocks (assuming the number of subcarriers equals a power of 2). For details about this method we refer to [78], [79], and [53]. Note that for implementing SMT based system similar to L-DACS1 we need 64 subcarriers, therefore this method is useful but does not decrease the complexity very much. For SMT based AG communication systems with a larger number of subcarriers (such as our C-band systems defined later), using this method reduces the complexity significantly.

3.2.4 SS-FBMC

This section continues our investigations on FBMC systems by applying a new idea to FBMC: spectrally shaped FBMC (SS-FBMC). Our FBMC based AG communication systems are based on the L-DACS1 system, and have physical layer parameters similar to those of L-DACS1 (e.g., equal bandwidth, power, etc.). The idea of spectral shaping is to tailor the PSD to meet some criteria [80]; here our main criterion is to maximize the robustness to adjacent channel DME interferers for L-band channels, but in principle other criteria can be applied, e.g., tailoring the spectrum to a specific channel transfer function or non-white noise across the spectrum. We conduct our spectral shaping designs by an analytical approach to find an optimum solution to the power distribution across subcarriers in terms of BER. This also will be shown to remove any error floors for different QAM modulation orders and different DME transmitting powers for our cases of interest.

Our goal here is as follows: the SS-FBMC system should provide additional gains in achievable throughput, while providing the same reliability (error probability performance) as our conventional FBMC designs [4]. In our conventional FBMC system, the transmitting power is equally distributed among all subcarriers (as in L-DACS1 and essentially all common OFDM systems). In SS-FBMC we deviate from this convention by assigning different power levels to the subcarriers to increase the subcarrier power where DME interference is highest, to improve the BER performance. We propose a method to find the required number and location of guard subcarriers, and optimize the amount of allocated power for each remaining subcarrier in order to obtain the best BER performance, without any error floor, for different QAM modulation orders and communication channels. In so doing we increase the communication system's efficiency and performance. Later we show that our conventional FBMC system and this new SS-FBMC system both have higher spectral efficiency and better resilience to DME interference than L-DACS1, but the conventional FBCM system in some cases still incurs a BER floor (as does L-DACS1). Via our spectral shaping approach in SS-FBMC we can remove these BER floors. Here we briefly describe the SS-FBMC system model, which is a small modification of the original FBMC model in [4]; see Figure 3.19.

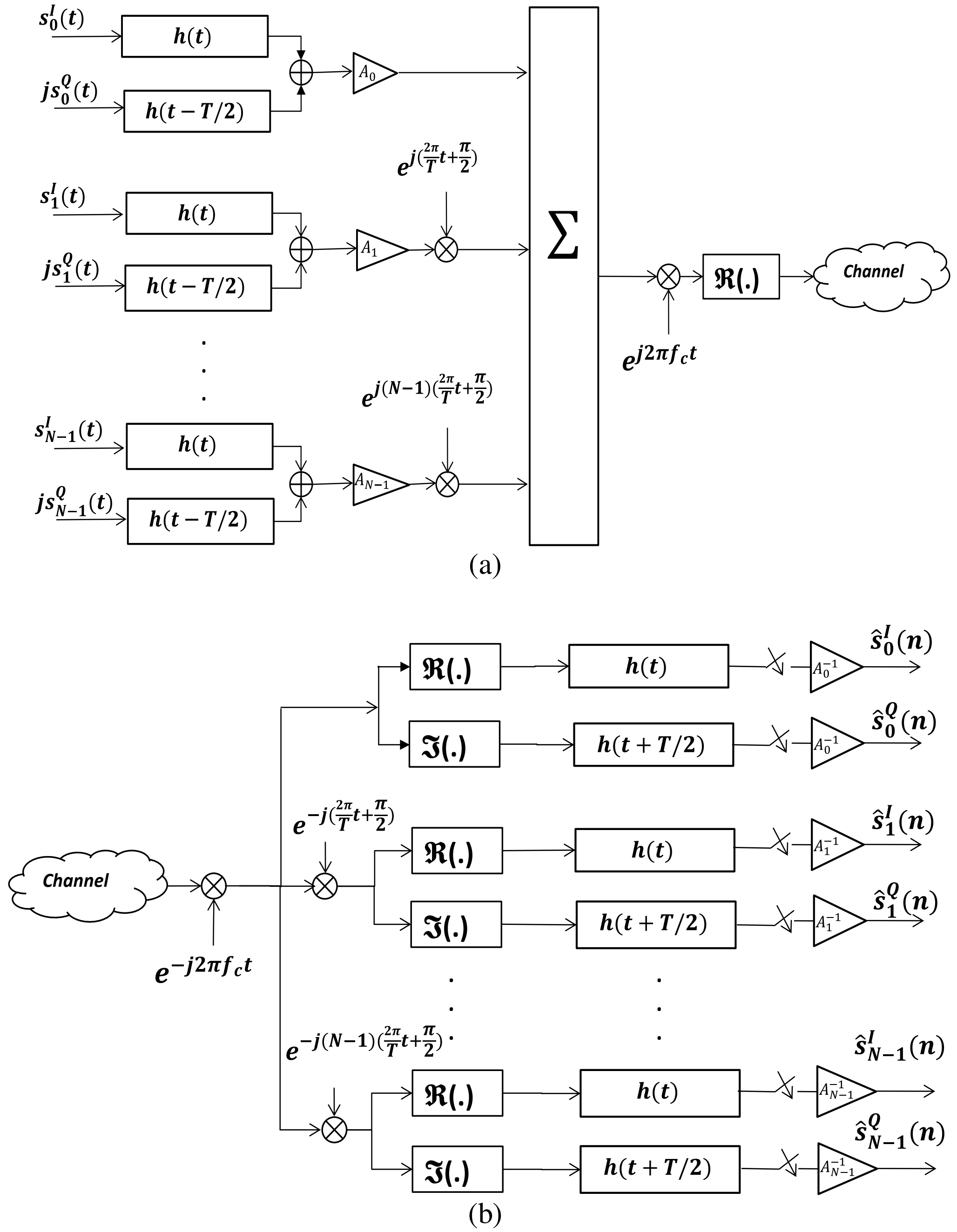

Figure 3.19. SS-FBMC Block Diagram (physical layer), (a) Transmitter (b) Receiver.

In this new design we apply an amplitude vector $[A_0, A_1, \ldots, A_{N-1}]$ to conventional FBMC subcarriers, which determines the allocated power on each of the N subcarriers (compare Figure 3.19 with Figure 3.16). In the final chapter we also show that by using this spectrum shaping method in a cognitive approach, our algorithm can automatically determine the guard band subcarriers for different modulation orders and channel link conditions, and hence adaptively improve the performance of the conventional FBMC system. This method is useful for non-white interference channel scenarios (such as DME) when the power of the channel noise or interference is non-white (not constant over the channel bandwidth). In an adaptive application, we can of course switch back to the conventional method when the channel noise/interference is white.

CHAPTER 4

COMPARISON OF L-DACS AND FBMC PERFORMANCE IN DIFFERENT ENVIRONMENTS

In this chapter we use the channel models described in chapter three to compare different FCI communication systems. We will compare the BER, PSD and DME interference impact on several communication systems. Our main focus will be on L-DACS1 and FBMC communication systems.

4.1 COMPARISON OF FCI SYSTEM; OVER-WATER AG CHANNEL AND DME INTEREFERNCE

In [4], we reviewed the physical layer characteristics of L-DACS1, L-DACS2, and FBMC, then via simulations we illustrated the performance of these communication systems in an over-water AG channel in the presence of DME interference signals. The AG channel we employed is that based upon the recent NASA measurement results [66-68]. Our main focus is on L-DACS1 and FBMC, with some L-DACS2 results included for comparison. In order to have a clear and fair comparison for all systems, we assumed perfect channel information available at receivers, and for L-DACS1 and FBMC we employed one-tap zero-forcing channel equalization, and for L-DACS2 we used a zero-forcing equalizer as well. Zero forcing equalizer refers to a form of linear equalization algorithm used in communication systems which applies the inverse of the frequency response of the channel. We compared the FBMC performance with that of the L-DACS schemes and showed that FBMC has higher spectral efficiency via its better time-frequency localized prototype subcarrier filters. This enabled use of some guard subcarriers as data carrying subcarriers, increasing throughput.

First in Figure 4.1 we show the BER versus SNR for L-DACS1, L-DACS2 and FBMC when these signals are transmitted in the reverse link (RL) *without* DME interference and encounter the same AG channel. For our simulations we used MATLAB software with Monte Carlo method [81]. In these simulations we used quadrature phase shift keying (QPSK) symbol mapping for L-DACS1 and FBMC; L-DACS2 has only binary (MSK) modulation. For other physical layer parameters we followed the system models described in chapter three.

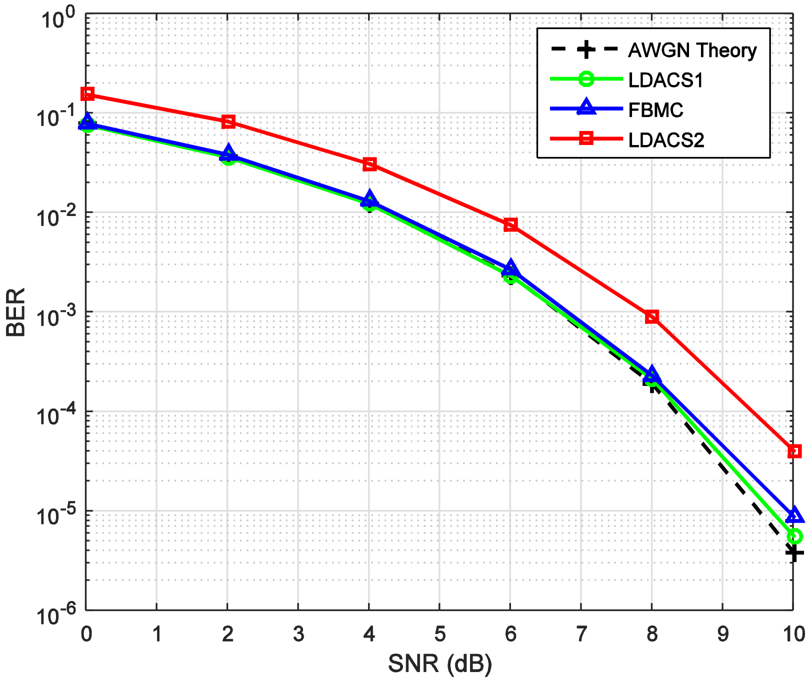

Figure 4.1. BER results without DME interference with channel equalization based on perfect CIR knowledge for over-sea channel.

As these results show the performance of FBMC is close to that of L-DACS1, and they both have performance close to that of the uncoded theoretical AWGN channel. For

L-DACS2, according to [77], we see that similar to GMSK performance, L-DACS2 has an approximate 1 dB degradation in comparison with the theoretical result.

We next added DME interference to the simulations accordingly for both the FL and RL. Before showing the BER results of DME interference case, first we show in Figure 4.2 an example of one single received frame of the FL FBMC signal after traversing the AG channel and incurring AWGN with signal to noise ratio (SNR) equals 10 dB.

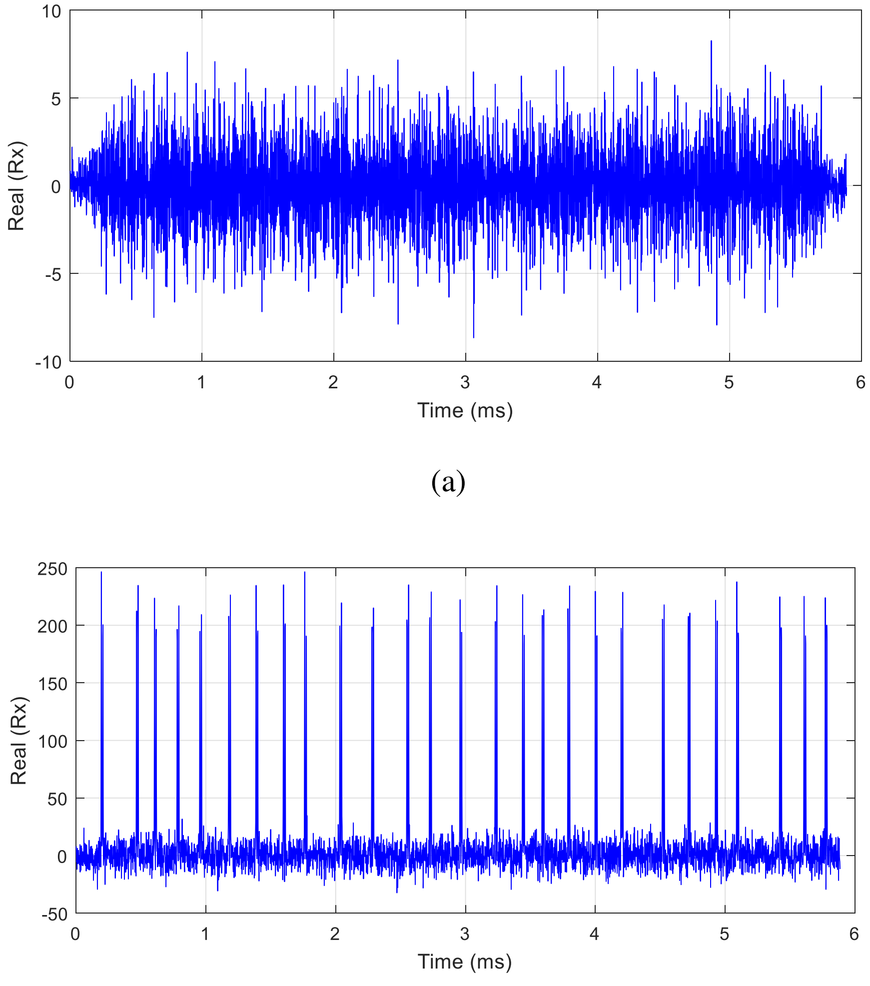

(a)

(b)

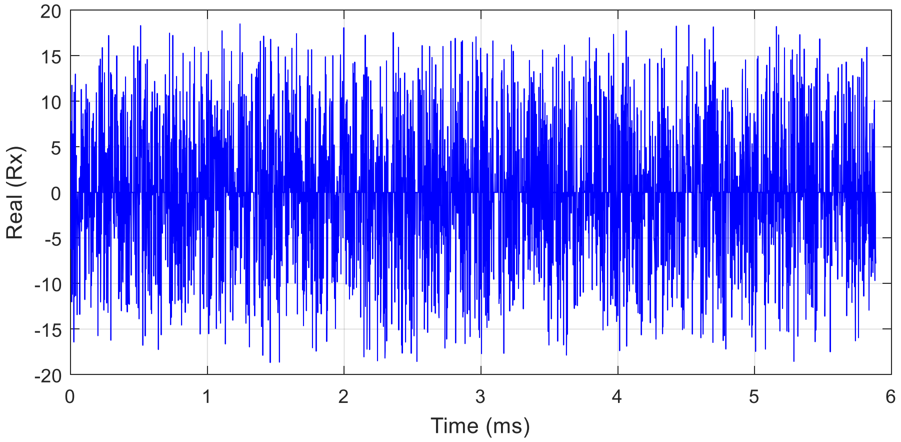

(c)

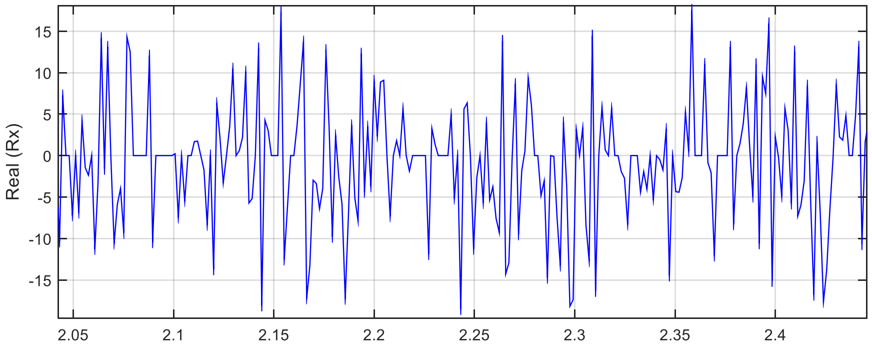

(d)

Figure 4.2. One single frame FBMC signal in the time domain, (a) without DME interference, (b) with DME interference, (c) After applying the PB technique to remove DME pulses, (d) Zoomed in portion of a short section of signal in (c) to see the zeroed samples.

In Figure 4.2 (a) we see the FBMC frame signal before adding any DME pulses. Figure 4.2 (b) shows the signal after adding the DME signal to the FBMC signal, and in Figure 4.2 (c) we see the received signal after applying the PB technique for zeroing-out the DME pulses. In Figure 4.2 (d) we zoomed in a portion of Figure 4.2 (c) to show the zeroed samples of signal after PB. As mentioned, PB operates by “blanking” or zeroing-out receiver signal samples that exceed a pre-set threshold. The drawback of PB is that it also zeros the desired signal, hence the threshold should be selected such that the signal impairment is tolerable.

Note that the process of adding and removing DME samples in Figure 4.2 is the same for L-DACS systems as well. For all systems, based on [23], we chose the PB threshold in our simulations as the maximum amplitude value of the desired transmitted signals (although this threshold is not practical but in our simulations we chose this threshold as the best case).

Figure 4.3 shows the simulated BER versus SNR for the RL and FL when DME interference is included. For these cases, the L-DACS and FBMC transmit powers are fixed at 10 W, and the DME interference peak pulse power 300 W and pulse rate 150 ppps for RL scenario and 1000 W with pulse rate 2700 ppps FL scenario.

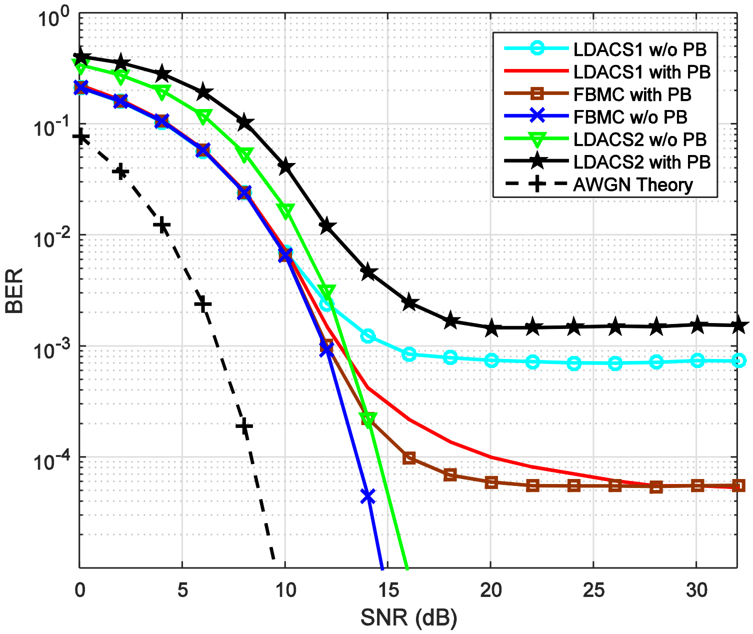

(a)

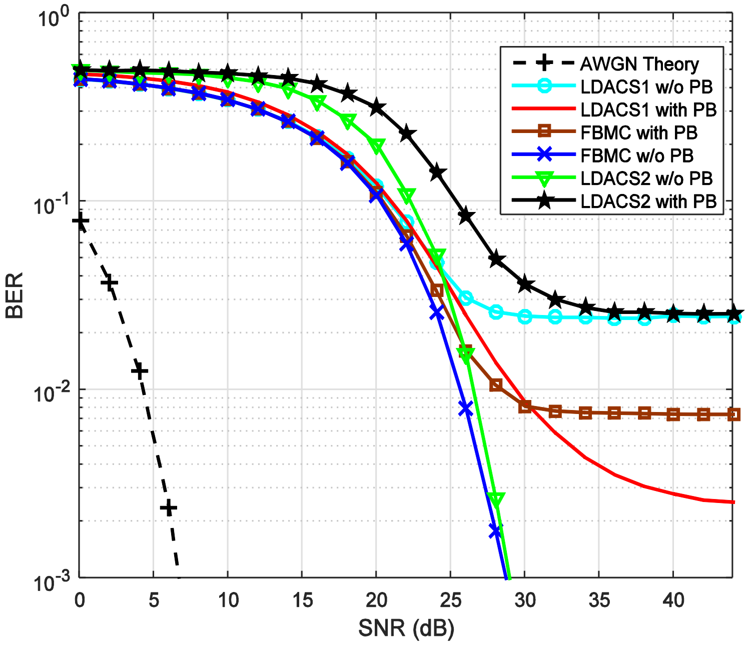

(b)

Figure 4.3. BER results in the presence of DME interference, (a) Air-to-ground (RL), (b) Ground-to-air (FL) in over-sea channel.

Note that in these simulations, all communication systems and DME base stations are assumed at the same location. In these figures we also provide results after PB. As expected for the FL due to the stronger DME transmitted signal, the BER performance is worse than for the RL. Here we note that PB improves performance only for L-DACS1, whereas for FBMC and L-DACS2, PB worsens performance. L-DACS2 and FBMC robustness against DME is due to the effects of the filters used in their receivers. Here based on the FBMC block diagram shown in Figure 3.17 we can compare FBMC with L-DACS1 and provide a short explanation of FBMC's robustness against DME pulses. According to Figure 3.17, the FBMC received signal including the DME signal interference is,

$$r(t) = \sum_{m=0}^{N-1} x_m(t) + i(t) + n(t) \tag{4.1}$$

where $i(t)$ represents the DME signal based on (3.12) and (3.14), and $n(t)$ is the AWGN with power calculated based on practical SNRs. Then for subcarrier m after down-conversion we have,

$$r_m(t) = (x_m(t) + i(t) + n(t))e^{-jm(\frac{2\pi}{T}t+\frac{\pi}{2})} \tag{4.2}$$

Then referring to (3.33) we have,

$$r_m(t) = \sum_{l=-\infty}^{\infty} \left(s_m^I[l]h(t - lT) + js_m^Q[l]h(t - lT - T/2)\right) + i(t)e^{-jm(\frac{2\pi}{T}t+\frac{\pi}{2})} + n(t)e^{-jm(\frac{2\pi}{T}t+\frac{\pi}{2})} \tag{4.3}$$

Then for real and imaginary parts of each subcarrier we have,

$$\boldsymbol{Real}(r_m(t)) = \sum_{l=-\infty}^{\infty}\left(s_m^I[l]h(t - lT)\right) + i(t)cos(m(\frac{2\pi}{T}t + \frac{\pi}{2})) + \boldsymbol{Real}(n(t)e^{-jm\left(\frac{2\pi}{T}t+\frac{\pi}{2}\right)}) \tag{4.4}$$

$$\boldsymbol{Imag}(r_m(t)) = \sum_{l=-\infty}^{\infty} \left(s_m^Q[l]h(t - lT - T/2)\right) + i(t)sin(m(\frac{2\pi}{T}t + \frac{\pi}{2})) + \boldsymbol{Imag}(n(t)e^{-jm\left(\frac{2\pi}{T}t+\frac{\pi}{2}\right)}) \tag{4.5}$$

After prototype filtering we have the following convolutions, $\boldsymbol{Real}(r_m(t)) * h(t)$ and $\boldsymbol{Imag}(r_m(t)) * h(t + \frac{T}{2})$. Assuming perfect channel estimation and perfect synchronization and using the prototype filter $h(t)$ at each symbol, and sampled at time $t=nT$ (decision points) we have the following values for subcarrier m,

$$\hat{s}_m^I[n] = s_m^I[n] + I_{Real} + n_{Real} \tag{4.6}$$

$$\hat{s}_m^Q[n] = s_m^Q[n] + I_{Imag} + n_{Imag} \tag{4.7}$$

where the second terms in these equations represent the real and imaginary parts of DME interference and the third terms represent the noise. For the interference terms we obtain,

$$I_{Real} = i(t)cos\left(m\left(\frac{2\pi}{T}t + \frac{\pi}{2}\right)\right) * h(t) \tag{4.8}$$

$$I_{Imag} = i(t) sin\left(m\left(\frac{2\pi}{T}t + \frac{\pi}{2}\right)\right) * h(t + T/2) \tag{4.9}$$

Thus for different subcarriers (values of *m*) and assuming *i*(*t*) as symmetric DME pulse pairs around *t*=*T*/2, we get different relative values for the real and imaginary parts at *t*=*T*/2. For *m*=0, I_{Imag} is zero, and for higher values of *m*, $I_{Real} >> I_{Imag}$, since *h*(*t*) is an even function around *t*=*T*/2 (with peaks at *t*=*T*/2), thus *T*/2 shifted versions of *h*(*t*) in (4.9) would still be even. Since the *sine* is an odd function the convolution in (4.9) is odd (with zero value at *t*=*T*/2). On the other hand in (4.8), with *h*(*t*) even around *t*=*T*/2, the convolution with *cosine* is also even.

In Figure 4.4 for one symbol duration we show the simulated received *DME* interference signal after receiver filtering from (4.8), (4.9) for both L-DACS1 and FBMC systems, for the first three subcarriers (*m*=0, 1, 2).

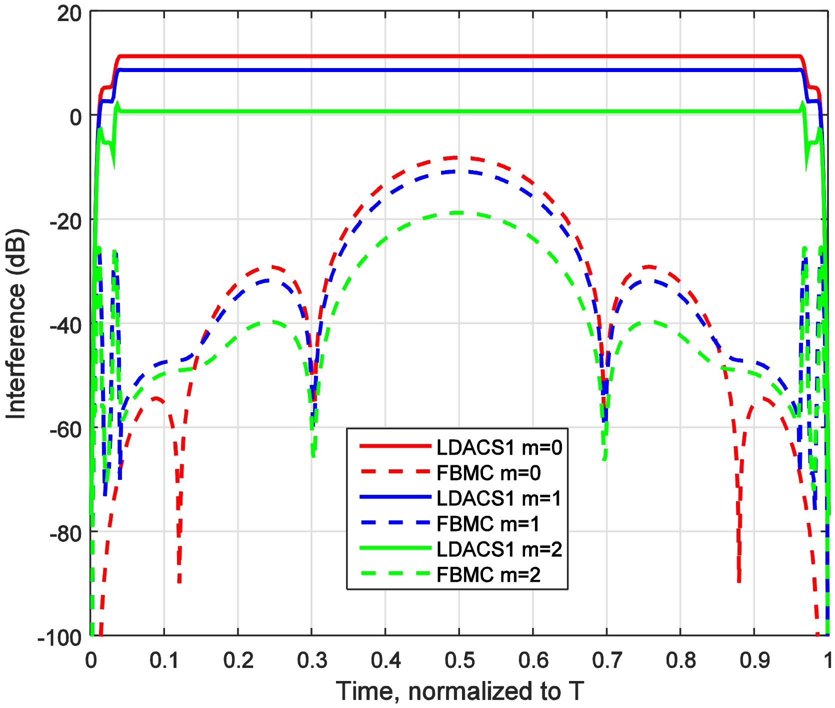

Figure 4.4. DME interference after FBMC and L-DACS1 prototype filters convolution.

Note that in our subcarrier indexing the first three subcarriers start from the left side of the L-DACS1 or FBMC spectrum, and the middle or DC subcarrier falls at $m=N/2$. After sampling these signals at the peak ($t=T/2$), we see that the FBMC filter reduces the DME interference by at least 19.5 dB in comparison to that experienced by the L-DACS1 signal, and this is similar for other subcarriers. As expected from Figure 4.4, the DME interference level decreases as we move toward the L-DACS1 or FBMC DC component. Worth noting is that although the shapes of the FBMC waveforms in Figure 4.4 will change (shift) for arbitrary values of delay, i.e., for $i(t-t_d)$ in (4.8) and (4.9), with t_d an arbitrary delay, the final result at the sampling time may be even less than 19.5 dB at $t=T/2$. Thus, in agreement with expectations, FBMC is better than OFDM for removing DME interference. The same explanation essentially applies for L-DACS2 via the sharp GMSK filtering (see Figure 3.13). FBMC and L-DACS2 have filters that largely reject the DME interference, and hence at these realistic power levels, have no error-floor[2]. Applying PB to FBMC and L-DACS2 though does create an error floor because of data deletion. In FBMC, PB deletes some signal information but very little DME interference because the FBMC filters already remove most of the DME interference. In contrast, L-DACS1 improves because the interference that is removed by PB is much more significant.

Figure 4.5 shows the simulated BER results versus link distance for an example flight path (20 km to 110 km moving away from the base station) for the over-sea setting. These figures show the BER for both RL and FL. In these simulations we applied DME interference and use the actual channel model for the over-sea environment. The channel

---

[2] At least for the BER range shown in Figures 4.2 and 4.3. Later in the final chapter we will show that even FBMC system can have an error-floor. We proposed an algorithm to remove these error-floors, discussed in the final chapter.

model employs three components: LoS, reflected, and intermittent. Note that in Figure 4.5-a, the trend for FBMC without PB (blue curve) is not shown clearly during the entire flight path because it has very low BER (less than 10^{-6}) for most of the link range. The periodic behavior of these figures reflects the primarily two ray behavior of the over-sea channel, with the peaks in the figures corresponding to the low SNR values in Figure 3.5 (CE2R model). According to Figure 4.5 results, at practical SNR values at each distance (Figure 3.5), FBMC has much better performance than L-DACS1. These results show that DME interference can have severe impacts on L-DACS and FBMC communication systems and that FBMC and L-DACS2 are more robust against this interference. Our simulation results also show that the FBMC subcarrier based system has the ability to work without PB and have the best performance among all systems.

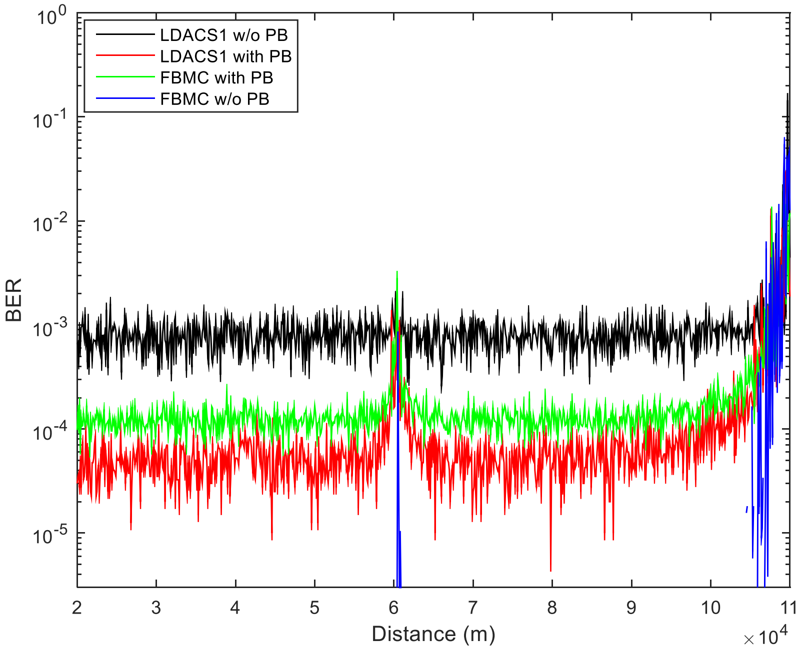

(a)

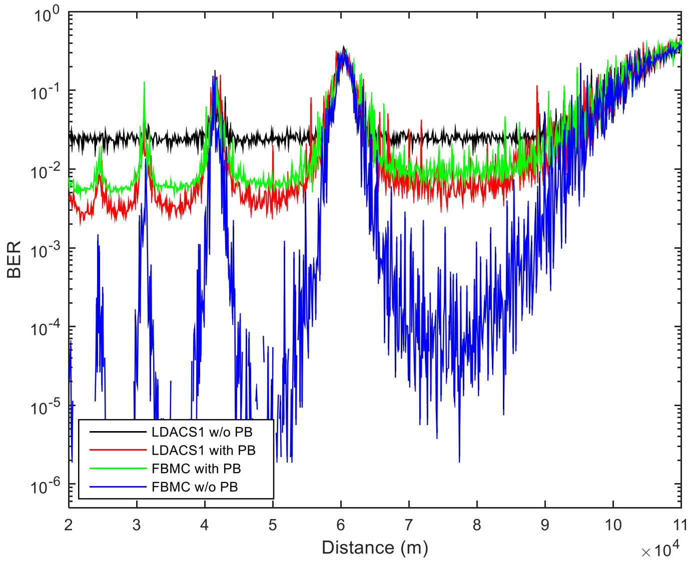

(b)

Figure 4.5. Comparing L-DACS1 and FBMC BER performance with DME interference vs. distance during flight for an over-sea channel for (a) RL scenario, (b) FL scenario.

Next we compare additional characteristics of the FCI systems: PAPR and PSD. For PAPR, as long as the amplitude distribution of two multicarrier system signals, with a large number of subcarriers (e.g., ≥64), is close to that of a Gaussian distribution, then the PAPR distribution is generally nearly identical. This holds true for the PAPR of the FBMC and L-DACS1 systems in the same physical layer conditions. In [82] simulation results for the complementary cumulative distribution function (CCDF) of two multicarrier systems with the same numbers of subcarriers are shown and, accordingly the results are similar for the two types of multicarrier systems. In Figure 4.6 we simulated these PAPR results for L-DACS1 and FBMC, which confirm the results in [82]. L-DACS2 uses continuous phase modulation (CPM) technique and it is known that CPM waveforms have the ideal PAPR value of unity (0 dB), thus in terms of PAPR, L-DACS2 is better than the other two systems.

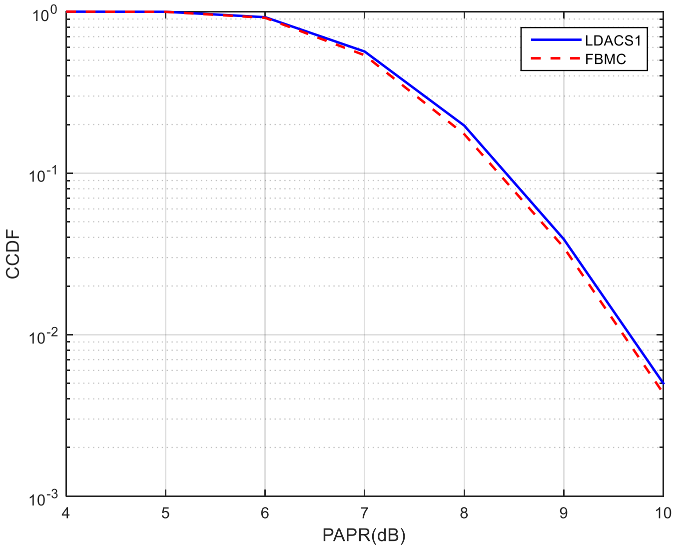

Figure 4.6. Complementary cumulative distribution function (CCDF) of PAPR for L-DACS1 and FBMC.

Figure 4.7 compares the simulated PSDs of these three FCI systems. As shown, the out-of-band (OOB) power of the FBMC signal is lower than that of L-DACS1 (about 80 dB lower at DME center frequencies), which implies much lower interference to adjacent FBMC channels or DME signals. Note that the L-DACS1 PSD result in Fig. 4.7 includes application of the windowing technique. We see that even after windowing, the L-DACS1 OOB PSD is much larger than that of FBMC. Once again this lower OOB power level of FBMC can provide better efficiency by restoring guard subcarriers into data subcarriers. In Figure 4.8 we compare the spectra of L-DACS1, L-DACS2 and FBMC signals. Here we do so for the RL in a frequency division multiplexing (FDM) arrangement, including DME interference spectra. Figure 4.8 shows the PSD of the received signals. Again in these simulations we assumed that the DME and L-DACS communication systems' transmitters and receivers are at the same locations on the ground and in the air.

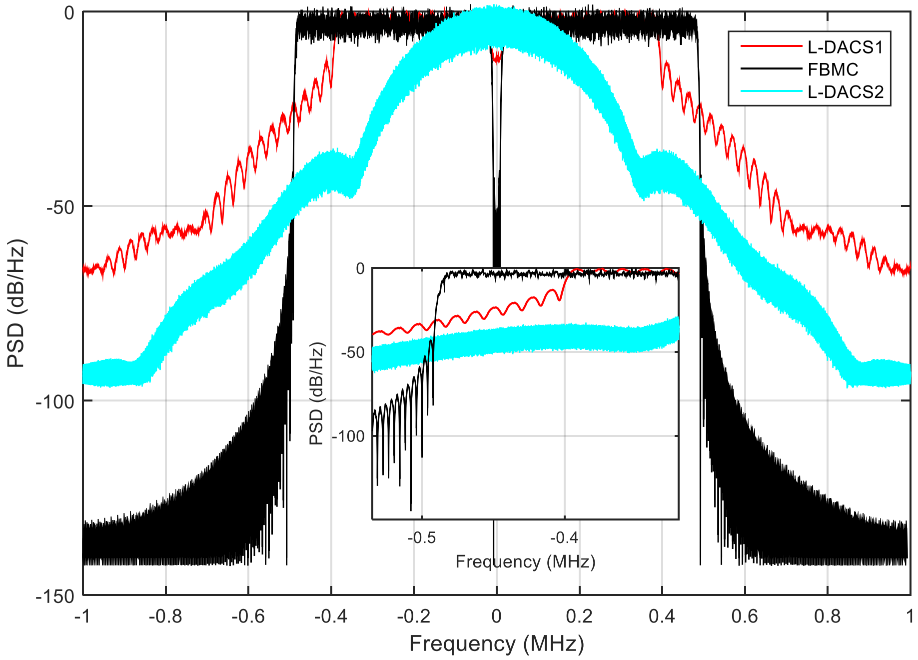

Figure 4.7. PSD of L-band communication systems (including a zoomed version of the plot around channel boundaries).

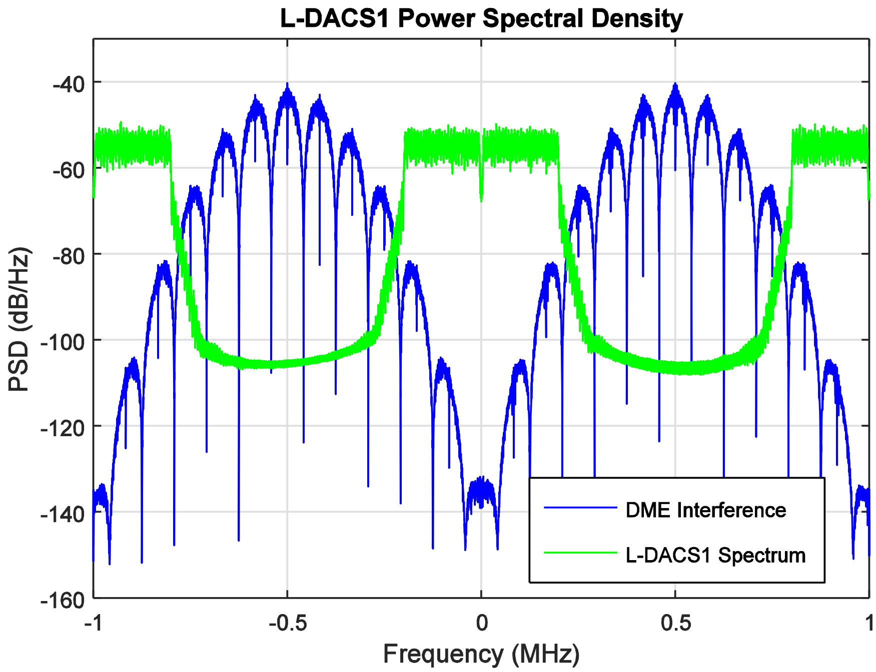

(a)

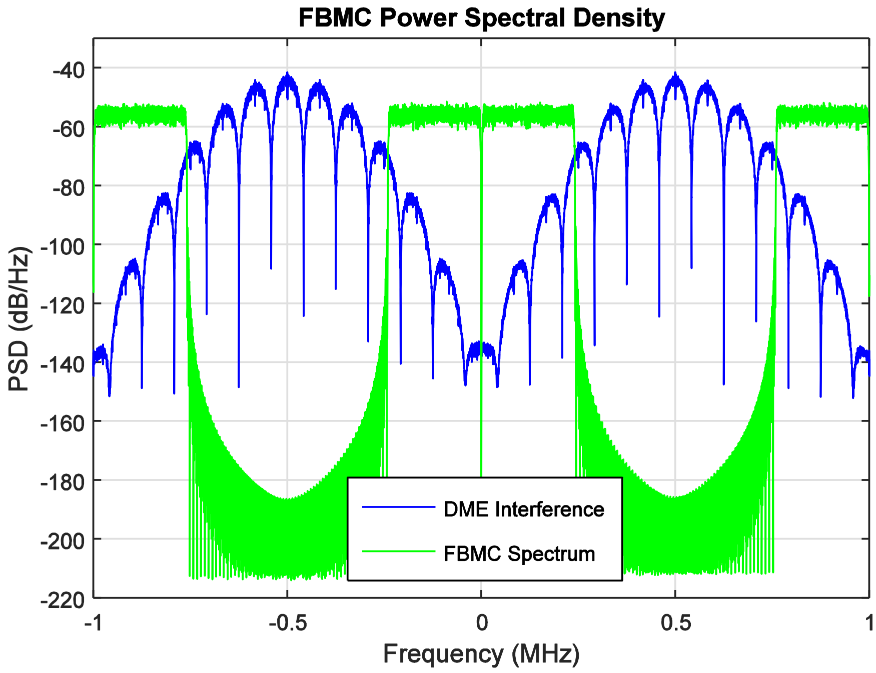

(b)

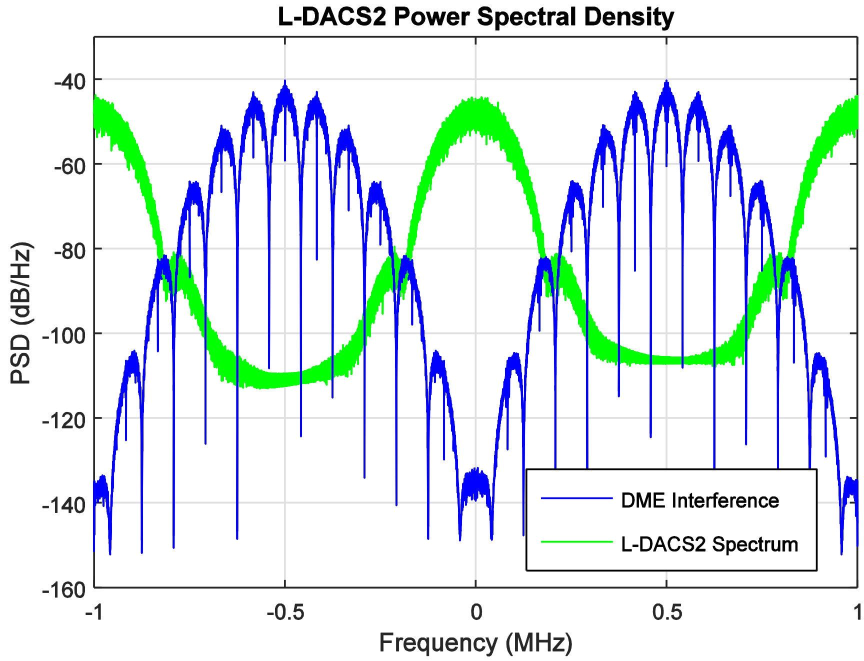

(c)

Figure 4.8. RL power spectral density of three communication systems, (a) L-DACS1 (without windowing) (b) FBMC (c) L-DACS2.

For all these cases the RL DME signal is transmitted with maximum power and pulse rate of 300 W and 150 ppps. Similar to Figure 4.7, the FBMC waveform has much lower OOB signal power (about 80 dB lower than L-DACS1 and L-DACS2 at DME central frequencies), and this reduces the interference to DME (and any other navigation signals in L-band).

Because of the relatively high power of the DME signals, decreasing the number of FBMC guard band subcarriers to 7 compared to the L-DACS1 number of guard subcarriers (13), would not appreciably affect the DME signal even at lower DME power levels. This is essentially because the power of the DME pulses is so much larger than that of the L-DACS1 or FBMC signals (see Figure 4.2).

4.2 COMPARISON OF L-DACS AND FBMC PERFORMANCE IN MORE DISPERSIVE CHANNELS

In this section we show the performance results of L-DACS1 and FBMC for C-band communication systems in more dispersive channels. For C-band AG communication systems we design a new CP-OFDM based communication system based on L-DACS1 which we name C-DACS. In our C-DACS scheme we chose 512 subcarriers with CP length of 88 symbols on the 5 MHz bandwidth signal. Using these parameter values we have the same CP-OFDM symbol length and subcarrier spacing as L-DACS1. We also chose 101 subcarriers as guard band to have spectrum similar to that of L-DACS1. In this case the total length of a C-DACS symbol would be 120 μs with subcarrier spacing equal 5 MHz / 512 = 9.765 kHz. In Table 4.1 we list the physical layer parameters of the CP-OFDM C-DACS system (compare Table 3.2 for L-DACS1).

Another reason we chose these parameter values for C-band AG communication system was to design a close system (with small differences) to 5 MHz airport communication systems (AeroMACS) which will be explained in chapter 6.

Also similar to the L-band FBMC based system we design another FBMC system for C-band. In our C-DACS FBMC system we can also use a small number of guard subcarriers, specifically 7. Therefore for C-band FBMC system we have similar symbol length and power spectrum shape as the L-band FBMC system. In Table 4.2 we list the physical layer parameters of C-DACS system (compare Table 3.3 for L-band FBMC).

Table 4.1. Designed CP-OFDM based C-DACS system physical layer parameters

Total channel bandwidth (kHz)	5000
Occupied Bandwidth, $\boldsymbol{B}$ (kHz)	4013.4
Total # of subcarriers ($\boldsymbol{N_{FFT}}$)	512
Total # of used sub-carriers ($\boldsymbol{N_u}$)	410
Total # of guard band sub-carriers ($\boldsymbol{N_g}$)	101
Subcarrier spacing, $\boldsymbol{\Delta f=B/(N_u+1)}$ (kHz)	9.765
Total Symbol duration $\boldsymbol{T_s}$ (μs)	120
Symbol duration w/o CP, T_{FFT} (μs)	102.4
Total guard time $\boldsymbol{T_g}$ due to CP (μs)	4.8
Raised Cosine (RC) windowing time, T_w (μs)	12.8
Cyclic prefix time, $T_{cp}=T_g+T_w$ (μs)	17.6
RC windowing roll-off factor	0.107

Table 4.2. Designed C-band FBMC system physical layer parameters

Total channel bandwidth (kHz)	5000
Occupied Bandwidth, $\boldsymbol{B}$ (kHz)	4931.3
Total # of subcarriers ($\boldsymbol{N_{FFT}}$)	512
Total # of used sub-carriers ($\boldsymbol{N_u}$)	504
Total # of guard band sub-carriers ($\boldsymbol{N_g}$)	7
Subcarrier spacing, $\boldsymbol{\Delta f=B/(N_u+1)}$ (kHz)	9.765
Total Symbol duration before overlapping $\boldsymbol{T_s}$ (μs)	409.6
Symbol duration after overlapping $\boldsymbol{T}$ (μs)	102.4
Cyclic prefix time, T_{cp} (μs)	0

For simulating these systems, we chose three AG channel environments from the NASA measurement results. These three environments are suburban hilly Latrobe [68], suburban desert Palmdale [68] and mountainous Telluride [67]. For simulating the channel we use the TDL model described in chapter 3. These models are largely “2-ray” models that account for the LOS component, the earth surface reflection, and IMPCs. We include two “suburban” settings because the Palmdale measurements contained some of the largest delay spreads in the entire measurement campaign. Here in Tables 4.3-4.5 we provide the parameter values of C_0, n_y and σ_z for the linear model (3.6) of for the IMPC parameter’s *on probability*, *duration* and *excess delay* for all MPCs. The duration and excess delay parameters include both mean and maxima of measured results. Next, based on the TDL channel generation algorithm explained in chapter 3 we generate the TDL models for the channels and simulate the BER performance.

Table 4.3. Intermittent taps *On Probability* for mountainous and suburban environments

On Probability	Suburban Hilly Latrobe			Suburban Desert Palmdale			Mountainous Telluride		
Tap index	C_0	n_y	σ_z	C_0	n_y	σ_z	C_0	n_y	σ_z
3	0.6496	-0.0876	0.3905	-0.1815	-0.0182	0.6737	-0.1878	-0.0656	0.2717
4	-0.6081	-0.0789	0.3247	-2.1944	-0.0080	0.7339	-2.4519	-0.0669	0.5428
5	-0.8656	-0.0983	0.4638	-3.0757	0.0028	0.8917	-4.0485	-0.0125	0.7560
6	-1.4191	-0.1008	0.5747	-3.3291	0.0069	0.8381	-4.4115	0.0175	0.7352
7	-2.6015	-0.0239	0.4810	-3.4486	-0.0025	0.7064	-22.481	1.2999	0.000
8	-3.6184	0.0284	0.4664	-3.4442	-0.0214	0.5864	NA	NA	NA
9	-4.5347	0.0484	0.6567	-5.8933	0.0427	0.4526	NA	NA	NA

Table 4.4. Intermittent taps *Duration* for mountainous and suburban environments

Duration		Suburban Hilly Latrobe			Suburban Desert Palmdale			Mountainous Telluride		
Tap index		C_0	n_y	σ_z	C_0	n_y	σ_z	C_0	n_y	σ_z
3	Max	2.7216	-0.0728	0.4184	2.5881	-0.0232	0.9143	-2.3326	-0.0632	0.5393
	Mean	0.3919	-0.0326	0.2661	0.6409	-0.0191	0.5227	0.4284	-0.0427	0.3092
4	Max	3.1396	-0.1144	0.5221	2.2730	-0.0236	1.0681	-2.0263	-0.1003	0.7938
	Mean	0.5069	-0.0498	0.3238	0.7173	-0.0162	0.7003	0.6337	-0.0602	0.7240
5	Max	2.8654	-0.1319	0.7041	1.6019	-0.0292	1.1818	-1.9294	-0.1499	1.3366
	Mean	0.2626	-0.0563	0.3633	0.3659	-0.0179	0.6386	0.9363	-0.1133	1.1876
6	Max	2.6607	-0.1475	0.6729	2.3076	-0.0696	1.0785	-0.8044	0.1376	1.4241
	Mean	0.1678	-0.0566	0.2884	1.0368	-0.0533	0.6595	-1.0671	0.1229	1.2419
7	Max	1.7637	-0.0830	0.648	0.7477	-0.0101	0.8169	-5.2714	0.5904	1.3101
	Mean	-0.0059	-0.0431	0.2546	0.0070	-0.0105	0.5438	-3.7099	0.3937	1.1760
8	Max	0.5994	-0.0003	0.3983	0.8133	-0.0407	1.0593	NA	NA	NA
	Mean	-0.5061	-0.0021	0.1938	0.1243	-0.0301	0.7336	NA	NA	NA
9	Max	-0.2685	0.0114	0.8776	4.2692	-0.1671	1.0036	NA	NA	NA
	Mean	-0.9092	0.0060	0.4032	2.5168	-0.1184	0.6578	NA	NA	NA

Table 4.5. Intermittent taps *Excess Delay* for mountainous and suburban environments

Excess Delay		Suburban Hilly Latrobe			Suburban Desert Palmdale			Mountainous Telluride		
Tap index		C_0	n_y	σ_z	C_0	n_y	σ_z	C_0	n_y	σ_z

3	Max	4.4643	-0.0277	0.3176	3.8748	0.0050	0.3848	3.4999	0.0003	0.6499
	Mean	2.6875	0.0034	0.1531	2.8716	0.0032	0.3114	2.2658	0.0008	0.191
4	Max	4.3461	-0.0203	0.2480	3.7422	0.0062	0.3496	3.52	-0.0323	0.5252
	Mean	2.7536	0.0127	0.1146	3.0494	0.0066	0.2924	2.6382	-0.008	0.2960
5	Max	4.3623	-0.0214	0.3145	3.6756	0.0110	0.2851	3.5433	-0.0405	0.5041
	Mean	2.8722	0.0171	0.191	3.2984	0.0067	0.3335	3.0248	-0.02	0.4947
6	Max	4.2931	-0.0200	0.3102	4.0825	-0.0064	0.3587	2.9584	0.0301	0.6315
	Mean	2.9844	0.0197	0.2087	3.6167	-0.0069	0.3135	2.9320	0.0117	0.5765
7	Max	4.1532	-0.0018	0.1973	3.6004	0.0075	0.4065	7.0381	-0.3454	0.2259
	Mean	3.0996	0.0194	0.0729	3.5731	-0.0074	0.2135	7.4870	-0.4059	0.1768
8	Max	3.8656	0.0175	0.2457	2.7830	0.0294	0.3581	NA	NA	NA
	Mean	3.2161	0.0140	0.1323	2.8877	0.0194	0.1886	NA	NA	NA
9	Max	3.6586	0.0227	0.4140	1.6106	0.0683	0.3105	NA	NA	NA
	Mean	3.3889	0.0065	0.2584	1.2064	0.0762	0.1786	NA	NA	NA

In Figures 4.9, 4.10 and 4.11 we show the measured and simulated instantaneous RMS-DS versus link range for one sample flight track (FT) for these C-band channels and 50 MHz signal bandwidth. Note that the bandwidth of signals in the measurements is 50 MHz so we used the same bandwidth for fair comparison. These results show the close resemblance between measured and simulated RMS-DS channel results versus link range. As long as in our C-band FCI communication systems we used 5 MHz bandwidth, in our later BER and RMS-DS simulations we use 5 MHz channel model by combining MPCs in power delay profiles.

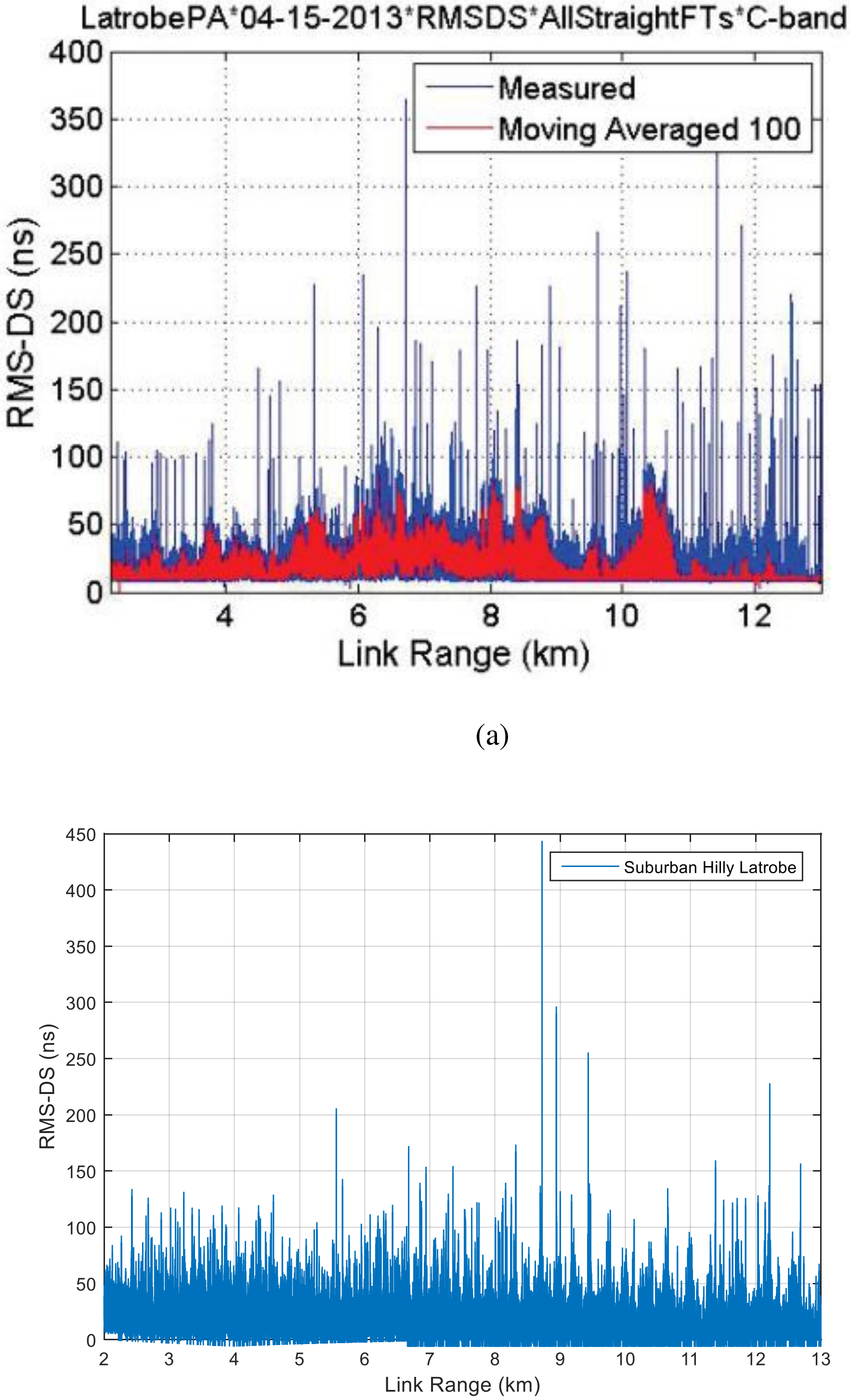

(a)

(b)

Figure 4.9. RMS-DS suburban Hilly Latrobe, (a) Measured, (b) Simulated.

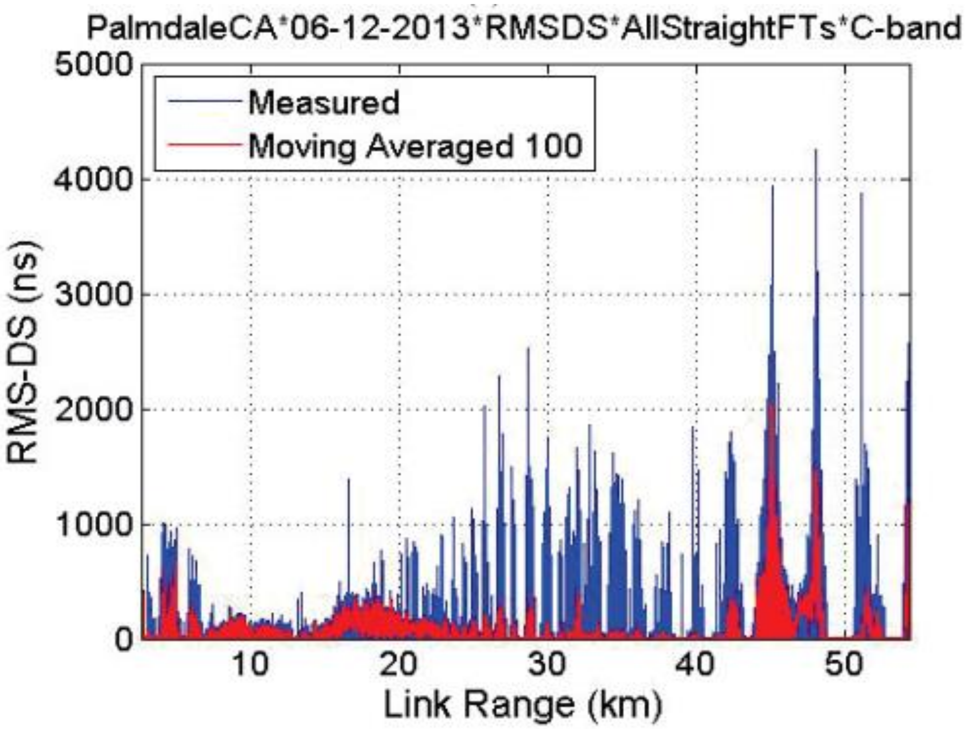

(a)

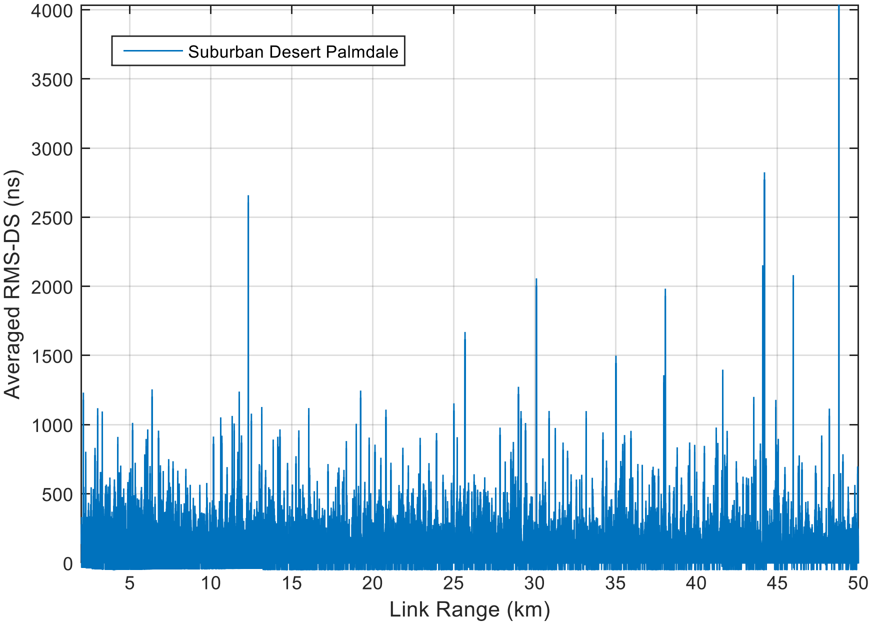

(b)

Figure 4.10. RMS-DS suburban Palmdale, (a) Measured, (b) Simulated.

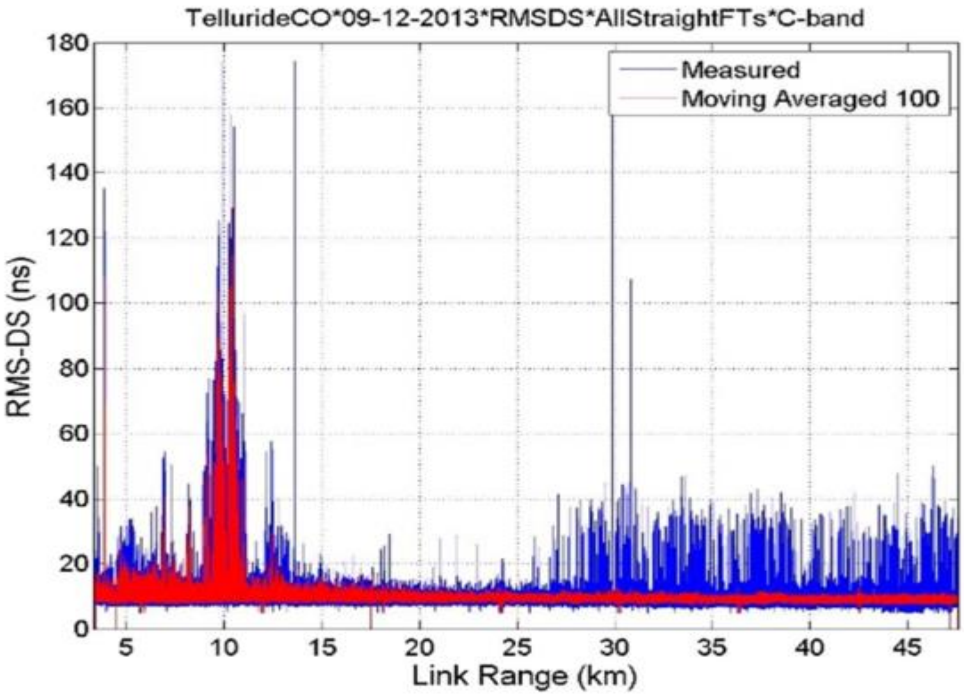

(a)

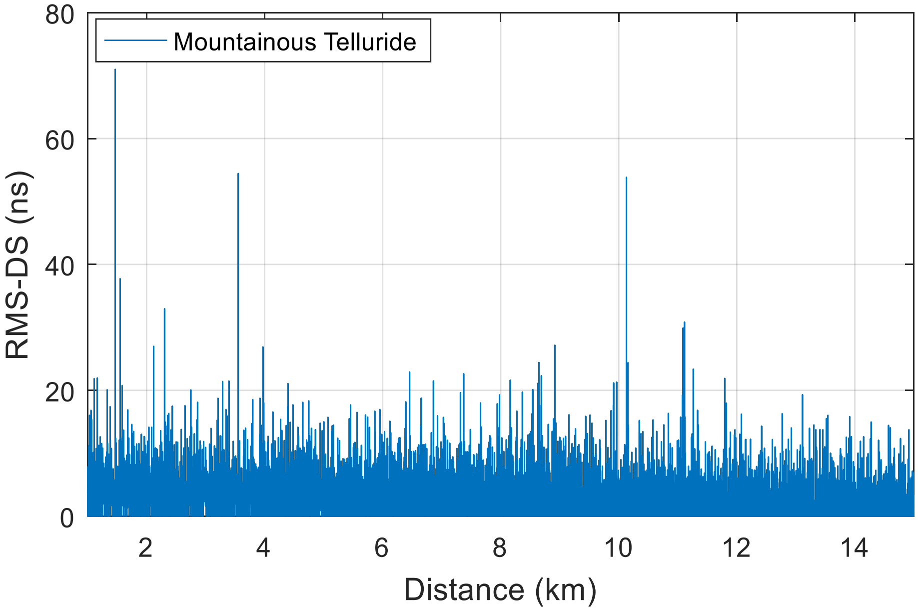

(b)

Figure 4.11. RMS-DS mountainous Telluride, (a) Measured, (b) Simulated.

In order to compare measured and simulated RMS-DS statistics we collected the maximum and mean values of RMS-DS over link range for 10000 iterations. Figures 4.12 and 4.13 show the mean and maximum RMS-DS values versus distance, respectively. Based on these results we can conclude that Suburban Palmdale is more dispersive than Suburban Latrobe and they are both more dispersive than the Mountainous Telluride environment. We also note the general 2-ray behavior of decreasing RMS-DS with distance.

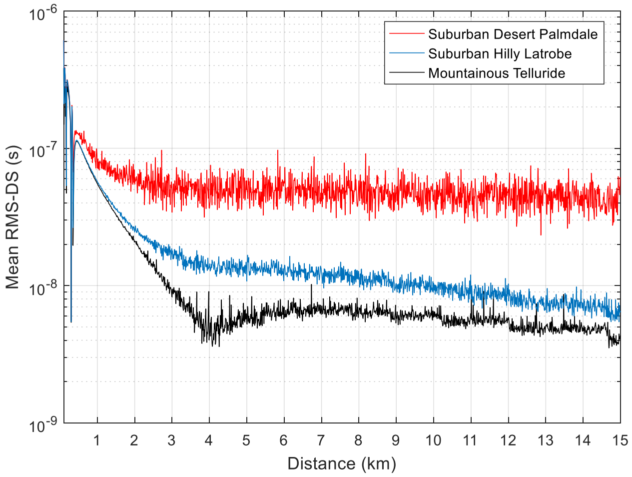

Figure 4.12. Mean value of RMS-DS at each distance for three environments.

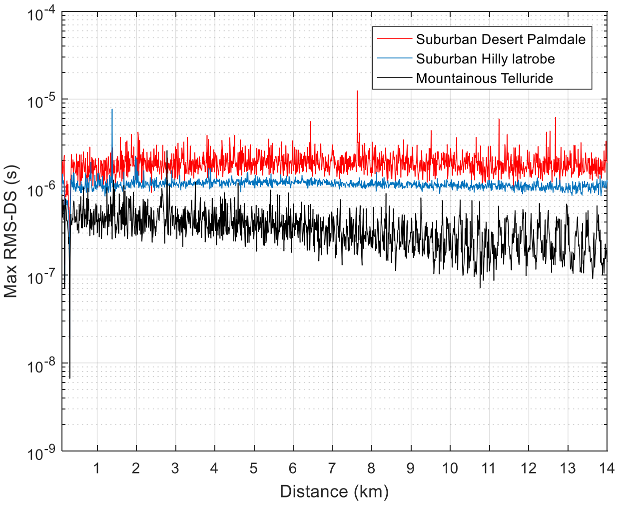

Figure 4.13. Max value of RMS-DS at each distance for three environments.

In Table 4.6 we compare these RMS-DS statistics for all environments. These results validate the simulations.

Table 4.6. Statistical RMS-DS values for measured and simulated results in AG channels

Channel environment	Measured Average RMS-DS (ns)	Simulated Average RMS-DS (ns)	Measured Maximum RMS-DS (ns)	Simulated Maximum RMS-DS (ns)
Suburban Hilly Latrobe	13.9	20.2	1190.8	972.4
Suburban Desert Palmdale	59.8	55.6	4242.9	3235.6
Mountainous Telluride	10.1	14.9	177.4	340.5

In our BER simulations we can chose to create channels with either mean or maximum MPC tap parameter values listed in tables 4.3 to 4.5 for our BER simulations. In our simulations we used the maximum values in order to simulate the worst case situation.

Before showing the BER results we first illustrate PSD results of our C-band FBMC and C-DACS systems in Figure 4.14. As can be observed, similar to L-band FBMC has significantly lower out of band power, and therefore via replacement of many guard subcarriers (at band edges) with data-bearing subcarriers, FBMC attains better spectral efficiency than its C-DACS counterpart. In most of our designs this gain in throughput is approximately 23%.

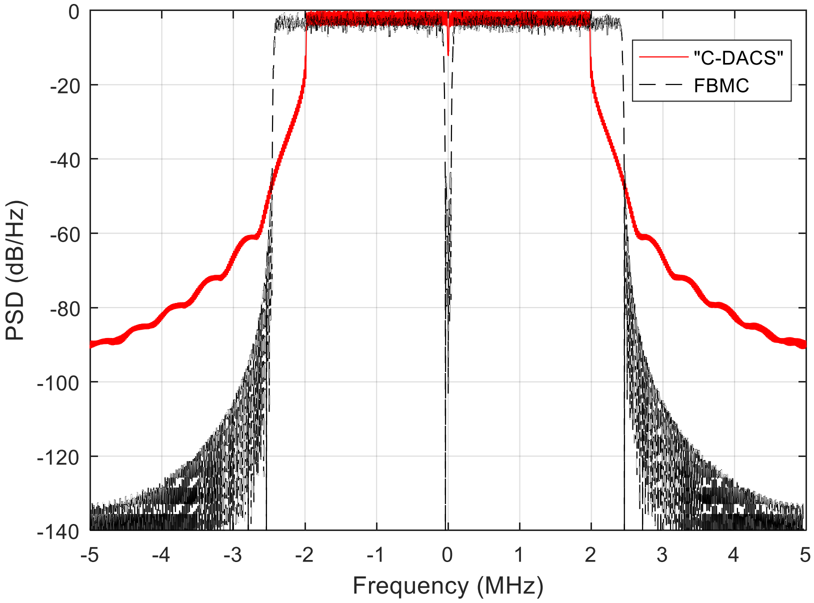

Figure 4.14. C-band FBMC and C-DACS power spectral densities.

Now in Figures 4.15 to 4.20 we compare the BER performance of FBMC and C-DACS communication systems results in these three environments. Each Figure includes BER performance of both systems in the three environments. In order to see the impact of distance on BER results we simulated these results at two different distances, 1 km and 7.5 km. As shown in the results at higher distances BER results get better, and this is consistent with downward trend of RMS-DS results. According to these results we see that the BER performance of Palmdale is worse than Latrobe and they are both worse than Telluride and again this is consistent with RMS-DS results. These results also show that comparing to C-DACS system FBMC system has the same BER performance (with marginally difference) for same modulation order and distance. This is true even for the most dispersive case (desert Palmdale) and with the highest-order modulation of 64 QAM. Hence for these 5 MHz C-band systems, FBMC, with its larger throughput and comparable performance to CP-OFDM, is a very attractive candidate.

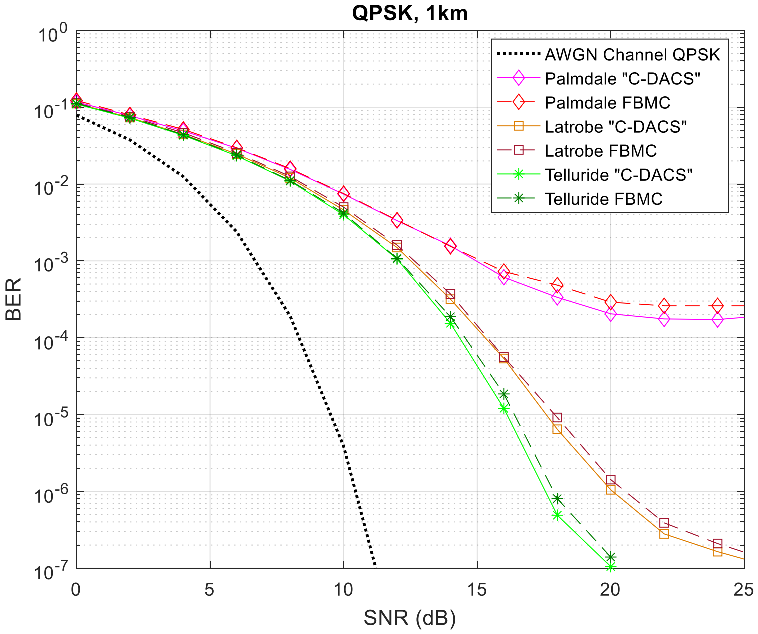

Figure 4.15. BER vs. SNR for C-DACS and FBMC systems in three different AG channel environments at distance 1 km, modulation QPSK and bandwidth 5 MHz.

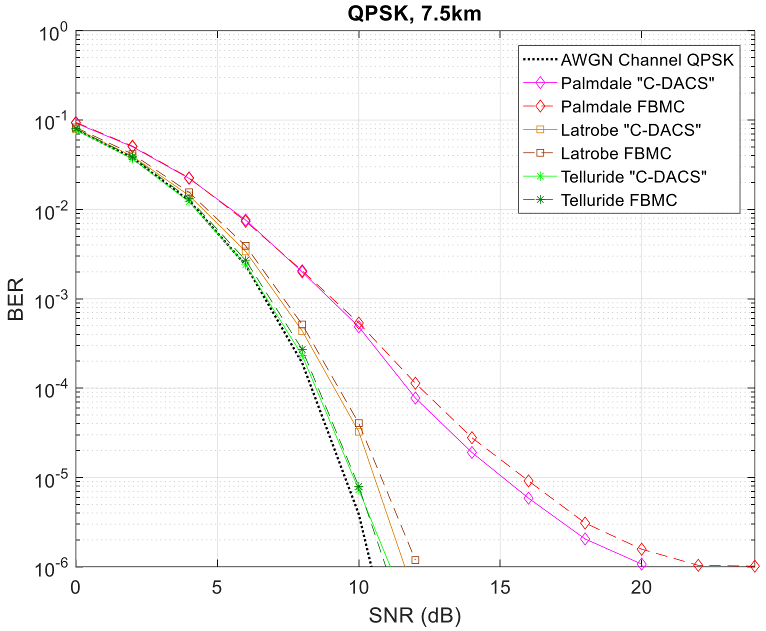

Figure 4.16. BER vs. SNR for C-DACS and FBMC systems in three different AG channel environments at distance 7.5 km, modulation QPSK and bandwidth 5 MHz.

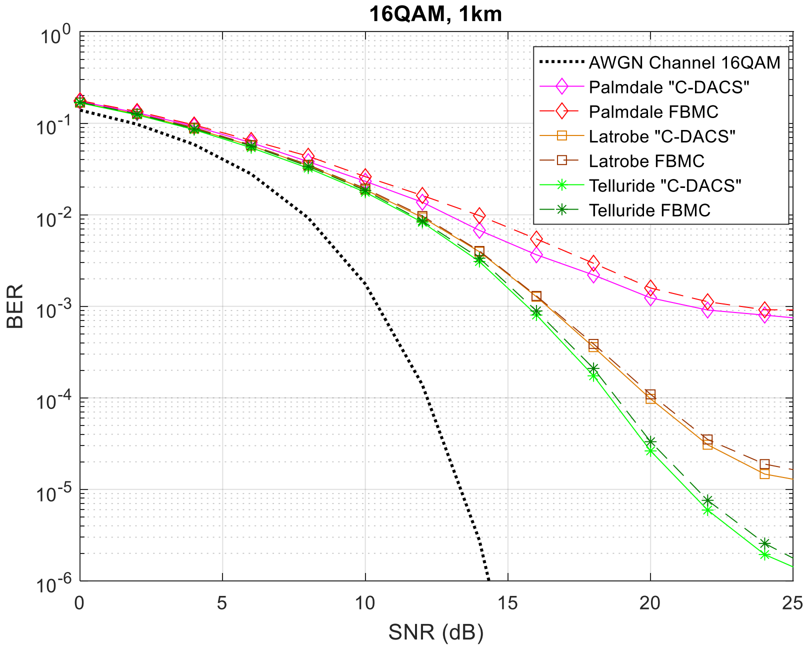

Figure 4.17. BER vs. SNR for DACS and FBMC systems in three different AG channel environments at distance 1 km, modulation 16 QAM and bandwidth 5 MHz.

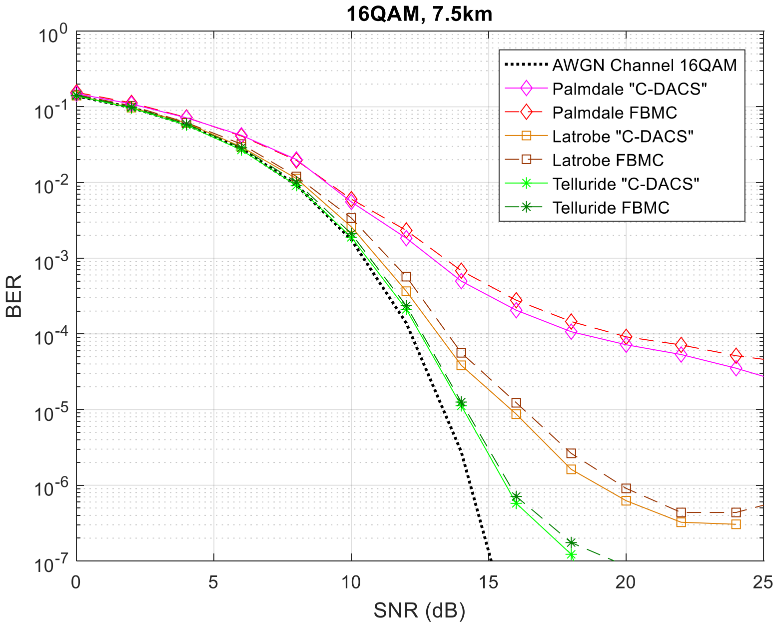

Figure 4.18. BER vs. SNR for DACS and FBMC systems in three different AG channel environments at distance 7.5 km, modulation 16 QAM and bandwidth 5 MHz.

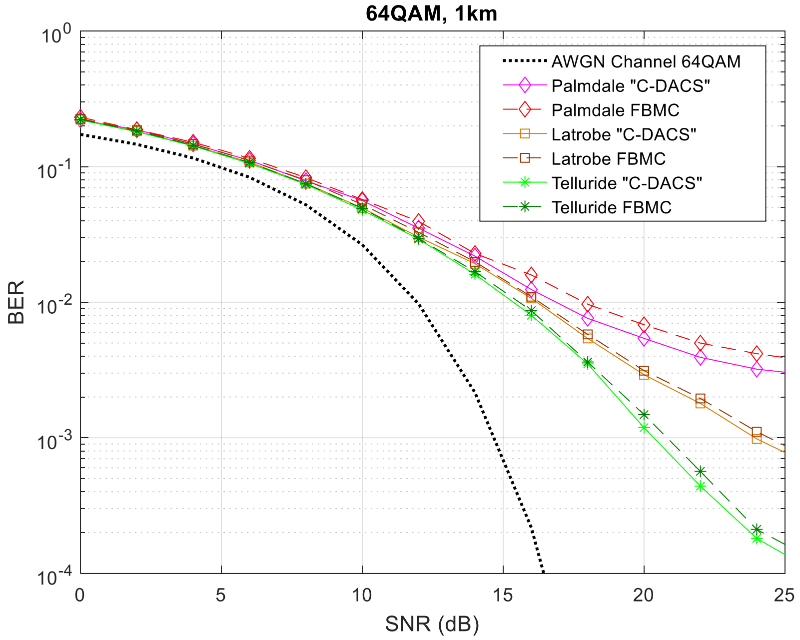

Figure 4.19. BER vs. SNR for DACS and FBMC systems in three different AG channel environments at distance 1 km, modulation 64 QAM and bandwidth 5 MHz.

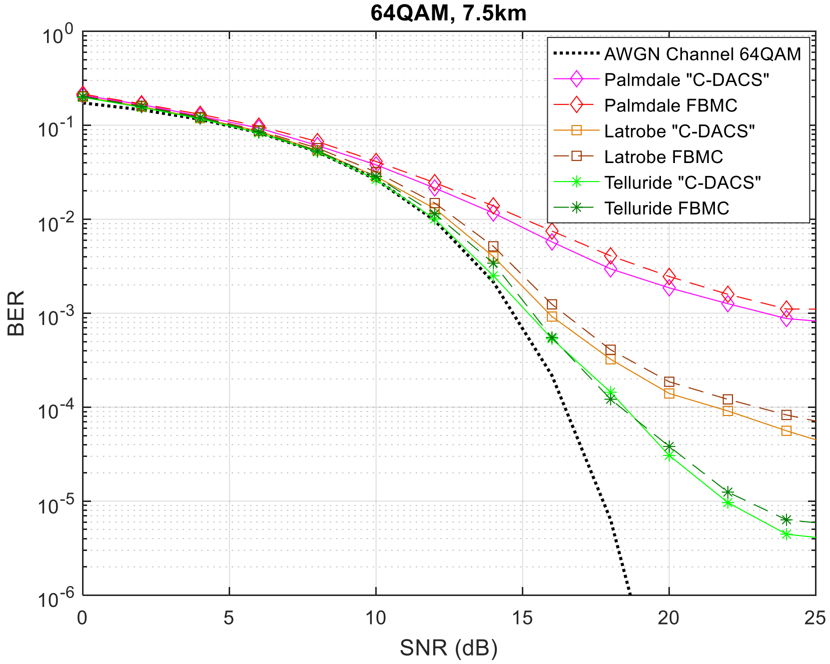

Figure 4.20. BER vs. SNR for DACS and FBMC systems in three different AG channel environments at distance 7.5 km, modulation 64 QAM and bandwidth 5 MHz.

4.3 PERFORMANCE OF L-DACS1 AND FBMC IN THE PRESENCE OF MULTIPLE DME INTERFERERS IN L-BAND

In our results in section 4.3 we only considered the actual dispersive channels without considering any interfering signals. We saw that in different AG environments and at various distances L-DACS1 and FBMC have essentially the same BER performance. In this section we continue analysis of BER performance of FCI systems but now in the presence of DME interference. We consider aircraft within the coverage volume of one cell of an L-band "cellular" network working in the presence of *multiple* DME stations.

In this section we will show the advantage of the L-band FBMC system in suppressing the DME interference from several DME ground stations during a flight path [60]. In our simulations we use the channel model for the suburban (hilly) Latrobe environment. We will compare BER results for L-DACS1 and FBMC systems.

In Figure 4.21 we show the cell coverage areas of two DME channel frequencies, channel 94 (1118 MHz) and channel 95 (1119 MHz), in the northeastern part of the United States; see [83]. We chose this environment near Latrobe, PA since that was one of the locations of the NASA Glenn Research Center channel measurements. We use the TDL model for these suburban channels as described in the last section. According to the geography of these DME stations, we selected two different locations for our L-DACS1 or FBMC ground stations (GS). In the first scenario (Figure 4.21-a), the center point between two DME stations has been selected as the location of the L-DACS1 or FBMC GS. In these figures, green circles show the coverage area of the L-DACS1 or FBMC cell with maximum radius of 370 km based on L-DACS1 specifications [13]. In the second scenario (Figure 4.21-b), the same DME channel 94 location has been selected as the location of the L-DACS1 or FBMC ground station.

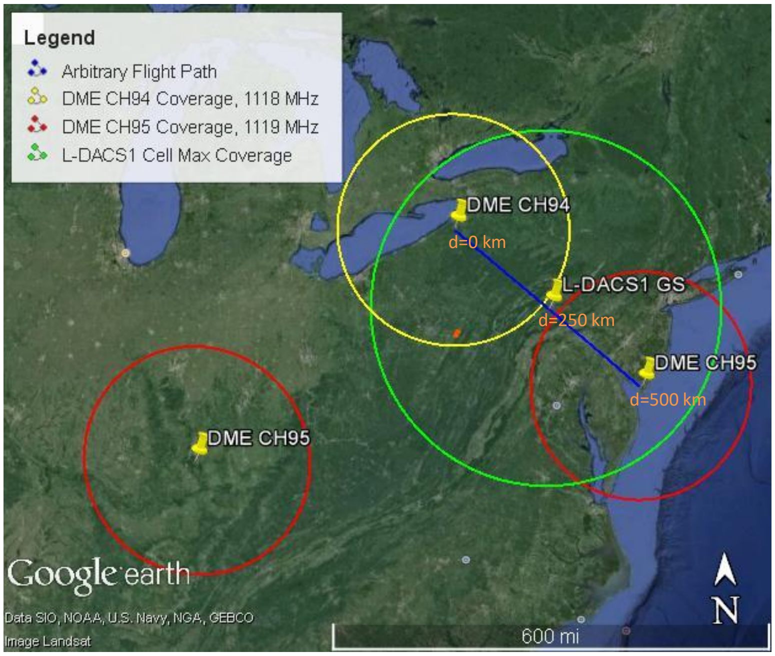

(a)

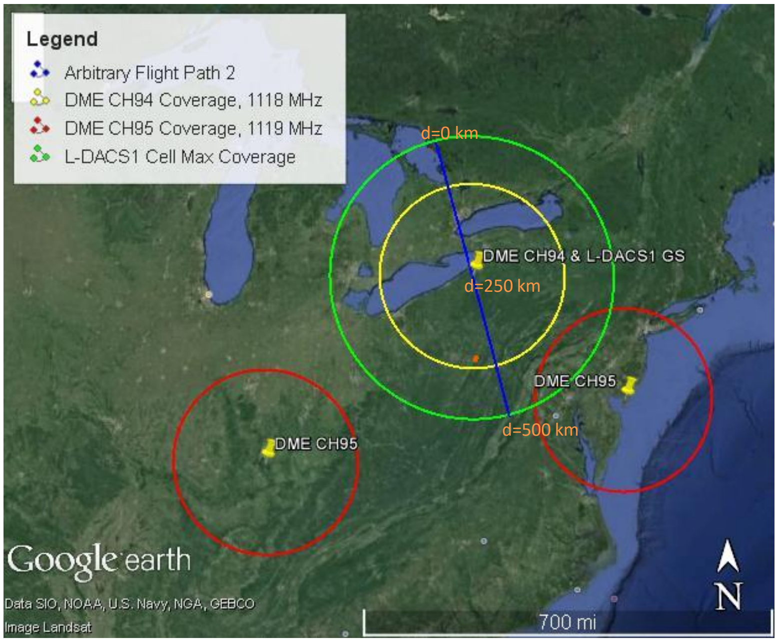

(b)

Figure 4.21. (a) Scenario I, FCI GS Between two DME stations, (b) Scenario II, FCI GS at the same DME CH94 location.

In order to compare the behavior of L-DACS1 and FBMC we selected two arbitrary flight trajectories (blue lines) as our flight paths. In these figures we also see another cell using the DME channel 95, but this cell is out of our simulation line of sight region and we do not consider it in our simulations. In our simulations we investigated both RL and FL communication system performance in the flight trajectories in Figure 4.21. Following the DME specs for forward and reverse links [71], the DME peak pulse power and pulse pair rate are 300 W and 150 ppps for RL, and 1000 W, 2700 ppps for FL. For all the results we used perfect channel information and the zero-forcing equalization technique at the receivers.

In Figures 4.22 (a) and 4.22 (b) we show the BER vs. distance performance results for FL and RL in scenario I. In these simulations we used QPSK modulation for both L-DACS1 and FBMC, with carrier frequency in between DME channels. We chose aircraft altitude at 5 km above the GS to have a line of sight channel at all distances. The GS antenna is 20 m above the ground surface. In these figures DME channel 94 is selected as the geographical reference d=0 km and DME channel 95 is located at d=500 km. The FCI system ground station is located at d=250 km distance from both DME station channels 94 and 95. We see that the BER results degrade as aircraft moves away from the FCI ground station (250 km) in both directions. This is due to the SNR reduction from free space path loss attenuation, as well as the increase in DME interference powers. These figures show that both FCI systems have the same performance for FL, RL communication systems when the FCI ground station is located far from DME stations.

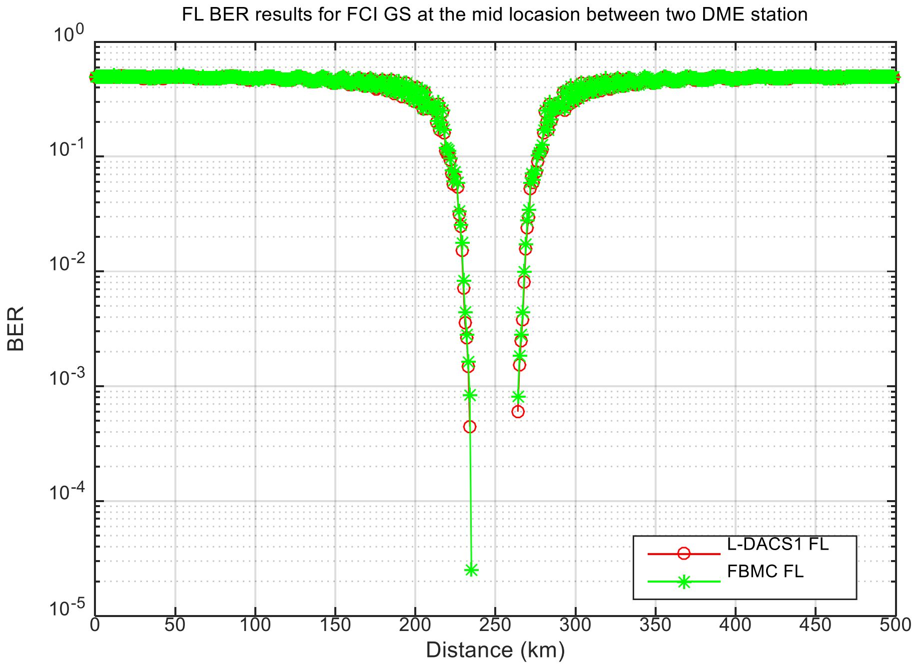

(a)

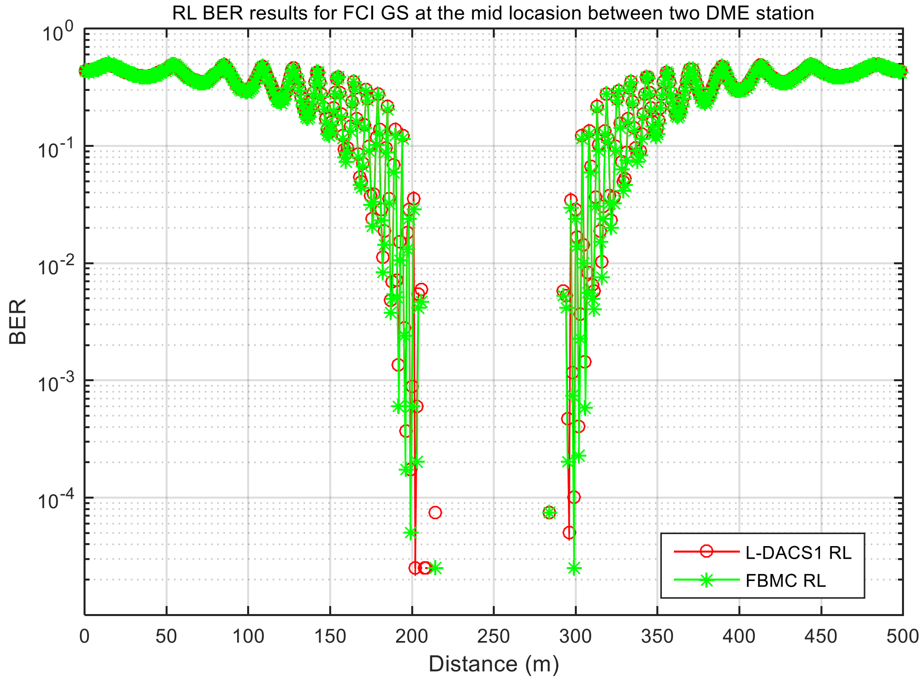

(b)

Figure 4.22. Scenario I, (a) FL BER results, (b) RL BER results, where d=0 km is the location of DME channel 94 and d=250 km is the location of FCI system.

Figures 4.23 (a) and 4.23 (b) show the performance of these systems in the second scenario when the FCI systems ground station is co-located with the DME channel 94 GS. In these figures, distance d=250 km is where the FCI GS and DME channel 94 GS are located. The main difference between this scenario and scenario I is the range of communication. As we see in this situation, larger distances can be covered with much lower error rate than in scenario I. In this scenario FBMC shows its advantage over L-DACS1. Recall that in section 4.1 we provided some results to show that L-DACS1 suffers from an error floor when the two L-DACS1 and DME signals are transmitted from the same location. Here in Figure 4.23, similar to those results in section 4.1, L-DACS1 shows very poor performance in the presence of DME interference.

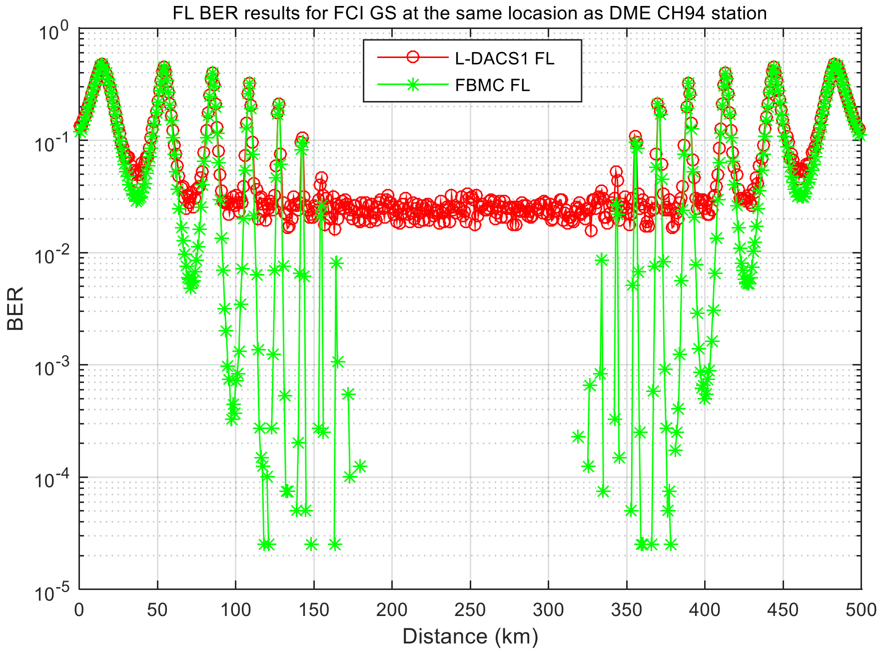

(a)

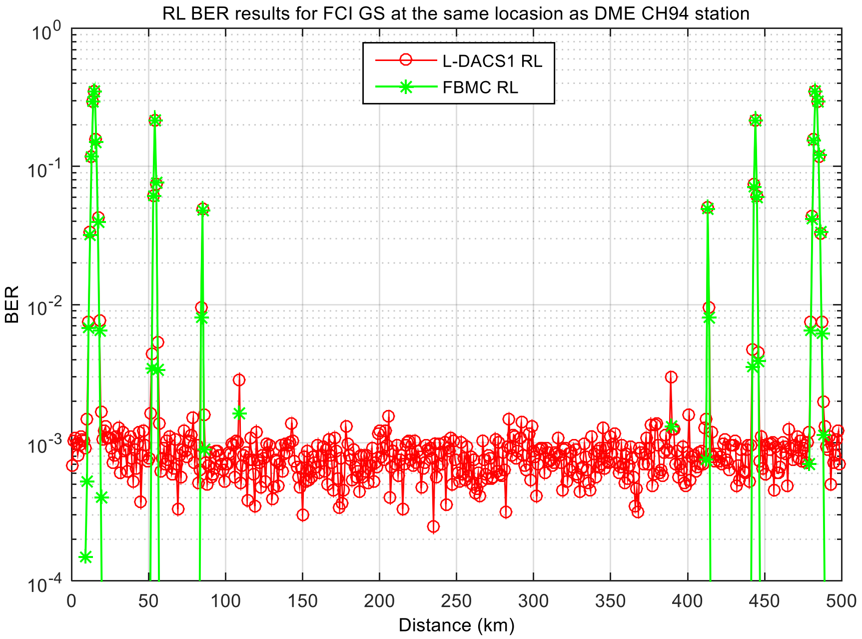

(b)

Figure 4.23. Scenario II, (a) FL BER results, (b) RL BER results, where d=250 km is the location of DME channel 94 and FCI systems as well.

Note that in all these BER results shown in Figure 4.23, the oscillatory effects are due to the two-ray multipath component effect. Also, we see that the RL results are better than those of the FL because the RL has lower power and pulse rate for the DME interference signals. Therefore in an existing DME cellular network, FBMC has better performance than L-DACS1 due to its better subcarrier filtering. Using FBMC can increase the link range. The FBMC AG communication system also has better spectral efficiency due to fewer guard bands, and it has shorter frame lengths in the FL.

CHAPTER 5

L-BAND AIR-TO-GROUND DUAL ANTENNA COMMUNICATION SYSTEM EXAMPLE PERFORMANCE

In one of our works [63], diversity and multiple antenna techniques for L-band AG communication systems were investigated. The advantages of using multiple antennas at the receiver are well-known for uncorrelated channels on the multiple antennas. Multiple antennas at the transmitter and/or the receiver can be used to provide additional diversity (spatial, frequency or etc.) against fading on the radio channel. Our simulation results in this chapter show that in L-band communication systems we can have the spatial diversity at lower distances mainly due to the 2-ray effect of the AG channel. In [96] we have shown that in AG channels it is also possible to achieve frequency diversity by sending the same signal with different frequencies on transmitter antennas, but in this chapter in order to follow the L-DACS1 frequency allocation requirements we only investigate the spatial diversity by just changing the position of the transmitter/receiver antennas with the same signal frequencies.

In this chapter the correlation coefficient between realistic receiver aircraft antenna channels was computed, and using these realistic channels (again, based upon NASA channel measurements) link performance was simulated to generate BER results. The realistic AG channel is essentially the two-ray channel with additional small-scale fading. Based upon the correlation coefficient results, required antenna separations (as a function of link distance) for nearly uncorrelated channels can be computed.

Using the channel model described in last chapter, we computed the correlation coefficient (CC) values of signals received on two different antennas (single transmitter antenna, i.e., single input, multiple output (SIMO)) for different receiver antenna separation (Δd) values and different link distances. Figure 5.1 shows the CC results for L-band signal with 0.5 MHz bandwidth signal, GS antenna height 20 m and aircraft altitude 1 km. Note that in our MIMO simulations we considered the second transmitter antenna with 4 m higher height than the first antenna. In these results we used curved earth two ray model as earth surface model. Also the radio frequency used in these simulations is 985.5 MHz. We computed these CC results based on a 20 m stationarity distance (SD) approximating that in [67]. The SD is the distance over which the channel can be considered wide-sense stationary.

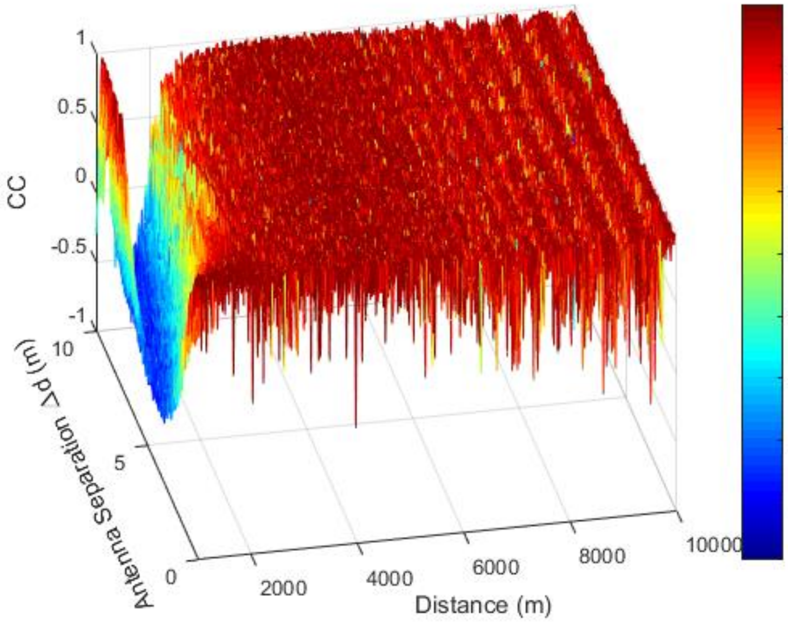

(a)

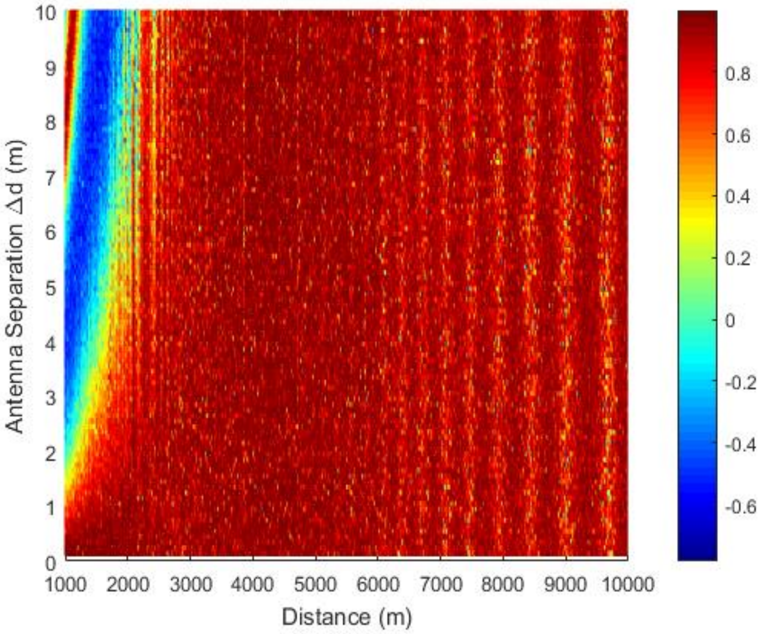

(b)

Figure 5.1. Correlation coefficient (CC) values between two separate receiver antennas, vs. distance and antenna separation, with stationarity distance= 20 m: (a) vs. both link distance and antenna separation; (b) contour plot of (a) at L-band.

We notice several points from the CC plots. The CC results reflect the two ray channel effect especially at smaller distances. These results—because they are largely two-ray results—are strongly dependent on geometry, and vary with GS antenna height, aircraft altitude, and earth surface type. For the particular link parameters used for Fig. 5.1, at larger distances, received signals are highly correlated and this shows that we cannot get much diversity gain by changing receiver antenna separation. Thus we would need other diversity techniques—such as different carrier frequencies—at large link distances to obtain diversity gain. At shorter distances (less than 2 km) there are some areas in which the CC values are low, and this gives rise to the idea of changing the receiver antenna separation dynamically with distance to obtain diversity. In order to approximate this technique practically one might adjust the distance of the receiver antennas on the aircraft (or ground station) in order to find the maximum spatial diversity.

In [63] we compared the BER results for forward link (GS to aircraft) signals at two different example distances from the GS in the two different suburban environments. The L-band carrier frequency used in these simulations is 985.5 MHz and the GS transmitter power is equal to 10 W (the L-DACS1 specification value). In our simulations we assumed the aircraft is located at 1 km height above the earth at distance *d* km from the GS. For our multiple antenna situations we used multiple input, single output (MISO) with 2 transmitter and 1 receiver antenna, single input, multiple output (SIMO) with 1 transmitter and 2 receiver antennas, and multiple input, multiple output (MIMO) with 2 transmitter and 2 receiver antennas. We compared performance at two different distances, 1.5 km and 20 km, corresponding to example "short" and "long" distances from the GS. All other physical layer parameters have been used based on L-DACS1 and FBMC parameters previously provided.

In Figures 5.2 (a), 5.2 (b) we show BER vs. SNR for suburban hilly Latrobe and suburban desert Palmdale, respectively. The TDL models of these environments account for the ground reflected signals and maximum number of MPCs; channel parameters are listed in tables 4.4 and 4.5. For these results we used perfect channel information at the receivers. The assumption is that transmit power is varied, but never exceeds the maximum allowed value of 10 W. For the detection methods at receivers we used the maximal ratio combining (MRC) technique in SIMO and the Alamouti coding technique [93] for both MISO and MIMO systems.

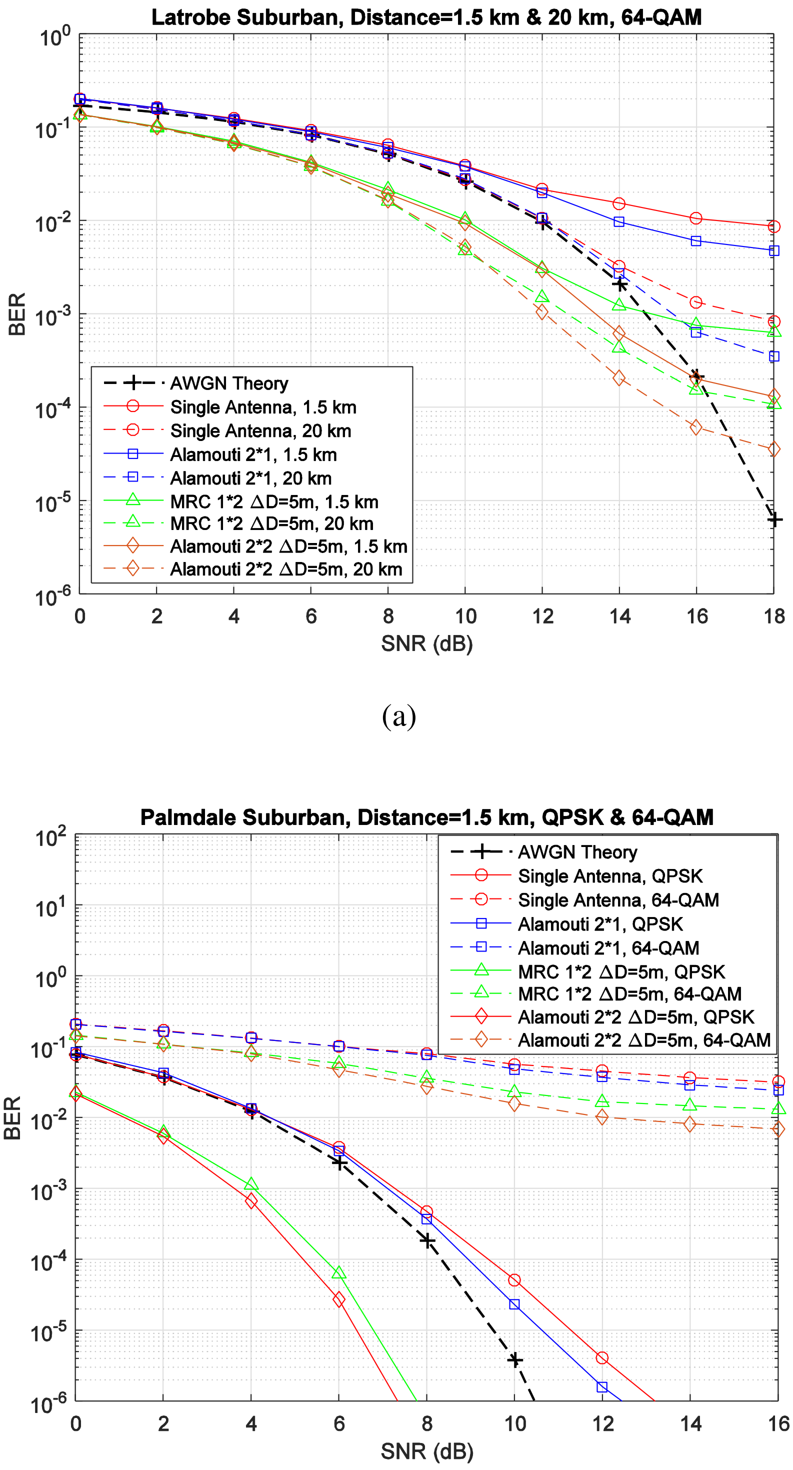

(a)

(b)

Figure 5.2. (a) Latrobe BER results 64-QAM at 1.5 km and 20 km, (b) Palmdale BER results: QPSK and 64-QAM at 1.5 km.

Note that for Latrobe the SISO QPSK BER results attain the theoretical AWGN result, hence we do not plot them here. The BER results of multiple antenna techniques are also in agreement with theory in AWGN channel: MISO has exactly the same performance as single antenna, and SIMO and MIMO techniques have the same BER results with a $10log_{10}(N_R)$ dB shift to the left from the AWGN result, where N_R is the number of receiver antennas (2 in our case). This represents the maximum potential gain in SNR using multiple antennas. For suburban desert Palmdale, worse performance results due to its larger RMS-DS values. For both environments, as modulation order increases, the performance deviates from theoretical, and this is due to channel dispersion. In Figure 5.2 (a) for comparison we plot the 64-QAM BER results for Latrobe at 20 km (longer distance) to show that the performance gets better at longer distances; as previously noted, this is expected since the channel dispersion generally decreases as distance increases. Also note that in these results at different distances best antenna separation (Δd) which result to maximum diversity gain would change.

In order to corroborate the correlation coefficient results with our communication performance results, in Figure 5.3 we show figures for BER and CC together, at two different sample distances (1 km and 1.5 km), for an aircraft height 2 km, GS height 20 m. At each distance these BER results have been simulated and averaged for the Latrobe channel for the same stationarity distance of 20 m, SNR value 12 dB, 64-QAM and a SIMO 1×2 communication system. We see that the average BER results essentially follow the CC results, and at Δd values where the CC values are close to +1 (highly correlated channels) the average BER results are maximum, hence corroborating the close connection between channel correlation and communication system performance.

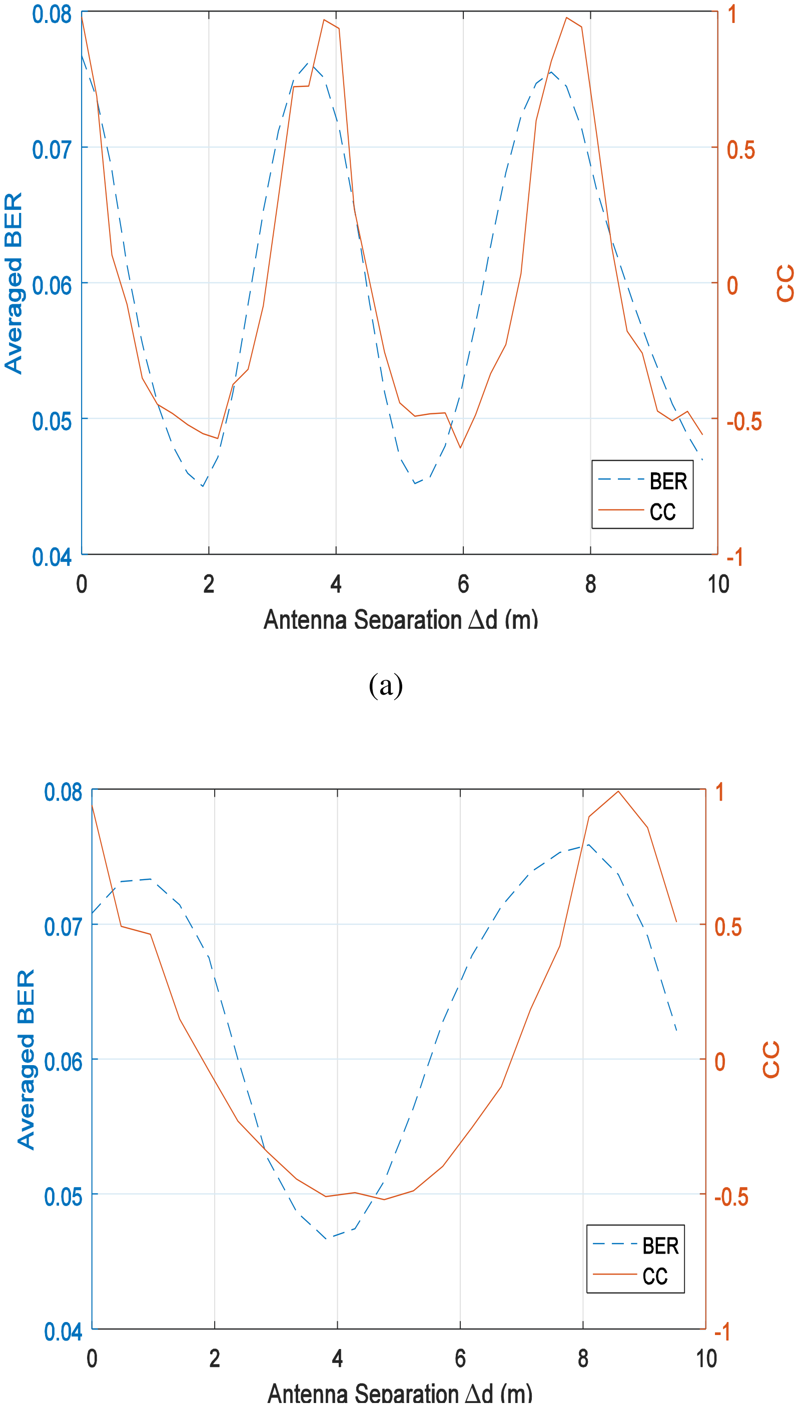

Figure 5.3. Comparison of average BER and correlation coefficient results vs. antenna separation Δd for stationarity distance= 20 m, SNR=12 dB, 64 QAM, 1×2 SIMO, in Latrobe: (a) CC and average BER vs. Δd at distance= 1 km; (b) CC and average BER vs Δd at distance= 1.5 km.

In summary, in this chapter we investigated multiple antenna and diversity techniques in L-DACS1 communication systems, in example suburban AG channels. We showed that for two suburban environments, varying the receiver antenna separation can provide diversity gains at short link distances, whereas at higher distances the diversity remains low. Simulation results showed the advantages of using diversity techniques especially for higher order modulations in AG multicarrier communication systems at short link distances. As one practical example of using multiple antennas could be in UAS.

CHAPTER 6

C-BAND FBMC FOR AIRPORT SURFACE ENVIRONMENTS

6.1 INTRODUCTION AND SYSTEM MODELS

Airport surface area (ASA) environments are one of the areas in which rapid development of communication systems is taking place. Several years ago the Federal Aviation Administration, EUROCONTROL, and the International Civil Aviation Organization proposed a communication system based on IEEE 802.16e standard which was also used in worldwide interoperability for microwave access (WiMAX) technology for airport surface areas: AeroMACS. WiMAX is a broadband wireless data communications technology based on IEEE 802.16 standard providing high speed data over a wide area. In [65] we investigated a new FBMC communication system for the unique airport surface environment. Analogous to our studies and designs for AG settings, our FBMC airport surface system has physical layer specifications similar to the CP-OFDM approach used in AeroMACS. Via computer simulations, using airport surface area channel models based on measured data collected by NASA Glenn Research Center, we illustrate the FBMC advantages over AeroMACS. By using FBMC we can significantly improve the spectrum emission mask (SEM), and by doing so, increase spectral efficiency and reduce interference to both adjacent ASA channels and adjacent band systems.

As we will describe, our results show that when using either zero-forcing or least-square (LS) channel estimation techniques, FBMC has slightly worse BER performance than AeroMACS, mainly at high SNR values, but FBMC still offers a considerable throughput advantage. Again based on the proposed FBMC design, throughput can be increased by approximately 23 percent.

AeroMACS is an all-IP network system with single cell coverage of approximately 8.3 km, sufficient for even large airport environments. Each AeroMACS channel has 5 MHz bandwidth; future applications may allow 10 MHz channels. AeroMACS employs time division duplexing (TDD) to allow more efficient support of asymmetric traffic, with a fixed frame length. Its time domain symbols are modulated using the CP-OFDM technique. The mask specified in [27] for AeroMACS transmitters is the SEM identified in the FCC Code of Federal Regulations (CFR) 47 Part 90.210 [84]. The half bandwidth emission mask for 5 MHz AeroMACS channels is provided in Figure 6.1.

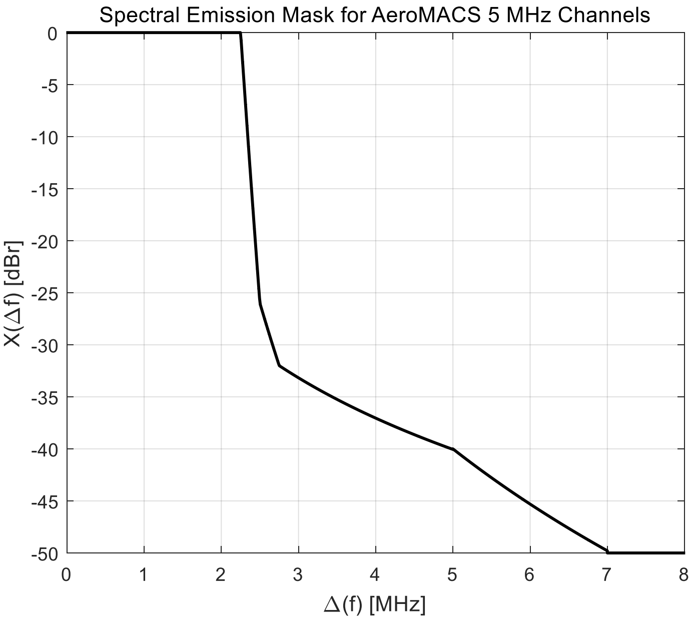

Figure 6.1. Spectral emission mask of AeroMACS transmitter.

In Figure 6.2 the AeroMACS subcarrier structure of the CP-OFDM frequency domain symbols is shown. In this structure, similar to other CP-OFDM systems, different types of subcarriers are used for different purposes, such as pilots for channel equalization and nulls for guard bands. The primary channel allocation plan for AeroMACS systems is shown in Figure 6.3. This includes 5-MHz channels on equally spaced center frequencies from 5095 to 5145 MHz. The location of AeroMACS channels takes into consideration a number of factors. Among those are efficient utilization of current and potential future spectrum allocations, and guard bands to limit OOB radiated power. Assuming coordination with other aviation allocations in the band directly below 5091 MHz (to limit the effects of interference) enables up to 11 separate AeroMACS channels [10] (i.e., the lowest-frequency channel in Figure 6.3 is not used). Other physical layer parameters of the 5 MHz bandwidth AeroMACS signals are listed in Table 6.1. We also include the physical layer parameters of our designed FBMC system in this table for comparison. The main physical layer characteristics of the proposed FBMC system are the same as AeroMACS, with just a few differences.

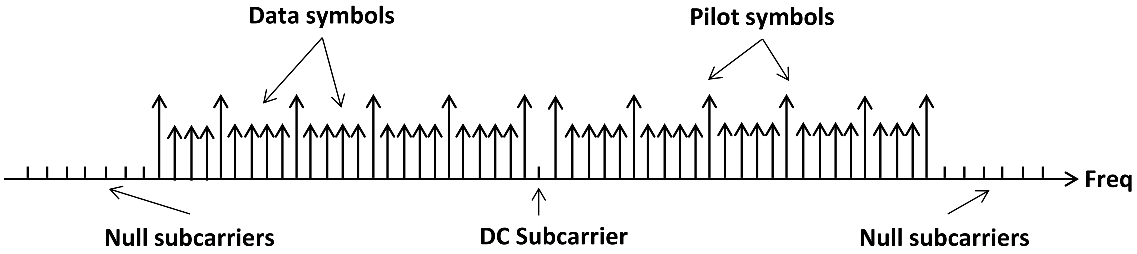

Figure 6.2. AeroMACS CP-OFDM subcarriers structure in frequency domain.

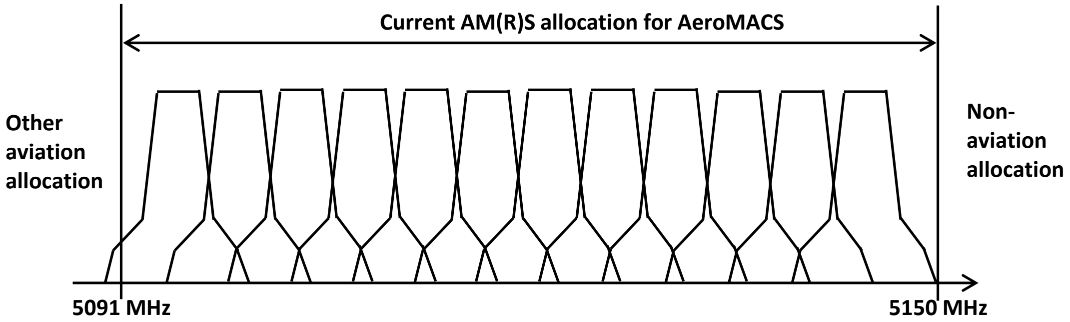

Figure 6.3. Proposed AeroMACS channel plan for 5091-5150 MHz allocation.

Table 6.1. AeroMACS and FBMC physical layer parameters.

Parameters	AeroMACS	FBMC
Channel bandwidth (MHz)	5 (or 10 later)	5/10
# subcarriers (N_{FFT})	512	512
# pilot subcarriers	16	16
# Null subcarriers	103 (52 left, 51 right)+1 DC	7 (4 left, 3 right)+ 1 DC
FFT length, T_{FFT} (μs)	102.4	102.4
Cyclic prefix length, C_P (μs)	$C_p=T_{FFT}/8$ = 12.8	0
Total symbol length, T_s (μs)	115.2	409.6
Frame length, T_f (ms)	5	4.915
Subcarrier spacing (kHz)	9.765	9.765
Modulation types	QPSK, 16-QAM, 64-QAM	QPSK, 16-QAM, 64-QAM
Coding	Rate 1/2, 2/3, 3/4 Convolutional/Turbo	Rate 1/2, 2/3, 3/4 Convolutional/Turbo

Also for FBMC based AeroMACS communications systems we used the SMT based FBMC technique. In AeroMACS, out of the 512 subcarriers in a 5 MHz bandwidth, more than 100 subcarriers are guard subcarriers; this is required to satisfy the SEM. As we will show, in our FBMC communication system we can decrease the number of guard subcarriers to fewer than 10, and attain a better SEM and this simultaneously increases throughput significantly.

As shown in Table 6.1, the main physical layer characteristics of the proposed FBMC system are the same as AeroMACS, with just a few differences. The first difference is the number of null subcarriers. In our FBMC system design, in addition to the DC null subcarrier, we use 4 and 3 null (guard) subcarriers on the left and right sides of the spectrum, respectively. The second difference is due to the CP. As mentioned, in FBMC there is no CP, therefore for the same number of transmitted symbols, the length of the total frame is less than that of the AeroMACS signal. The actual total FBMC frame length depends on the prototype filter length and the so-called overlapping factor. For example, in this FBMC system, similar to the L-band FBMC systems we designed, the prototype filter defined in the PHYDYAS project with overlapping factor K=4 [85] was used. In this case the total frame length of our FBMC signals would be slightly larger than that of the CP-OFDM signal before its added CP. Yet since FBMC does not use a CP, even after using long prototype filters (4 symbol durations for the PHYDYAS filter), the FBMC frame lengths are shorter than those of the AeroMACS signals. In summary, for overlapping factor K=4, each FBMC symbol has length 4 times the FFT length (T_s=409.6 μs) and after overlapping symbols, the total frame length is 153.6 μs less than the AeroMACS frame length (T_f=4.915 ms in FBMC).

6.2 AIRPORT SURFACE CHANNEL MODELS

The channel models that we used in our simulations are those based on the channel measurement and modeling campaign conducted by NASA Glenn Research Center for the airport surface environment in the 5-GHz band [86]. In [86], the large airport surface channel was classified into different propagation regions.

We used the Miami International Airport (MIA) and non-line-of-sight (NLOS) case in our simulations, as this is the worst case (most dispersive). We point out that the airport surface channel is somewhat unique, especially in some large airports like Miami. In these settings, the relatively open ASA property is nearly surrounded by large buildings, metallic warehouses, etc., while the ASA itself is populated by numerous large metallic aircraft and ground vehicles moving about [86]. Maximum delay spreads reach nearly 2.4 μs, with mean values nearly 1.5 μs, and 90th percentile values 1.7 μs [27].

In Figure 6.4 we show two simulated sequences of PDPs for 5 and 10 MHz bandwidth channels over multiple frame times. According to the channel specifications in [86] for 5 and 10 MHz bandwidths, we have 8 and 14 MPCs, respectively, including the first MPC. In Figure 6.4 the power delay profile (PDP) lengths in time domain are ~100 µs and ~50 µs for 5 MHz and 10 MHz channel bandwidths, respectively.

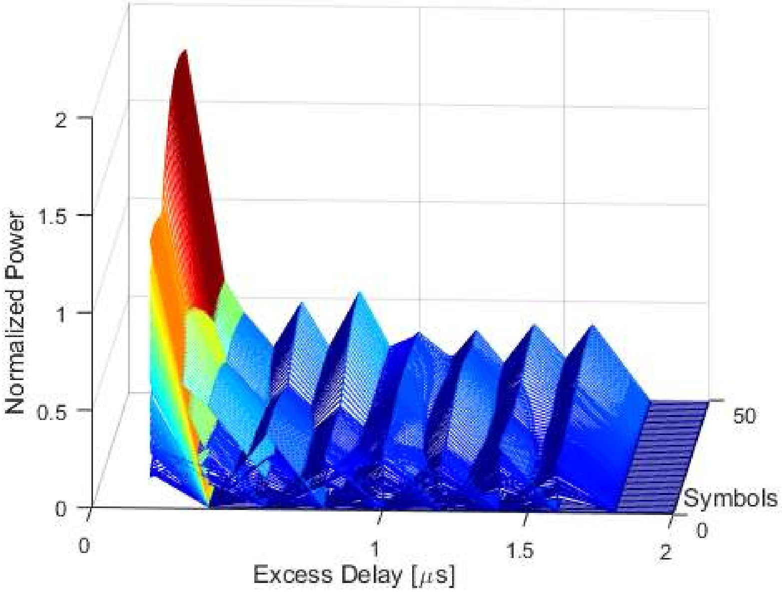

(a)

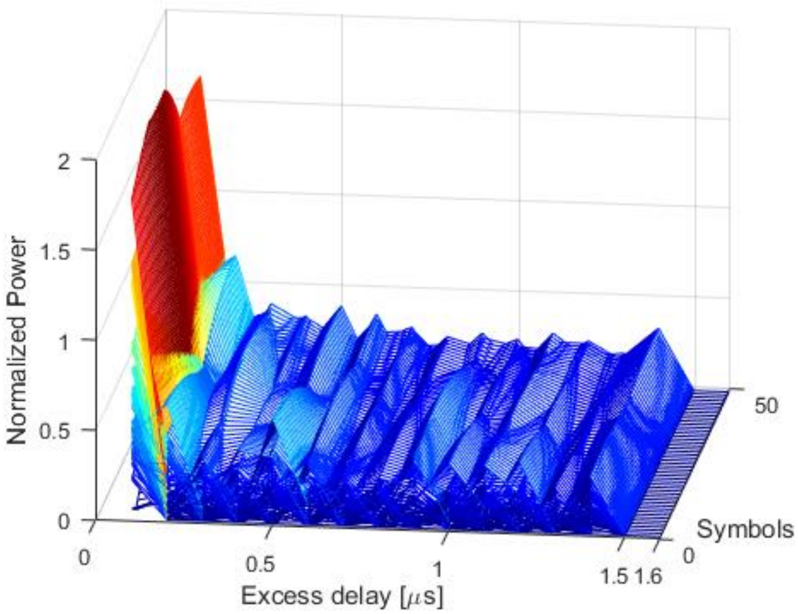

(b)

Figure 6.4. Example power delay profiles of channels in MIA, (a) BW=5 MHz, (b) BW=10 MHz.

6.3 SIMULATION RESULTS

In our simulations we used the physical layer parameters provided in Table 6.1, over the channel models described in the previous section. Figure 6.5 shows the relative power spectral densities of the two communication systems. Again, similar to the L-band schemes L-DACS1 and our L-band FBMC system, for calculating these PSD results we used the periodogram technique. These results show that using fewer null subcarriers in FBMC provides a wider bandwidth for data transmission while still satisfying the SEM requirement (Figure 6.1). These results also illustrate that the OOB power in FBMC is *much* less than in AeroMACS: it is more than 25 dB lower than AeroMACS at the boundary of the next adjacent channels. The relative adjacent channel powers approximately equal -55 dBr for AeroMACS and -118 dBr for FBMC. These values are total out-of-band integration of power of center FBMC or AeroMACS channel over two adjacent similar communication systems with the same channel powers.

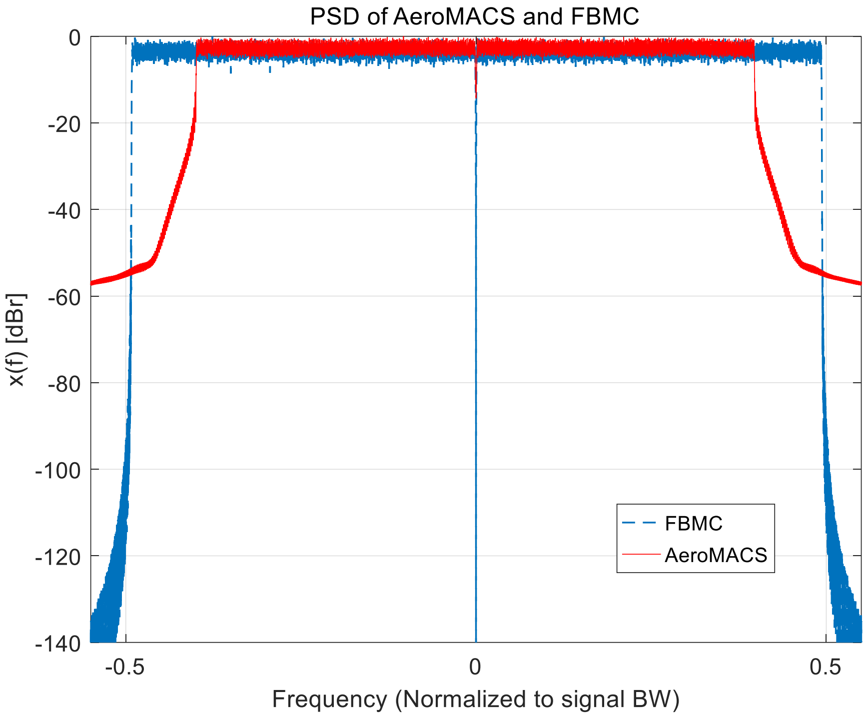

Figure 6.5. Power spectral densities of FBMC and AeroMACS systems.

In Figure 6.6 we show example adjacent channel interference (ACI) simulation results for AeroMACS and FBMC. These are the results for a “center” channel’s BER performance when interfered by two adjacent channels with larger power. Modulation is QPSK. The abscissa is the power ratio of the adjacent channels to that of the center channel, and the ordinate is the BER performance. To focus only on ACI we used the AWGN channel with SNR=5 dB without any other interference or impairments (e.g., we assume perfect synchronization, no Doppler spread, full precision in filter coefficients, no nonlinear distortion, etc.). As can be seen, compared to AeroMACS channels, FBMC channels have *substantially* better BER performance at much higher relative adjacent channel powers.

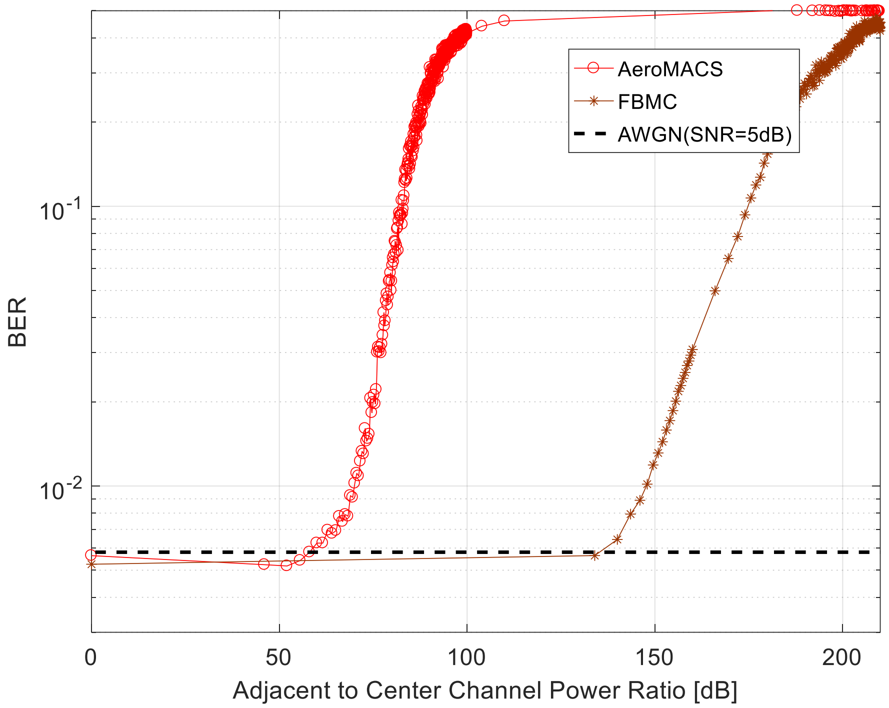

Figure 6.6. Adjacent channel interference results for QPSK modulation.

The (uncoded) BER vs. energy-per-bit to noise density for 16-QAM 5 MHz and 10 MHz bandwidth signals appears in Figure 6.7. For channel equalization first we simply used the zero-forcing technique assuming perfect channel knowledge at the receiver for both AeroMACS and FBMC, (Figure 6.7 results are in the absence of ACI and any other impairments). In Figure 6.7 we also plot the theoretical BER results for the AWGN and Rayleigh flat-fading channels for 16-QAM for comparison. In Figure 6.8 we show the BER results of the two systems using actual channel estimation techniques; Least-Square (LS) plus DFT-based channel estimation [64], [87]. We recall that in multicarrier communication systems as one of the popular channel estimation techniques we can use pilot scattering. In pilot scattering we choose some of the subcarrier symbols as pilots and then at the receiver we can estimate the channel impulse response based on these known pilots. LS channel estimation method is the simplest technique which finds the channel estimation $\widehat{H}$ in such a way to minimize the following cost function:

$$J(\widehat{H}) = \left\|Y - X\widehat{H}\right\|^2 \tag{6.1}$$

where Y is the received symbols on pilot subcarriers and X is the known transmitted pilot symbols. Therefore following the solution in [87] we can find the LS channel estimation as,

$$\widehat{H}_{LS} = X^{-1}Y \tag{6.2}$$

The DFT-based channel estimation technique has been derived to improve the performance of LS channel estimation by eliminating the effect of noise outside the maximum channel delay [87]. These results show that FBMC performance starts to degrade at higher signal-to-noise ratio (SNR) values (around 20 dB). This degradation appears at error probabilities below 10^{-2}, where forward error correction would be very effective in reducing the final output data error probability. The reason for the FBMC degradation is because we have no CP in the FBMC design, therefore the channel dispersion is large enough to make single-tap equalization inadequate for higher SNRs. Yet these results show that even using simple channel estimation techniques the FBMC system has BER performance very close to that of AeroMACS in the NLOS ASA channel for practical SNR values. This holds for other modulation orders as well (QPSK, 64-QAM). In these large airport channel conditions, even for the larger signal bandwidth, FBMC does not require a CP to deal with channel dispersion. Figure 6.7 results also show that the BER performance for the 10 MHz channel is worse than 5 MHz channel bandwidth (for example it is approximately 5 dB worse than the results for the 5 MHz bandwidth at SNR=20 dB). This is because for 10 MHz channel bandwidth signal, the multipath component taps in channel model have slightly worse fading and they are more correlated, therefore the channel is more dispersive than 5 MHz bandwidth.

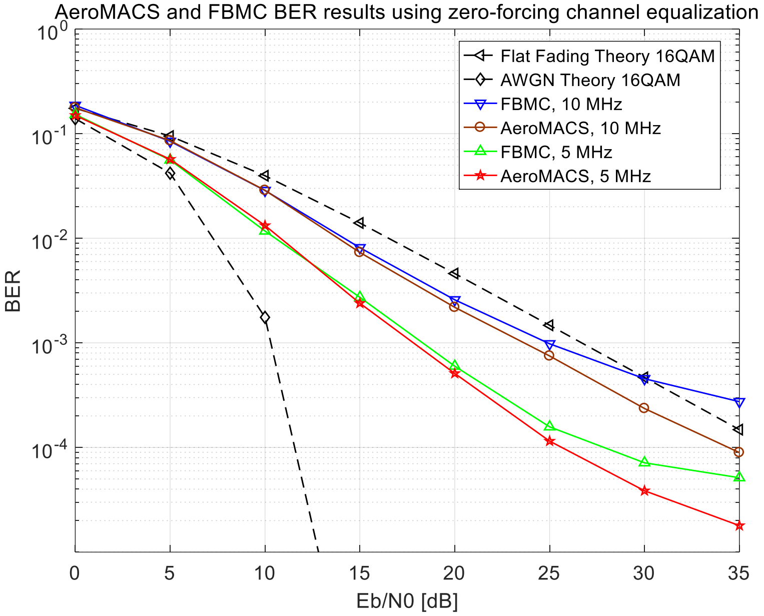

Figure 6.7. BER vs. E_b/N_0, 5 and 10 MHz bandwidth for 16-QAM, NLOS MIA airport channel with perfect channel knowledge (zero-forcing estimator).

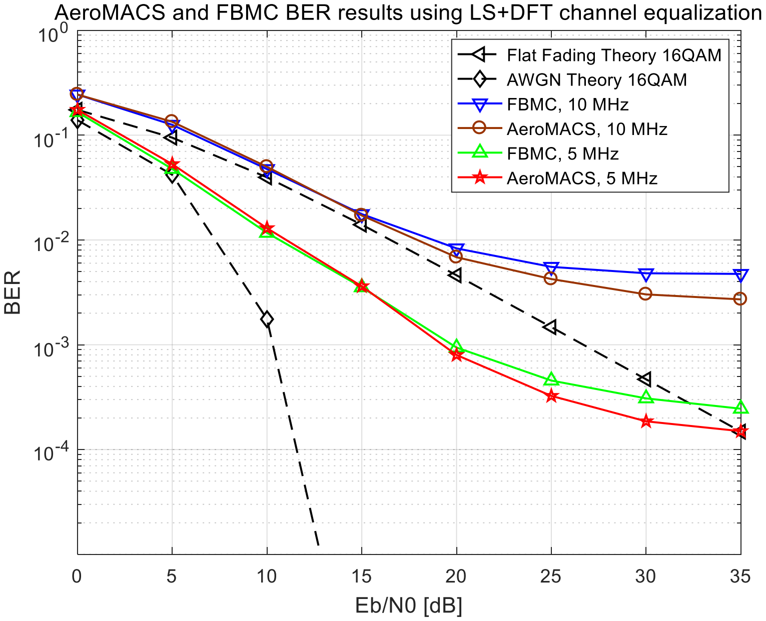

Figure 6.8. BER vs. E_b/N_0, 5 and 10 MHz bandwidth for 16-QAM, NLOS MIA airport channel with LS + DFT based channel estimation technique.

As noted, the compact spectrum of FBMC can be used to reduce the number of null subcarriers to well below the 100 subcarriers used by AeroMACS. In that case, the number of data subcarriers can be increased by 96 via FBMC, and comparing to the AeroMACS total of 393 data subcarriers, this increases the overall throughput by more than 23 percent. For example, in the 5 MHz channel, with QPSK, AeroMACS throughput is 7.65 Mbps, and FBMC throughput is 9.44 Mbps. These values increase to 22.95 Mbps for AeroMACS using 64 QAM, and 28.34 Mbps for FBMC using 64 QAM. All data rates approximately double for the 10 MHz channel bandwidths.

To summarize, in this chapter we explained the work done in [65], where we studied the potential of an FBMC based communication system as a future alternative to AeroMACS for airport surface environments. We compared AeroMACS to an FBMC system with similar parameters; each system meets the required spectral mask. In our simulations we used channel models based on real measurement data for the worst-case conditions (non-line-of-sight, large airport) and two values of channel bandwidth. The results show that FBMC systems have close BER performance to that of AeroMACS with a *smaller* number of guard subcarriers, and this will increase the FBMC system throughput by approximately 23 percent. The FBMC system's well-localized prototype filters decrease the out-of-band power emissions and hence interference to adjacent channels. This yields both higher spectral efficiency *and* lower BER when FBMC is used in a "fully loaded" spectrum. Due to these advantages, FBMC could be a very good candidate for an enhanced future airport surface area communication system.

CHAPTER 7

SPECTRALLY SHAPED FBMC COMMUNICATION SYSTEMS

In [62] we investigated a new spectrally shaped FBMC based communication system for AG communication. In our previous FBMC communication system design (similar to L-DACS1, and to essentially all OFDM systems), the transmitting power is equally distributed among all subcarriers. Based on the observation that channel conditions may differ for different subcarriers, we investigated the idea and potential of an unequal power distribution among subcarriers, where the distribution depends upon the channel. In our L-band AG case, we observe the high power DME signal spectrum on some of the edge FBMC subcarriers, and expect that these particular subcarriers will incur a larger BER than subcarriers with much weaker DME interference levels. In fact, some of these subcarriers may experience a BER floor. We validated this observation in simulations.

In what we term spectrally-shaped FBMC (SS-FBMC) we deviate from the equal power per subcarrier convention and we explore this as another means to mitigate DME interference. We propose a method to find the required guard subcarriers and optimize the amount of allocated power for each remaining subcarrier in order to obtain the best BER performance, without any error floor, for different QAM modulation orders and channels. In so doing we increase the communication system's efficiency and performance, at a very minor increase in complexity.

In one of our latest work we have used the SS-FBMC idea in [62] as a reliable approach for L-band AG *cognitive radio* based communication systems. Cognitive radio has been investigated in the last few years [97-100]. Most of the studies have been done for terrestrial and wireless regional area networks (WRAN). The most prominent cognitive radio standard is the IEEE 802.22, which is defined for UHF/VHF TV bands between 54 and 862 MHz [97]. In [62] and our new work described in this chapter we reviewed the potentials of using cognitive radio technology for aeronautical communication systems by using SS-FBMC approach. Here we study a cognitive SS-FBMC system as an inlay approach between DME channels in the L-band. We show that using this idea along with reliable spectrum sensing techniques, with DME systems considered the primary spectrum users, we can use the spectral gaps in the L-band spectrum for secondary users of a cognitive aeronautical broadband communication network. In the following sections first we cover the SS-FBCM contents and results in [62] and then we describe the new cognitive SS-FBMC system.

7.1 SS-FBMC

As noted, the essential difference between conventional FBMC and SS-FBMC transceivers is the use of scale factors or weights [A_0, A_1, …, A_{N-1}] in the SS-FBMC communication system structure (Figure 3.18). These factors assign the allocated power on each of the N subcarriers. In Table 7.1 we review and list the physical layer parameters of the FBMC and SS-FBMC system proposed in [62]. We see that the number of guard subcarriers in SS-FBMC is flexible and could change according to the link and signal modulation conditions. Subsequently we show that in cognitive SS-FBMC we have even more flexibility than in a "static" SS-FBMC system. Note that for SS-FBMC we may have different values of occupied bandwidth for different modulation orders and channels, and the minimum and maximum bandwidth we use in the L-band DME inlay case are ~459 kHz and ~576 kHz, respectively.

Table 7.1. FBMC and SS-FBMC physical layer parameters for L-band.

	FBMC	SS-FBMC
Total FFT bandwidth (kHz)	625	625
Occupied Bandwidth, $\boldsymbol{B}$ (kHz)	595.6	varies
FFT length ($\boldsymbol{N_{FFT}}$)	64	64
# of used subcarriers ($\boldsymbol{N_u} = \boldsymbol{N_{FFT}}$-$\boldsymbol{N_g}$-1)	61	46, 52, 54, 58
# of guard subcarriers ($\boldsymbol{N_g}$)	2	5, 9, 11, 17
Subcarrier spacing, $\boldsymbol{\Delta f} = \boldsymbol{B/(N_u}+1)$ (kHz)	9.765	9.765
Total Symbol duration before overlapping $\boldsymbol{T_s}$ (μs)	409.6	409.6
Symbol duration after overlapping $\boldsymbol{T}$ (μs)	102.4	102.4

The idea of power spectral shaping in FBMC spectrum comes from the special shape of the PSD of the DME signal. Figure 7.1 depicts the PSD of the FBMC signal (and L-DACS1 signal *without windowing* for comparison) in between two adjacent DME channels. As we see, most of the energy of the FBMC system is concentrated in between two DME channels. DME interference power values get larger as we approach the FBMC spectrum sides.

In our SS algorithm in SS-FBMC we used Shannon's channel capacity theorem [101]. Derived from Shannon's theorem, in order to maximize the capacity of the channel at each subcarrier, assuming we know the relative DME interference and AWGN power at each subcarrier, the well-known water filling algorithm pertains [88]. This gives us a metric to find the desired powers for each subcarrier. Our goal here though is not to maximize the capacity of each subcarrier, but rather to adjust power levels to "equalize

BER performance" across subcarriers to an acceptable level. In this section we find the optimum solution for different QAM modulation orders and FL and RL conditions in order to find the best BER performance over all subcarriers.

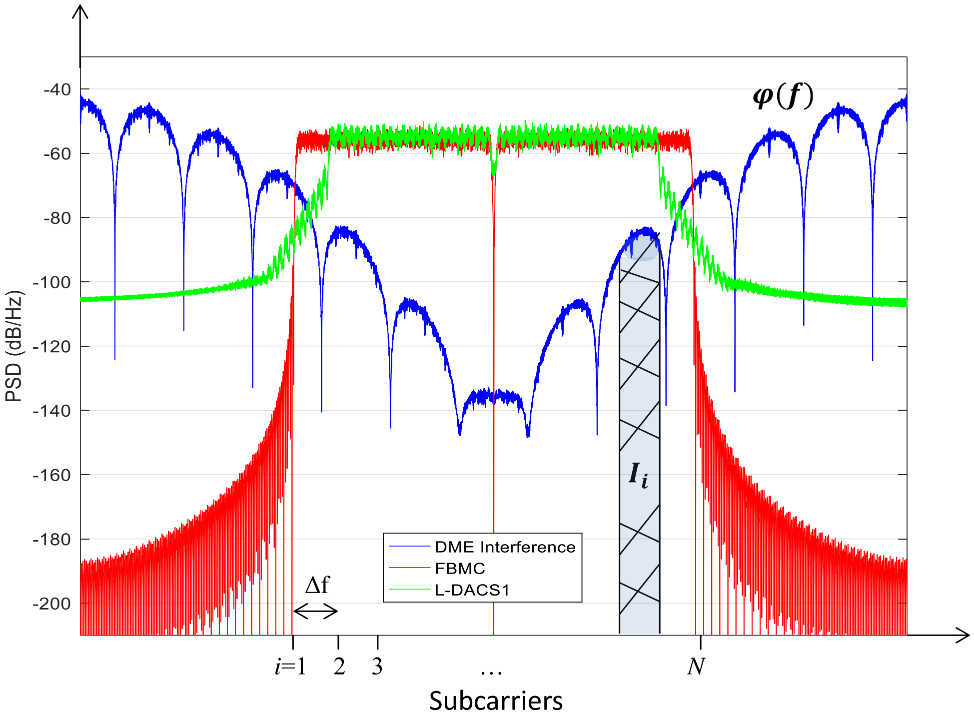

Figure 7.1. FBMC (and L-DACS1) spectrum in between two DME channels.

In our simulations, we noticed that without using guard band subcarriers on each side of the FBMC spectrum, the output BER could exhibit a large error-floor, especially for the higher QAM modulation orders. In order to solve this problem we define an optimization problem which has a two-step solution. As a first step we used the water filling algorithm to find the guard bands required for each modulation order according to the ratio of the energy per bit and DME interference and AWGN power at each subcarrier. This means the guard subcarriers are the ones that incur a very large amount of interference and no attempt is made to use them for data transmission. After finding the guard band subcarriers, then our second step is to apply what we call *inverse water* *filling* to equalize the bit energy to interference and noise density ratio at all remaining subcarriers.

In order to better understand this problem, we explain the process based on Figure 7.1. This figure shows the possible location of all N subcarriers of the multicarrier communication system, for an arbitrary example subcarrier bandwidth. The gray color filled area indicates the amount of DME channel interference (I_i) in the band of subcarrier i. In this Figure at subcarrier i, and based on Shannon's capacity theorem[3] for the AWGN channel, the capacity of each subcarrier can be calculated as follows,

$$C_i = \Delta f log_2\left(1 + \frac{g_b^i}{\sigma_i^2}\right) \; i = 1, \dots, N \tag{7.1}$$

where Δf is the subcarrier bandwidth, and g_b^i is the allocated energy per bit at subcarrier i and $\sigma_i^2 = \sigma_{AWGN}^2 + I_i$ is the AWGN power plus DME interference (I_i) at subcarrier i. In order to calculate I_i over each subcarrier we need to know the PSD of the DME signal. According to spectrum equation of the DME signal (3.13), for each DME power and ppps (and channel direction, i.e., FL and RL) we can calculate the following interference power over each subcarrier,

$$I_i = \int_{f_i-\Delta f/2}^{f_i+\Delta f/2} |\varphi(f)|^2 \, df \;\; i = 1, \dots, N \tag{7.2}$$

where according to Figure 7.1, $\varphi(f)$ is the spectrum of the DME signal relative to that of the FBMC signal at each frequency, and f_i is the center frequency of subcarrier i. Note that in both DME and SS-FBMC simulations in this work we do not explicitly express terms in a link budget but simply scale for relative power levels at the receivers. Solving this equation for all subcarriers for both links we find the DME interference energies at

---

[3] We note that Shannon's capacity formula pertains to white noise channels, and our interference densities are non-white. For decreasing subcarrier bandwidth, on a per-subcarrier basis the interference density approaches a white form.

each subcarrier; for one example these values at each subcarrier are simulated and plotted in Figure 7.2. In this plot according to the DME specs we assumed DME peak powers equal 1000 W and 300 W for FL and RL, respectively. As seen in this figure, and as expected, the amount of interference is much higher for side subcarriers and is minimum at the center. Note that as long as FL DME signal power is $\frac{1000}{300}$ larger than RL therefore its DME interference energy at each subcarrier is also $10\log\left(\frac{1000}{300}\right) \cong 5dB$ larger as shown in Figure 7.2.

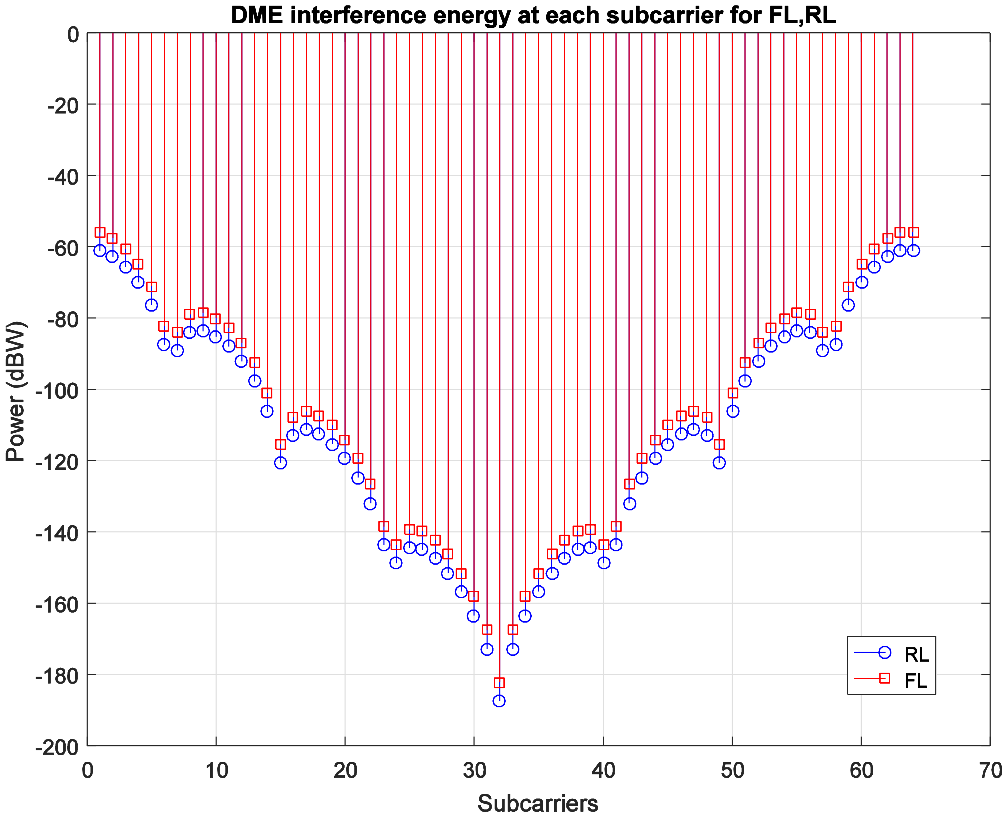

Figure 7.2. DME interference energy at different subcarriers in FL and RL.

For the first step in our algorithm for finding the guard subcarriers (and when finished, the subcarriers that we use to transmit symbols for each M-QAM constellation) with minimum degradation from interfering signals, we define the following optimization problem,

$$\underset{\alpha_i,\ g_b^i}{\boldsymbol{Max}} : \sum_{i=1}^{N} \alpha_i C_i$$

$$subject\ to:$$

$$1: g_b^i \geq 0 \quad 2: \alpha_i \in \{0,1\} \ \ \forall\, i \quad 3: M \sum_{i=1}^{N} g_b^i = P \tag{7.3}$$

This optimization problem has three constraints; the first constraint states that the power allocated to each subcarrier is a non-negative value. The second constraint defines the parameter α_i for the subcarrier selection process: the α's take value either 0 or 1. The last constraint limits the total transmitting power to a certain power value P (which in our simulations we use $P = 10\ W$ based on L-DACS1 requirements). This optimization problem has a well-known solution based on the water filling algorithm [88], so after applying the water filling algorithm we find the guard subcarriers: those are subcarriers that experience a very high amount of interference.

For the second step in our algorithm (to equalize the signal to interference plus noise ratio (SINR) among all subcarriers to obtain the lowest BER, without error-floor) we just accept the allocated subcarriers (α_n) without considering the allocated powers (g_b^n). This means subcarriers with $\alpha_n = 1$ are active subcarriers and the others are guard bands. The reason we do not accept the initial g_b^n values is that, based on the water filling algorithm, these allocated powers have lower power values for subcarriers with higher DME interference, and they will result in high BER-floors. In order to solve this problem and to remove the BER-floors, we deviated from (7.3) and just accept the α_i values as assigned subcarriers, then in order to equalize the SINR values for all active subcarriers we allocate the power between active subcarriers as follows,

$$P_{b_{new}}^{i} = \frac{2}{N}\sum_{j=1}^{N} g_b^j - g_b^i \quad \forall\, i|\, \alpha_i \neq 0 \tag{7.4}$$

By this approach we allocate more power to the remaining or active subcarriers that experience larger DME interference.

7.2 SS-FBMC SIMULATION RESULTS

This section contains different SS-FBMC simulation results for both the AG FL and RL for QPSK, 16-QAM and 64-QAM modulations. We used the physical layer parameters listed in Table 7.1. Using the proposed spectrally shaped algorithm we find the guard subcarriers and allocated power values for active subcarriers in both FL and RL. Figure 7.3 shows one example solution of the power mask (linear scale, allocated power to active subcarriers) of the FL subcarriers for different QAM modulation orders.

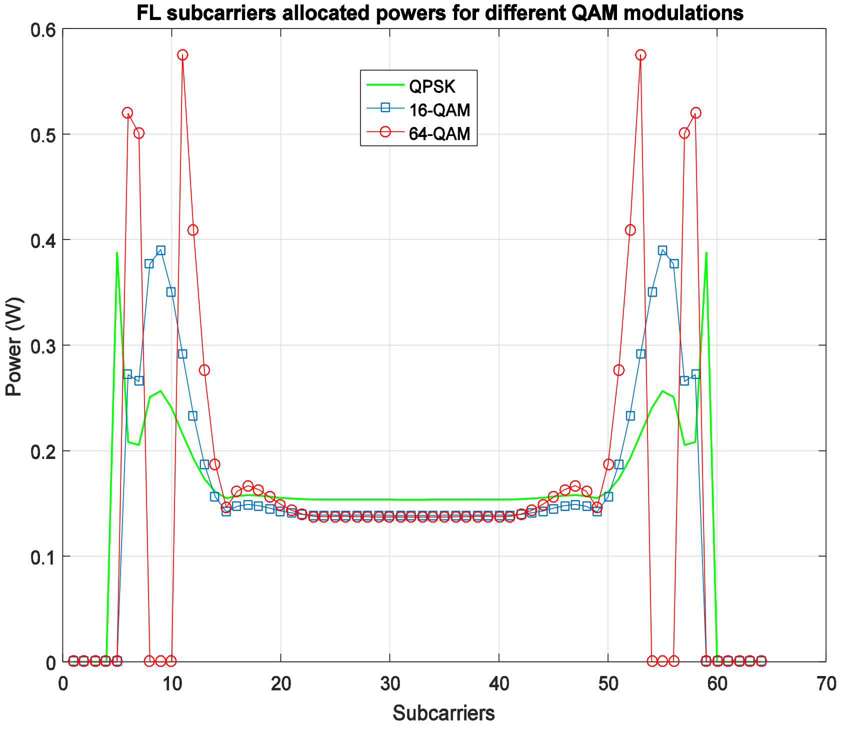

Figure 7.3. FL subcarriers power mask for different QAM modulations.

Based on our power constraint, the sum of all subcarrier powers is equal to 10 W. As we see QPSK has 2 fewer guard subcarriers than 16-QAM and 64-QAM. It also has lower power levels on its side subcarriers because of its greater Euclidean distance between signal points for a given E_b/N_0. As we see for higher order modulations the SS algorithm solution is more conservative, therefore in addition to more guard subcarriers, the allocated powers to the side subcarriers must be higher than in QPSK in order to increase the energy per bit to noise density ratio. In Figure 7.4 we plot the PSD (logarithmic scale) of SS-FBMC waveforms for the different modulation orders with the linear power mask shown in Figure 7.3.

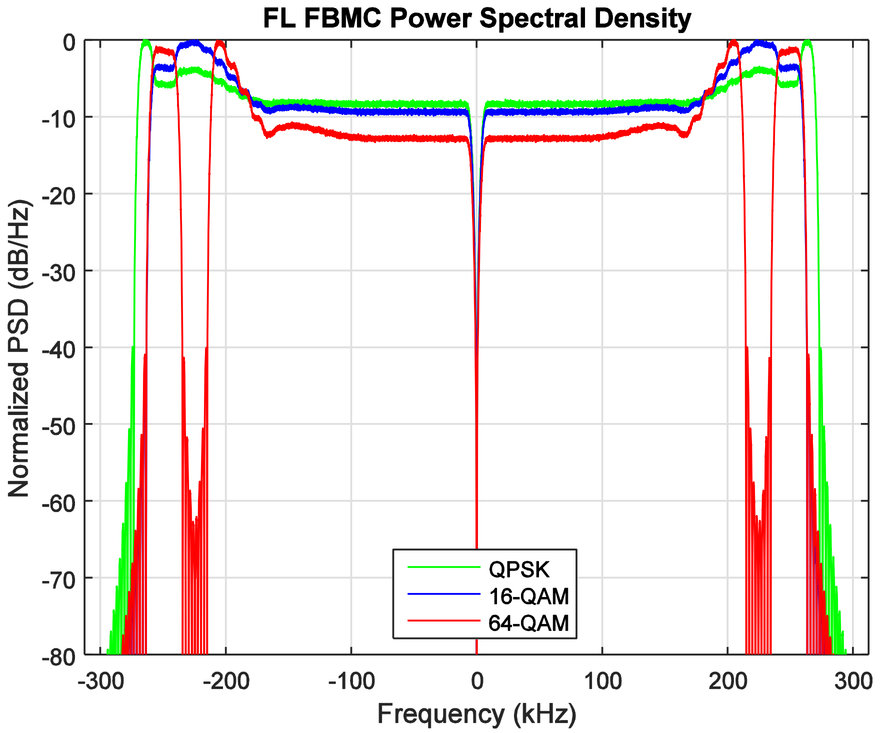

Figure 7.4. FL PSDs for different QAM modulations.

The QPSK spectrum has slightly larger bandwidth and the difference between its peak power and the flat area of the PSD is smaller than in the other two QAM modulation orders. The 64 QAM PSD is interesting in that it is atypical for FBMC, with nulls and sidelobes. In Figures 7.5 and 7.6 similar results are plotted for the RL. Here the number of guard bands is smaller because in the RL the DME power is lower than in the FL.

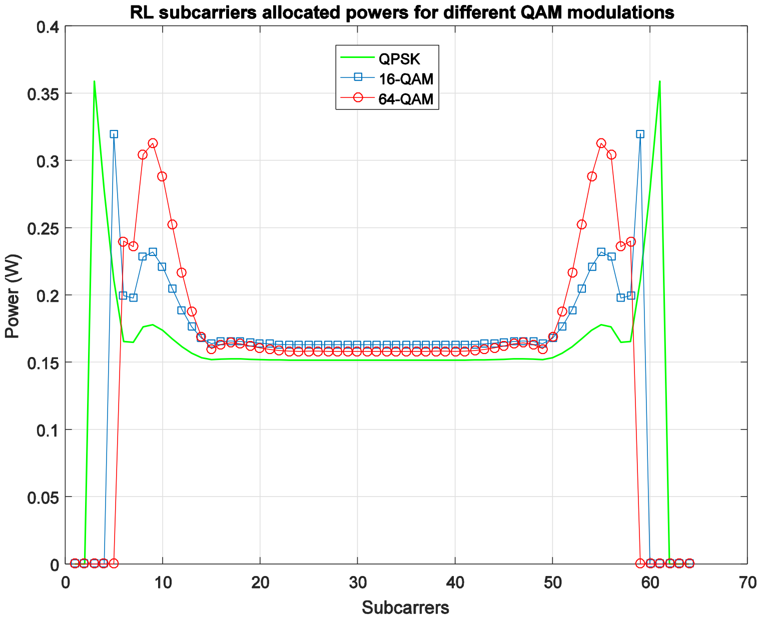

Figure 7.5. RL subcarriers power mask for different QAM modulations.

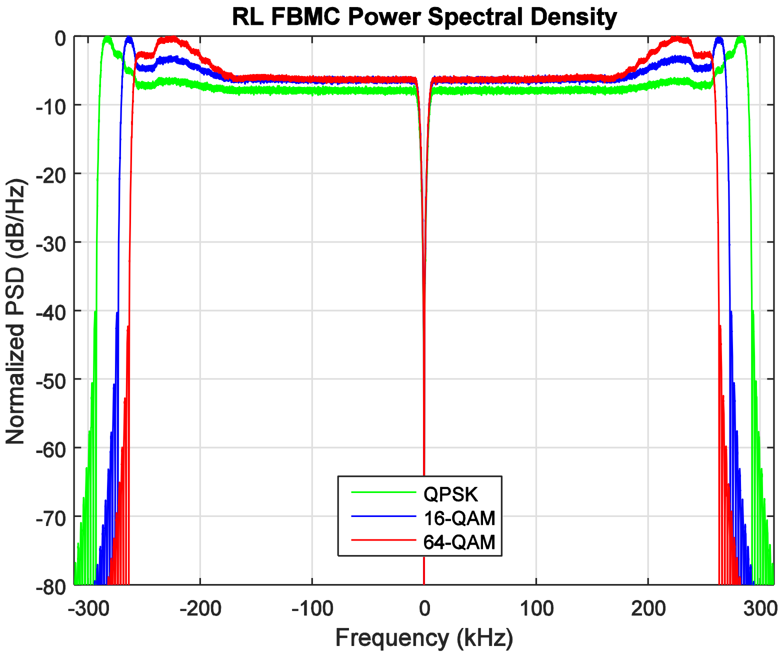

Figure 7.6. RL PSDs for different QAM modulations.

In the following Figures in this section (Figures 7.7 to 7.12) we plot simulated BER results for both FL and RL and different QAM modulation orders. In these figures the colored curves depict the BER performance of each individual subcarrier. The black solid and dashed curves are BER results for AWGN theoretical and the average BER across all subcarriers, respectively. We have plotted the BER result for each subcarrier to show the variation of the BER across subcarriers as a result of the spectral shaping technique.

As seen in these figures, the colored BER curves that are to the left of the dashed average BER line are the BER results for the subcarriers with higher allocated powers. Most of the BER results for the "central" subcarriers are crowded near the average BER dashed line, some to the left, and some to the right. In all of these results we do not see any error floors, even at high SNR values. We emphasize again that all these colored curves are shown simply to illustrate the BER *variation* that results from our spectral shaping technique.

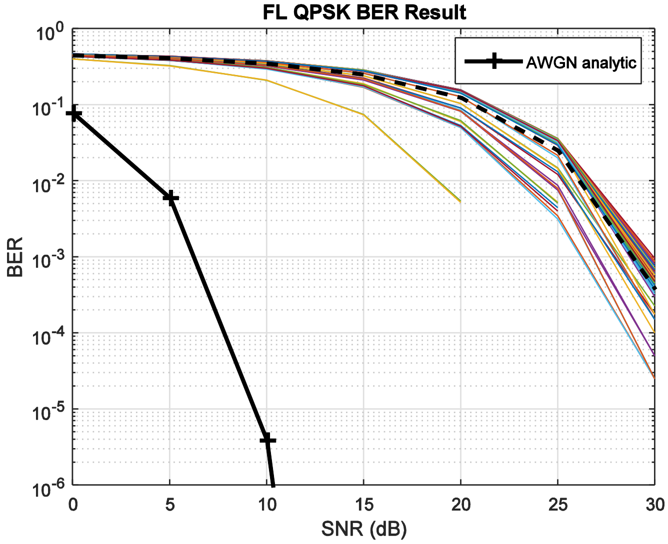

Figure 7.7. FL QPSK BER results, colored curves are the BERs of each subcarrier and the dashed curved is the averaged BER of all subcarriers.

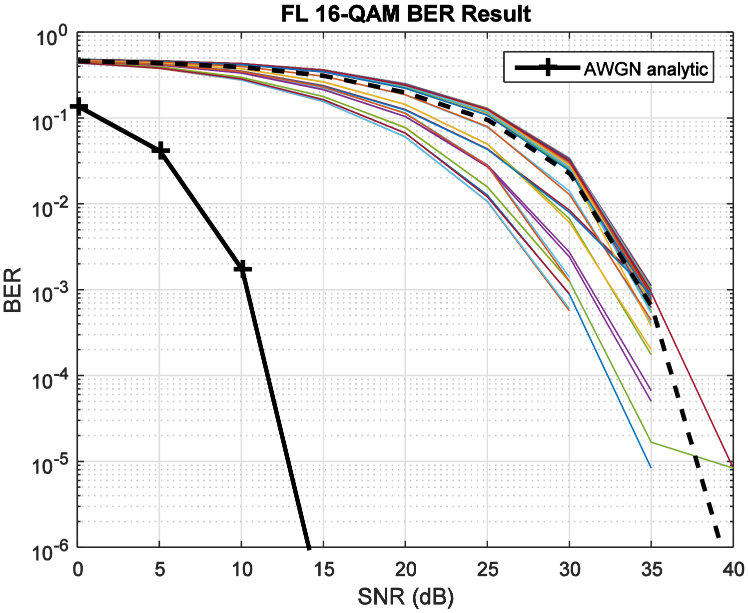

Figure 7.8. FL 16-QAM BER results, colored curves are the BERs of each subcarrier and the dashed curved is the averaged BER of all subcarriers.

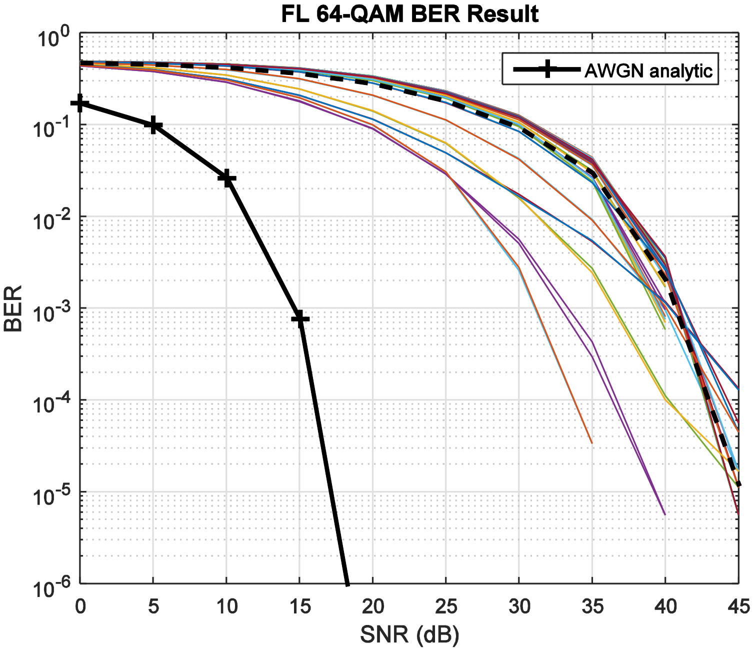

Figure 7.9. FL 64-QAM BER results, colored curves are the BERs of each subcarrier and the dashed curved is the averaged BER of all subcarriers.

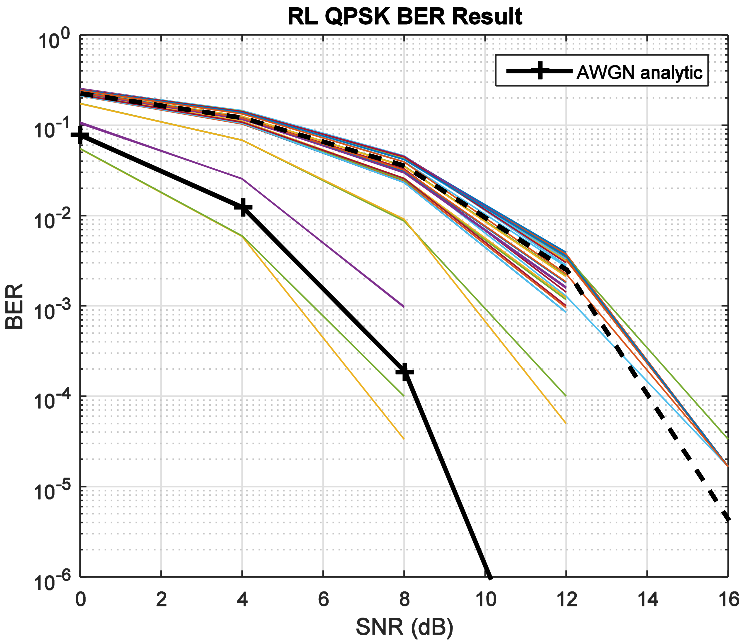

Figure 7.10. RL QPSK BER results, colored curves are the BERs of each subcarrier and the dashed curved is the averaged BER of all subcarriers.

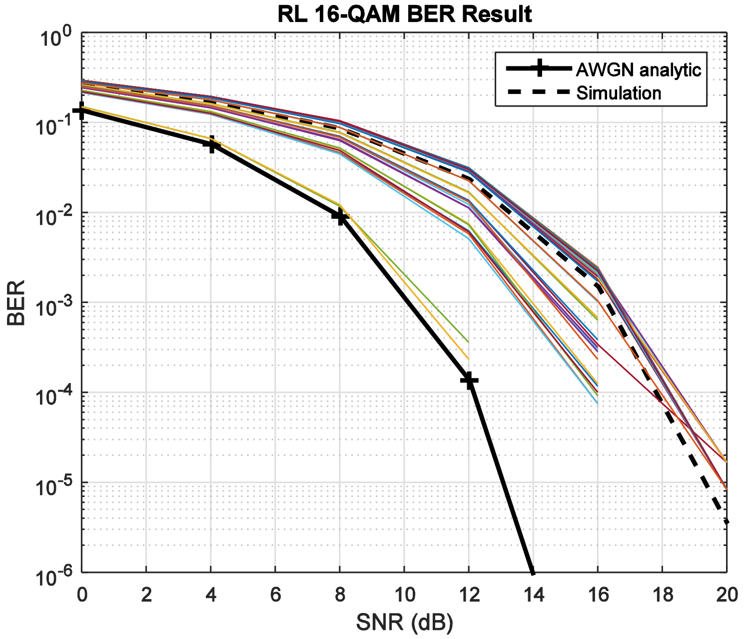

Figure 7.11. RL 16-QAM BER results, colored curves are the BERs of each subcarrier and the dashed curved is the averaged BER of all subcarriers.

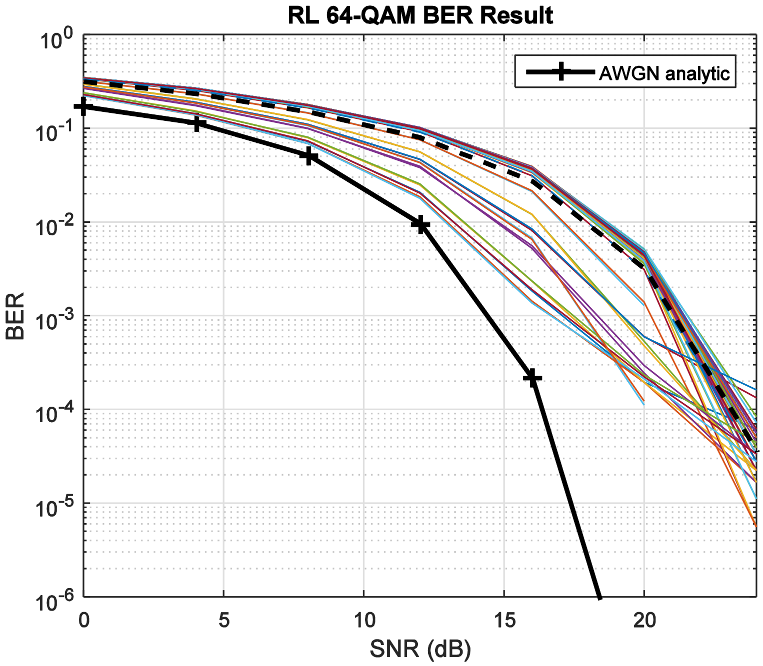

Figure 7.12. RL 64-QAM BER results, colored curves are the BERs of each subcarrier and the dashed curved is the averaged BER of all subcarriers.

Generally it is the average BER (dashed curve) that matters most, although in some applications, some data can be made more reliable via careful allocation to subcarriers. To validate these results we changed the power allocation mask values very slightly and noticed that for different guard subcarrier locations, some of these subcarriers had an error floor which would also yield an error floor in the overall average BER.

As an example of a system performance differences between a conventional FBMC system [4] and SS-FBMC, we simulated the same FL link for 16-QAM and depict the result in Figure 7.13. Here the average BER reaches an error floor due to the poor performance of the subcarriers nearest the two sides of the spectrum. The SS-FBMC result for this case as shown in Figure 7.8 significantly improves the BER results and eliminates the error floors.

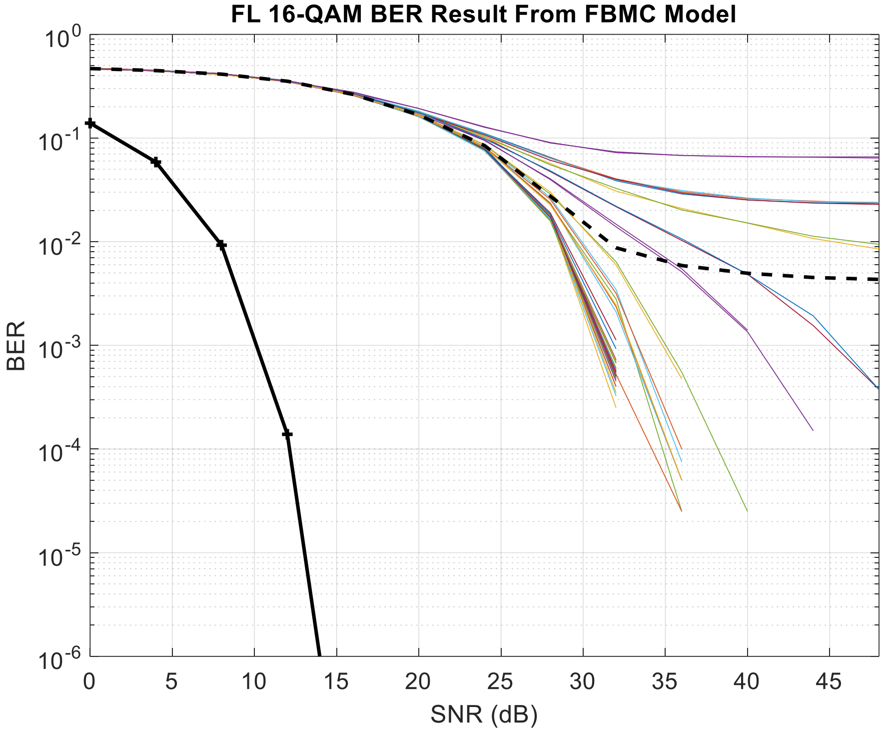

Figure 7.13. FL 16-QAM BER results from FBMC, colored curves are the BERs of each subcarrier and the dashed curved is the averaged BER of all subcarriers.

According to these results, in comparison to conventional FBMC [4], our example L-band AG SS-FBMC system has a larger number of data subcarriers (2 more) and hence larger throughput (~3%) in RL QPSK, but it has more guard subcarriers (2) and slightly smaller throughput (~3%) compared to the original FBMC scheme for FL QPSK. We emphasize again that the primary virtue of the SS-FBMC design is that there is no BER floor at high SNR values.

7.3 COGNITIVE SS-FBMC

In this section we describe the cognitive radio (CR) approach for our SS-FBMC system. Within recent years, some standardization activities, such as IEEE 802.22, have contributed to achieve communication systems based on CR for WRAN and terrestrial networks [89], [97]. For VHF bands the studies of CR in aeronautical systems has been done in [90]. Later in [91], the authors expanded this idea with more sophisticated algorithms and additional results for the same band. Here we explore the idea of CR in L-band for A/G communications purposes. In Table 7.2, we review the SS-FBMC scheme and list the physical layer parameters for our cognitive SS-FBMC system. The cognitive SS-FBMC system has even more flexibility in parameter selection than SS-FBMC.

One of the main differences between the cognitive SS-FBMC scheme and SS-FBMC is the total bandwidth. We chose the total bandwidth as 1 MHz in our cognitive system in order to send signals even with*in* the DME bands when DME channels (called primary users in CR systems) are not activated. This larger bandwidth enables use of shorter packet lengths, especially for smaller numbers of subcarriers. We also let the total number of subcarriers take smaller values: this value can be selected based on the channel conditions in different aeronautical communication environments.

Table 7.2. SS-FBMC and cognitive SS-FBMC physical layer parameters.

	SS-FBMC	Cognitive SS-FBMC
Total FFT bandwidth or sample rate (kHz)	625	1000
Occupied Bandwidth, B (kHz)	varies	varies
FFT length (N_{FFT})	64	16, 32, 64, 128
# of used subcarriers ($N_u = N_{FFT}-N_g-1$)	46, 52, 54, 58	varies (cognitive)
# of guard subcarriers (N_g)	5, 9, 11, 17	varies (cognitive)
Subcarrier spacing, $\Delta f = B/(N_u+1)$ (kHz)	9.765	7.8125,15.625, 31.25, 62.5
Total Symbol duration before overlapping T_s (μs)	409.6	64, 128, 256, 512
Symbol duration after overlapping T (μs)	102.4	16, 32, 64, 128

In order to test our cognitive SS-FBMC algorithm and for further analysis we also suggested another example interfering signal: rectangular pulses. The time domain and frequency domain equations for the pulse and its spectrum are given in (7.5) and (7.6), with $T = 2 \times 10^{-6}\ \mu s$ in our simulations.

$$S_{rect}(t) = \Pi(t) = \begin{cases} 1 & t \leq T \\ 0 & t > T \end{cases} \tag{7.5}$$

$$S_{rect}(f) = T\, sinc(Tf) \tag{7.6}$$

In Figure 7.14 we show the PSD analytical and simulation results for two similar and adjacent channels of DME and rectangular pulse signals. For this example we have plotted results for a 1 MHz bandwidth. In these results we assumed transmitting signal pulses with peak power equal to 300 W and pulse rate 150 ppps. The SS algorithm and its solution in cognitive SS-FBMC is the same as SS-FBMC except the physical layer specifications can change according to channel conditions; in cognitive SS-FBMC we have more flexibility on bandwidth, subcarrier bandwidth, number of subcarriers and accordingly the length of the signal packets in the time domain (Table 7.2).

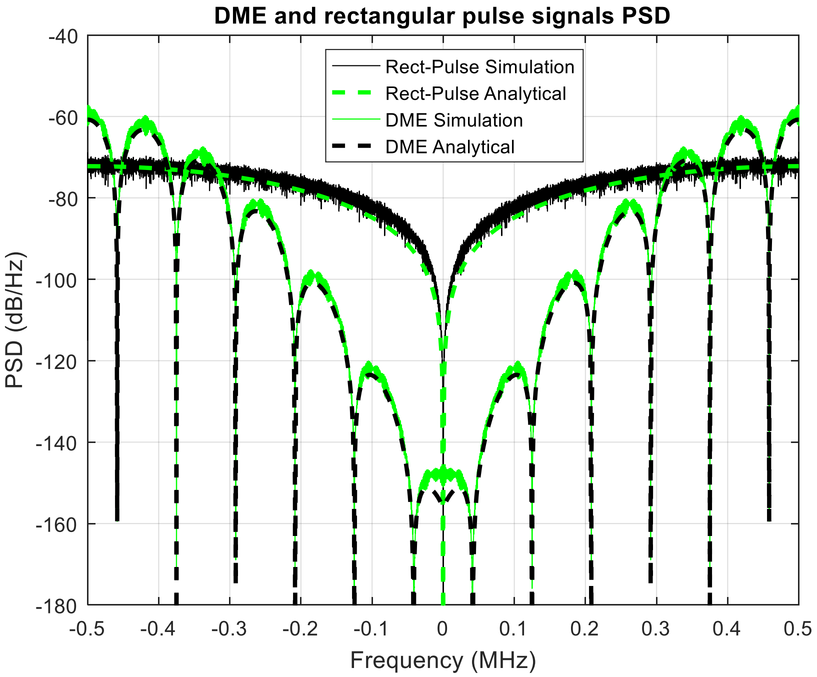

Figure 7.14. DME and rectangular pulse power spectral densities.

As mentioned, the total bandwidth of our cognitive SS-FBMC system is 1 MHz, therefore in our subcarrier metrics analysis in (7.1) and (7.2) we follow the design depicted in Figure 7.15 instead of Figure 7.1. As shown in this figure, total bandwidths between adjacent DME channels would be considered as the cognitive SS-FBMC signal bandwidth, and this consideration will also let us to use entire DME channels when they are inactive. In this model, after calculating subcarrier metrics in (7.1) and (7.2) we can follow the two step solutions for the SS algorithm (equations (7.3) and (7.4)) to find the guard subcarriers and allocated power on remaining active subcarriers.

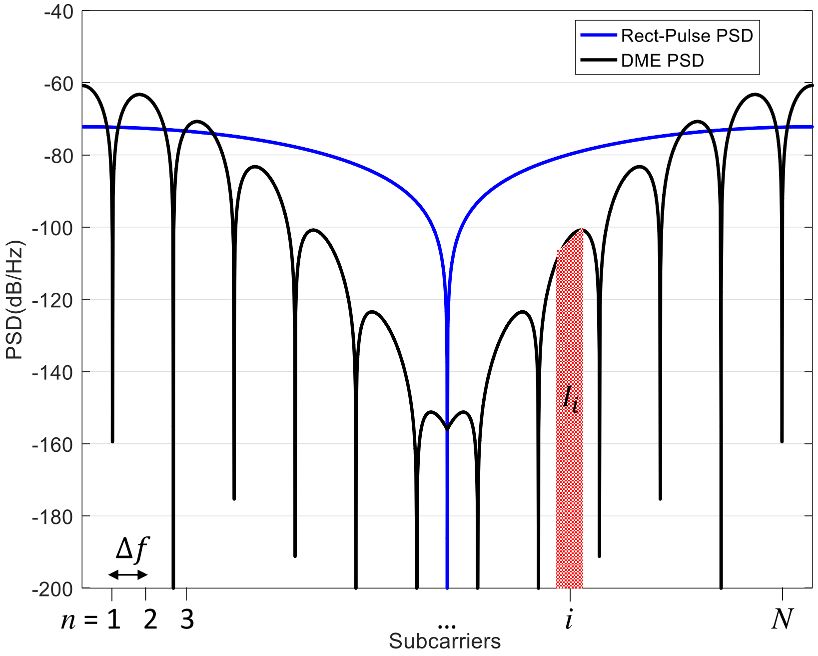

Figure 7.15. Subcarriers positions in cognitive SS-FBMC model.

7.4 SIMULATION RESULTS

In Figures 7.16 and 7.17 the PSDs of our cognitive SS-FBMC waveform after solving the SS algorithm for the DME and rectangular pulse interference scenarios are shown. As shown in these figures, the SS algorithm allocated more powers to the subcarriers that experience higher DME interference levels, and when the DME interference is higher than a threshold (threshold in water-filling algorithm), the SS algorithm will consider that subcarrier as guard subcarrier.

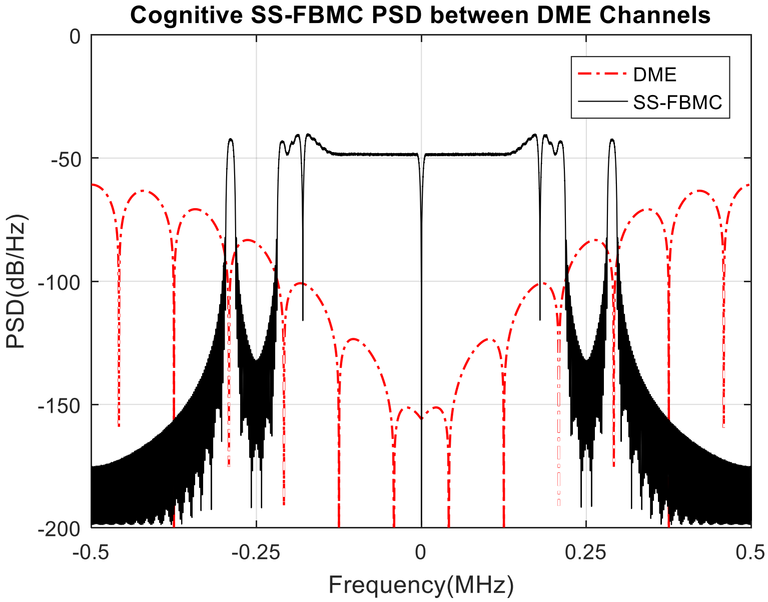

Figure 7.16. Cognitive SS-FBMC PSD over DME channel.

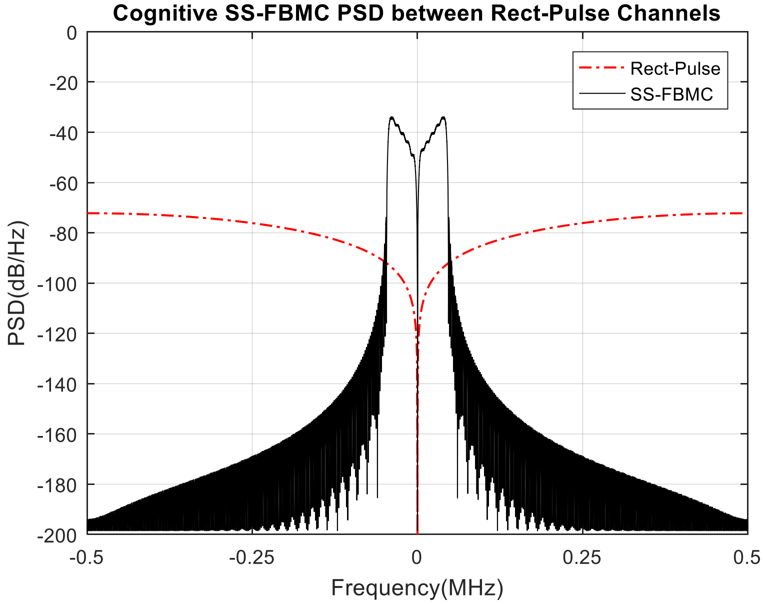

Figure 7.17. Cognitive SS-FBMC PSD over rectangular pulse channel.

In these simulations we used the parameters listed in Table 7.2 for cognitive SS-FBMC, and also chose $P = 10\ W, N = 128$. We used the same prototype filter as in our AG FBMC system. For the AG channel model we considered the over-water environment channel, and we assumed perfect channel knowledge at the receiver for channel equalization. Actually this is unrealistic to assume perfect channel knowledge and in order to implement the system similar to other multicarrier communication systems we need to have pilot-based channel equalization in our cognitive SS-FBMC system. But in this work our main purpose is to investigate the potential of our cognitive SS algorithm, and this is done in perfect channel scenario without other interference (except DME). In future work we plan to study the channel equalization technique for our SS system. Note that in these simulations, DME and rectangular pulse interference signals have the same peak powers of $300\ W$ and pulse rate $150\ ppps$ resembling the transmitted signals from aircraft. Also note that in these simulations we assumed similar DME and rectangular pulse signals on *both* sides of the SS-FBMC communication spectrum. Figure 7.18 shows the active subcarriers with their allocated powers for this particular example; note that the center subcarrier is nulled for all cases in order to have null DC subcarrier.

In this example for DME and rectangular pulse signals there are 54 and 10 active subcarriers, respectively. The reason DME channels allow us to have more active subcarriers is because of its PSD, which has smaller power levels around the spectrum gap. Another way to state this is that according to Figure 7.18, in the rectangular pulse interferer situation the allocated powers to the active subcarriers are larger than those for the subcarriers in the DME interferer situation because of the higher power levels of the rectangular pulse signal.

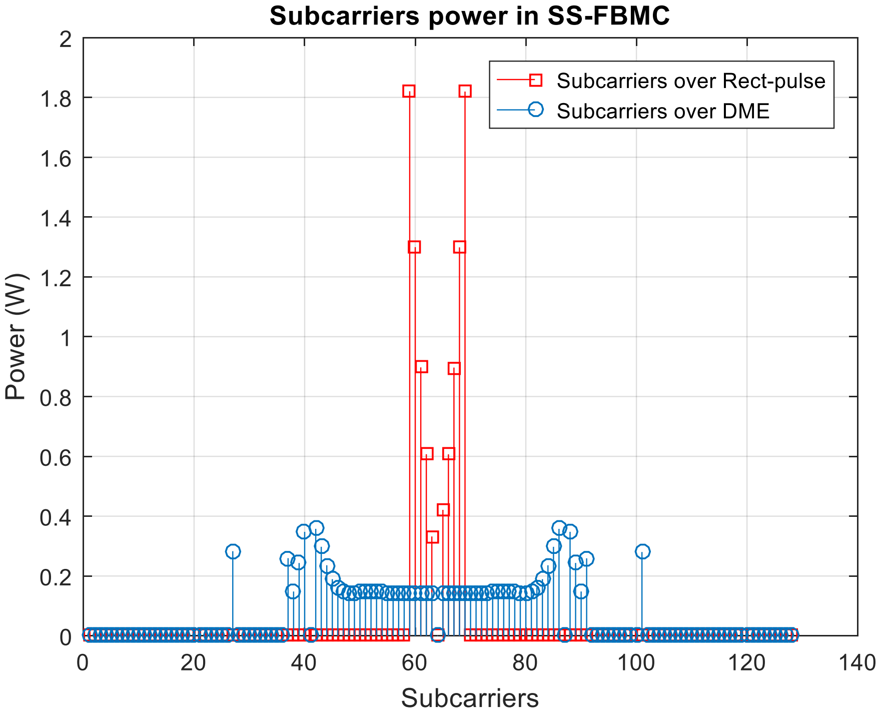

Figure 7.18. Guard subcarriers and allocated powers to active subcarriers from SS algorithm

It is clear that for other situations (different modulation orders and interference signals) we might have different algorithm solutions and the PSDs would change.

We estimated the BER by simulations for this example in Figure 7.19. These BER results are the best case scenario without any error-floors (since we have considered perfect synchronization, equalization, etc.). In order to test the accuracy of the results of our algorithm we changed some of the subcarriers in Figure 7.18 for the DME interference case. We manually activated subcarriers numbered 35 and 36 and 92 and 93 and we set their power levels equal to that of the nearest active subcarrier, specifically:

$$g_{b_{new}}^{35} = g_{b_{new}}^{36} = g_{b_{new}}^{37} \text{ and } g_{b_{new}}^{92} = g_{b_{new}}^{93} = g_{b_{new}}^{91} \tag{7.7}$$

Total transmit power is then normalized before BER estimation. We term this result the “non-optimized DME” case. As the results show, those manually activated subcarriers result in error floors that affect the overall BER performance of the system.

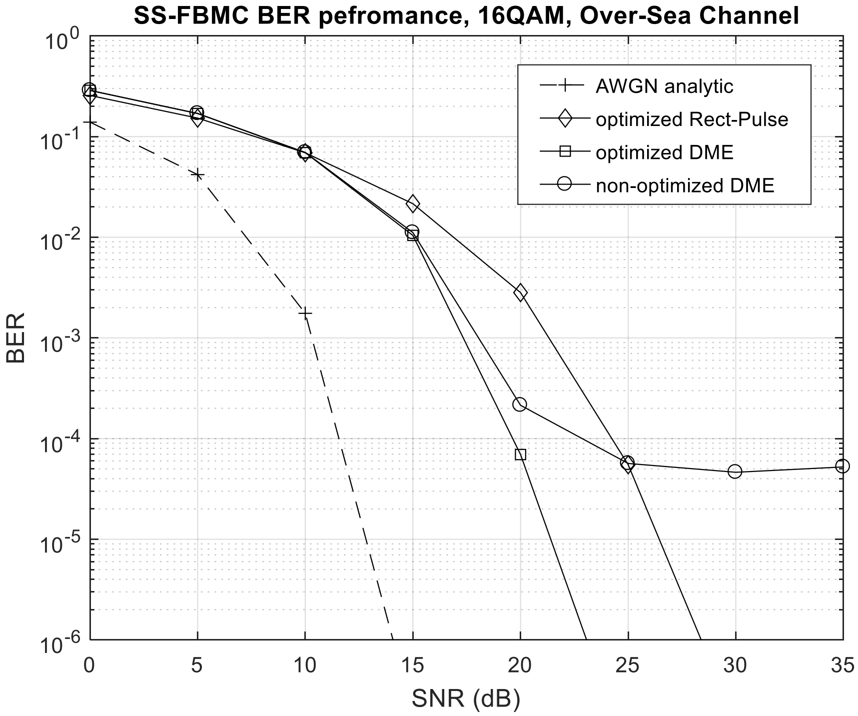

Figure 7.19. SS-FBMC BER results on DME and rectangular pulse channels

We should note that this SS approach only works well with FBMC due to its well localized prototype filters and sharp subcarrier PSD. Using this approach for CP-OFDM would still yield large BER floors because of its rectangular shape prototype filters with unfavorable PSD. These results show that cognitive SS-FBMC systems, with their flexible and adaptive spectrum shape, could be a good candidate for cognitive radio purposes in L-band AG communication systems.

CHAPTER 8

CONCLUSIONS AND FUTURE WORK

In this dissertation, we have investigated the potential of using new and more efficient multicarrier waveform designs based on FBMC for the L-band and C-band air-ground channel, and for airport surface environments. Our investigation employed analyses and simulations, and based upon empirical channel models for the various aviation communication environments, we provided comparative results for our proposed FBMC communication system and other CP-OFDM based systems such as L-DACS1 and AeroMACS. These results showed that our FBMC designs improve over the existing designs in terms of throughput and/or error probability performance. In this chapter, the main conclusions and discussion of avenues for future research for academia and industry are presented.

8.1 DISSERTATION CONCLUSIONS

The main objective of our research was to evaluate and compare the multicarrier air interfaces FBMC and CP-OFDM in the L-band and C-band for air-ground communications. We explored this because the aviation community is seeking new solutions for spectrum crowding, and better-performing new technologies are of interest. Some background on AG and airport surface communication systems and L-band and C-band spectrum issues and challenges were discussed. A survey of the literature regarding AG communication systems for VHF, L-band and C-band was provided. The AG and airport surface channel models based on recent NASA Glenn Research Center measurements were described and our simulations of them were validated against measurement results. We provided the technical specifications regarding the physical layer of CP-OFDM systems (L-DACS and AeroMACS) and based on these specifications we proposed our new designs based on FBMC for L-band and C-band. Via several power spectral density and error probability results we have shown that using FBMC yields significant advantages. These advantages are better spectral efficiency (throughput) and much lower out-of-band and in-band interference. For example FBMC is more robust than L-DACS1 to DME channel interference in the L-band and hence has lower BER. Similarly, for the airport surface environment FBMC has lower out-of-band power than AeroMACS and also attains a higher throughput. In general FBMC could increase the throughput by up to 23 percent. We have compared the BER performance results of FBMC, DACS and AeroMACS systems in different AG and airport surface environments and shown that even in the most highly dispersive AG channels FBMC has performance similar to that of the existing systems, with the advantage of higher throughput and lower adjacent channel interference.

We compared the performance of FBMC with L-DACS1 in a cellular network setting where the FBMC system operates in the presence of multiple DME stations. Our results show that when the ground sites for the FBMC, L-DACS1 and DME ground stations are co-located, FBMC can increase the range of communication by virtue of its reduction of the DME signal interference. We also produced initial results for dual antenna AG communication systems. We have shown that when strong two-ray channel conditions exist, if antenna separation can be dynamically adjusted with link distance, then even in these line of sight cases using multiple antennas can achieve spatial diversity gains.

We proposed spectrally shaped FBMC systems and for that devised a subcarrier/power allocation algorithm to obtain the best BER performance without any error-floors in non-white noise channels such as the L-band with DME signals. Our results showed the FBMC error-floor-free performance in different DME channel conditions (power, pulse rate). Based on this algorithm we also proposed a highly efficient cognitive spectrally shaped FBMC communication system with generally error-floor-free performance for L-band AG communication systems. Based on these results, as detailed in the dissertation, we suggest that FBMC is a strong and efficient waveform candidate for future AG and airport surface communications.

8.2 FUTURE WORK

Possible extensions of this dissertation work are listed below:

- Implementation of example FBMC communication systems on software defined radio (SDR) platforms, and testing to compare the performance with CP-OFDM systems in different AG channel bands and environments.
- Investigate and test the channel equalization, synchronization and also MIMO capability of FBMC through simulations, and eventually implementation in different AG channel bands and environments.
- Investigation and comparison of FBMC with CP-OFDM systems in more dispersive lower altitude environments. For example, small UAS can fly at very low altitudes, on the order of tens of meters or less, and hence buildings, trees and other objects can obstruct the LOS signal.

- Investigation of the performance degradation incurred when using FBMC through a non-linear channel, e.g., the non-linearity caused by a transmitter power amplifier. Such an effect is known to raise spectral sidelobes, so quantification of this, and comparison with CP-OFDM, is of interest.
- Further development of adaptive FBMC schemes that can operate in *both* the L- and C-bands, either alternately or simultaneously.
- Investigation of FBMC systems that dynamically change the number of subcarriers, to manage peak-to-average power ratio, channel dispersion, and throughput. Development of companion receiver equalizers—with relatively low complexity—for some of these schemes.
- Investigation of finite precision arithmetic on FBMC performance.
- Investigation of single – carrier frequency-division multiplexing (SC-FDMA) technique in RL AG communication systems to reduce the PAPR and power consumption.
- Doppler shift and spread analysis in CP-OFDM and FBMC based AG communication systems.

REFERENCES

[1] Broadband VHF Aeronautical Communications System based on MC-CDMA (Jan 2004) [Online]. Available: http://www.b-vhf.org.

[2] M. Schnell *et al.*, “B-AMC - broadband aeronautical multi-carrier communications,” *2008 Integrated Communications Navigation and Surveillance Conference* (*ICNS*), pp. 1-12, Bethesda, MD, 5-7 May 2008.

[3] H. Jamal, D. W. Matolak, R. Sun, “Comparison of L-DACS and FBMC performance in over-water air-ground channels,” *Proc. IEEE/AIAA 34th Digital Avionics Systems Conference (DASC)*, pp. 2D6-1, Prague, Czech Republic, 13-17 Sept. 2015.

[4] H. Jamal, D.W. Matolak, “FBMC and LDACS Performance for Future Air to Ground Communication Systems," *IEEE Transactions on Vehicular Technology*, vol. 66, no. 99, pp. 5043-5055, June 2017.

[5] R. Chang, “High-speed multichannel data transmission with bandlimited orthogonal signals,” *Bell Sys. Tech. J.*, vol. 45, pp. 1775-1796, Dec. 1966.

[6] B. Saltzberg, “Performance of an efficient parallel data transmission system,” *IEEE Trans. on Comm. Tech.*, vol. 15, no. 6, pp. 805-811, Dec. 1967.

[7] ITT Industries, “Technology Assessment for the Future Aeronautical Communications System,” NASA/CR-2005-213587, TR04055, Reston, VA, May 2005.

[8] IEEE Standards Association, IEEE 802.16, website: http://standards.ieee.org/getieee802/802.16.html, 2 March 2017.

[9] Radio Technical Commission for Aeronautics (RTCA) Special Committee (SC) 223, “AeroMACS System Requirements Document,” edition 1.0, 9 February 2010.

[10] P. Wang, Y. Li, L. Song, B. Vucetic. “Multi-Gigabit Millimeter Wave Wireless Communications for 5G: From Fixed Access to Cellular Networks,” *IEEE Comm. Mag*., vol. 53, no. 1, pp. 168-178, January 2015.

[11] N. Neji, R. de Lacerda, A. Azoulay, T. Letertre and O. Outtier "Survey on the Future Aeronautical Communication System and Its Development for Continental Communications," *IEEE Trans. Vehicular Tech.*, vol. 62, no. 1, pp. 182,191, Jan. 2013.

[12] Eldredge, Leo, et al. “Alternative Positioning, Navigation & Timing (PNT) Study.” *International Civil Aviation Organisation Navigation Systems Panel (NSP), Working Group Meetings, Montreal, Canada*. 2010.

[13] M. Sajatovic, B. Haindl, M. Ehammer, Th. Gräupl, M. Schnell, U. Epple, and S. Brandes, “L-DACS1 System Definition Proposal: Deliverable D2,” Tech. Rep., Eurocontrol, Issue 1.0, Feb 2009.

[14] N. Fistas, “L-DACS2 System Definition Proposal: Deliverable D2,” Tech. Rep., Eurocontrol, Issue 1.0, Brussels, Belgium, Dec 2009.

[15] S. Brandes, et al. “Physical layer specification of the L-band Digital Aeronautical Communications System (L-DACS1).” *Integrated Communications, Navigation and Surveillance Conference (ICNS), IEEE*, pp. 1-12, Arlington VA, 13-15 May 2009.

[16] G. Snjezana, M. Schnell, and U. Epple. “The L-DACS1 physical layer design,” *INTECH Open Access Publisher*, 2011.

[17] M. Schnell, F. Nico, and G. Snjezana. “L-DACS1 laboratory demonstrator development and compatibility measurement set-up.” *Proc. IEEE/AIAA 29th Digital*

Avionics Systems Conference (*DASC*), pp. 3.E.3-1 - 3.E.3-11, Salt Lake City, UT, 3-7 Oct 2010.

[18] N. Franzen, A. Alexander, and M. Schnell. "L-DACS1 physical layer laboratory demonstrator." *Integrated Communications Navigation and Surveillance Conference* (*ICNS*)*, IEEE*, pp. A2-1 - A2-11, Herndon VA, 11-13 May 2010.

[19] R. Jain, T. Fred, and Y. Kwong-Sang. "Analysis of l-band digital aeronautical communication systems: L-dacs1 and l-dacs2." *IEEE Aerospace Conference*, pp. 1–10, Big Sky, MT, 5-12 March 2011.

[20] N. Neji, et al. "Effect of the aeronautical L-DACS2 radio-frequency signals on the DME system performance." *Vehicular Technology Conference Fall* (*VTC* 2010-Fall), *IEEE*, pp. 1-5, Ottawa, ON, 6-9 Sept 2010.

[21] R. Jain, and F. Templin, "Requirements, challenges and analysis of alternatives for wireless datalinks for unmanned aircraft systems," *IEEE Journal on Selected Areas in Communications,* vol. 30, no. 6, pp. 852–860, June 2012.

[22] U. Epple, et al. "Receiver optimization for L-DACS1." *Proc. IEEE/AIAA 28th Digital Avionics Systems Conference (DASC)*, pp. 4.B.1-1 - 4.B.1-12, Orlando, FL, 23-29 Oct 2009.

[23] S. Brandes, E. Ulrich, and M. Schnell, "Compensation of the impact of interference mitigation by pulse blanking in OFDM systems." *Global Telecommunications Conference, IEEE*, pp. 1-6, Honolulu, HI, Nov. 30 2009-Dec. 4 2009.

[24] E. Haas, H. Lang and M. Schnell, "Development and implementation of an advanced airport data link based on multi-carrier communications," *IEEE Seventh International Symposium on Spread Spectrum Techniques and Applications*, pp. 373-379 vol.2, 2002.

[25] R. D. Apaza, "Next Generation Airport Surface Communications," workshop, 5th *Integrated Comm., Nav., & Surveillance Conf.,* Fairfax, VA, 2-5 May 2005.

[26] G. Bartoli, R. Fantacci, D. Marabissi, "AeroMACS: A new perspective for mobile airport communications and services," *IEEE Wireless Communications*, vol. 20, no. 6, pp. 44-50, December 2013.

[27] RTCA, "Aeronautical Mobile Airport Communications System (AeroMACS) Profile," RTCA DO-345, December 2013.

[28] R. J. Kerczewski, R. D. Apaza, R. P. Dimond, "AeroMACS System Characterization and Demonstrations," *NASA Technical Report*, NASA/TM-2013-216497, March 2013.

[29] Wikipedia, "Aircraft Communications Addressing and Reporting System," (2015, June 22). [Online]. Available: en.wikipedia.org/wiki/Aircraft_Communications_Addressing_and_Reporting_System.

[30] Wikipedia, "VHF Data Link," (2015, June 22). [Online]. Available: en.wikipedia.org/wiki/VHF_Data_Link.

[31] European Telecommunications Standards Institute (ETSI), "VHF air-ground Digital Link (VDL) Mode 2; Technical characteristics and methods of measurement for ground-based equipment; Part 1: Physical layer and MAC sub-layer," *ETSI EN 301 841-1 V1.3.1 Final draft*, Jan. 2010.

[32] Broadband VHF, (2015, June 22). [Online]. Available: www.b-vhf.org/.

[33] EUROCONTROL, (2015, June 22). [Online]. Available: www.eurocontrol.int/.

[34] Wikipedia, "Automatic dependent surveillance – broadcast," (last edited on 21 July 2017). [Online]. Available: https://en.wikipedia.org/wiki/Automatic_dependent_surveillance_–_broadcast

[35] G. Dyer, J. Budinger, “FCS Technology Assessment Team: Technology Assessment Phase II – P34 Overview,” (2015, June 22). [Online]. Available: www.icao.int/safety/acp/Inactive%20working%20groups%20library/ACP-WG-C-11/ACP-WGC11-WP31-P34_Overview.ppt.

[36] Wikipedia, “Distance measuring equipment” (last edited on 17 April 2017). [Online]. Available: https://en.wikipedia.org/wiki/Distance_measuring_equipment

[37] Aeronautical Communications Panel (ACP), “B-AMC — A Promising Future Aeronautical Communications System Based Multi-carrier Technology,” (2015, June 22). [Online]. Available: www.icao.int/safety/acp/prl/ACP-1-ENGLISH/ACP.1.IP.008.1.en.doc.

[38] L-DACS1 System Design Proposal: Deliverable D3 - Design Specifications for L-DACS1 Prototype, (2015, June 22). [Online]. Available: www.eurocontrol.int/sites/default/files/article/content/documents/communications/01042009-ldacs1-d3-v10.pdf.

[39] N. Neji, R. de Lacerda, A. Azoulay, T. Letertre, and O. Outtier, “Survey on the Future Aeronautical Communication System and Its Development for Continental Communications,” *IEEE Transactions on Vehicular Technology*, vol. 62, no. 1, pp. 182–191, Jan. 2013.

[40] L-DACS2 Transmitter and Receiver prototype equipment specifications: Deliverable D3, (2015, June 22). [Online]. Available: www.eurocontrol.int/sites/default/files/article/content/documents/communications/18062009-ldacs2-design-d3-v1.2.pdf.

[41] Microwave Landing System, (2015, June 22). [Online]. Available: www.microwave.landingsystem.com.

[42] Radio Technical Commission for Aeronautics (RTCA) Special Committee (SC) 223, "AeroMACS System Requirements Document," edition 1.0, 9 February 2010.

[43] J. M. Budinger, and E. Hall, "Aeronautical mobile airport communications system (AeroMACS)", NASA Glenn Research Center report, 2011.

[44]

[45] U. Epple, F. Hoffmann & M. Schnell, "Modeling DME interference impact on LDACS1." Proc. Integrated Communications, Navigation and Surveillance Conference (ICNS), pp. G7-1, Herndon, VA, 24-26 April 2012.

[46] S. Dhabu, A. P. Vinod, and A. S. Madhukumar. "Low complexity fast filter bank-based channelization in L-DACS1 for aeronautical communications." New Circuits and Systems Conference (NEWCAS), 2015 IEEE 13th International, pp. 1-4, Grenoble, 7-10 June 2015.

[47] L. Douzhe, W. Zhijun, "A Novel Time-Domain DME Interference Mitigation Approach for L-Band Aeronautical Communication System", IEICE TRANSACTIONS on Communications, Vol.E99-B No.5 pp.1196-1205, 2016.

[48] L. Douzhe, W. Zhijun, "DME Interference mitigation for L-DACS1 based on system identification and sparse representation", Chinese Journal of Aeronautics, 2016.

[49] Y. Xiao, J. Xie, J. Yang and T. Zhang, "A time-domain Correlative Interference Mitigation in LDACS1," 2016 Integrated Communications Navigation and Surveillance (ICNS), pp. 2D3-1-2D3-9, Herndon, VA, 2016.

[50] B. Wang, Y. Chang and H. Li, “DME interference analysis in aeronautical LTE networks,” 2016 International Conference on Wireless Communications, Signal Processing and Networking (WiSPNET), pp. 1727-1731, Chennai, 2016.

[51] Hirosaki, “An analysis of automatic equalizers for orthogonally multiplexed QAM systems,” IEEE Trans. on Communications, Jan 1980.

[52] P. P. Vaidyanathan, “Multirate Systems and Filter Banks.” Englewood Cliffs, NJ: PTR Prentice-Hall, 1993.

[53] P. Siohan, C. Siclet, N. Lacaille, “Analysis and design of OFDM/OQAM systems based on filterbank theory,” IEEE Trans. Signal Processing, vol. 50, no. 5, pp. 1170-1183, May 2002.

[54] B. Farhang-Boroujeny, “OFDM versus filter bank multicarrier.” Signal Processing Magazine, IEEE, Volume 28, Issue 3, pp. 92-112, May 2011.

[55] D. Chen, X. G. Xia, T. Jiang and X. Gao, “Properties and Power Spectral Densities of CP Based OQAM-OFDM Systems,” IEEE Trans. on Signal Processing, vol. 63, no. 14, pp. 3561-3575, July15, 2015.

[56] W. Cui, D. Qu, Tao Jiang, and B. F. Boroujeny, “Coded Auxiliary Pilots for Channel Estimation in FBMC-OQAM Systems,” IEEE Trans. on Vehicular Technology, vol. 65, no. 5, pp. 2936–2946, May 2016.

[57] Y. Zhou, T. Jiang, C. Huang, and S. Cui, “Peak-to-Average Power Ratio Reduction for OFDM/OQAM Signals via Novel Alternative Signals Method,” IEEE Trans. on Vehicular Technology, vol. 63, no. 1, pp. 494-499, Jan 2014.

[58] D. Kong, Xiang-Gen Xia, T. Jiang, and X. Gao, “Channel Estimation in CP-OQAM-OFDM Systems,” IEEE Trans. on Signal Processing, vol. 62, no. 21, pp. 5775-5786, Nov 2014.

[59] D. Chen, D. Qu, T. Jiang and Y. He, “Prototype Filter Optimization to Minimize Stopband Energy With NPR Constraint for Filter Bank Multicarrier Modulation Systems,” *IEEE Trans. on Signal Processing*, vol. 61, no. 1, pp. 159-169, Jan.1, 2013.

[60] H. Jamal, D. W. Matolak, “Performance of L-band Aeronautical Communication System Candidates in the Presence of Multiple DME Interferers,” *IEEE/AIAA 35th Digital Avionics Systems Conference* (DASC), Sacramento, CA, September, 2016. ***(Won the best session paper).***

[61] H. Jamal, D.W. Matolak, “Cognitive Spectrally Shaped FBMC for Non-Frequency-Flat L-band Aeronautical Channels," *IEEE Transactions on Vehicular Technology*.

[62] H. Jamal, D. W. Matolak, “Spectrally Shaped Filter Bank Multicarrier Systems for L-band Aeronautical Communication Systems,” *IEEE Aerospace Conference*, pp. 1-15, Big Sky, MT, 4-11 March, 2017.

[63] H. Jamal, D. W. Matolak, “Multicarrier Air to Ground MIMO Communication System Performance,” *IEEE 84th Vehicular Tech. Conference* (VTC Fall), Montréal, September, 2016.

[64] H. Jamal, D. W. Matolak, “Channel Estimation in an Over-water Air-Ground Channel Using Low Complexity OFDM-OQAM Modulations,” *IEEE Consumer Communications and Networking Conference* (CCNC), Las Vegas, NV, USA, 13-17 January, 2016.

[65] H. Jamal, D. W. Matolak “Enhanced Airport Surface Multi-carrier Communication

Systems: Filterbank Advantages over AeroMACS OFDM," *IEEE Military Communications Conference (MILCOM)*, to appear, Baltimore, MD, 2017.

[66] D. W. Matolak and R. Sun, "Air–Ground Channel Characterization for Unmanned Aircraft Systems—Part I: Methods, Measurements, and Models for Over-Water Settings," *IEEE Trans. Vehicular Tech.*, vol. 66, no. 1, pp. 26-44, Jan. 2017.

[67] R. Sun and D. W. Matolak, "Air–Ground Channel Characterization for Unmanned Aircraft Systems Part II: Hilly and Mountainous Settings," *IEEE Trans. Vehicular Tech.*, vol. 66, no. 3, pp. 1913-1925, March 2017.

[68] D. W. Matolak and R. Sun, "Air–Ground Channel Characterization for Unmanned Aircraft Systems—Part III: The Suburban and Near-Urban Environments," *IEEE Trans. Vehicular Tech.*, vol. 66, no. 8, pp. 6607-6618, Aug. 2017.

[69] D. W. Matolak and R. Sun, "Air-Ground Channel Characterization for Unmanned Aircraft Systems: The Hilly Suburban Environment," *Vehicular Technology Conference (VTC-Fall)*, pp. 1-5, Vancouver, BC, 2014.

[70] D. W. Matolak, R. Sun, "AG Channel Measurement & Modeling Results for Over-Water and Hilly Terrain Conditions," (Report #7) NASA Grant #NNX12AR56G, 26 September 2014.

[71] R. J. Kelly and D. R. Cusick, "Distance Measuring Equipment in Aviation," *Advances in electronics and electron physics, Academic Press*, Vol. 68, New York, 1986.

[72] G. X. Gao, "DME/TACAN Interference and its Mitigation in L5/E5 Bands," *Institute of Navigation Global Navigation* (*ION*) *Satellite Systems Conference*, Fort Worth, TX, USA, September 2007.

[73] M. Mostafa, N. Franzen and M. Schnell, "DME signal power from inlay LDACS1

perspective," *2014 IEEE/AIAA 33rd Digital Avionics Systems Conference (DASC)*, pp. 3B1-1-3B1-6, Colorado Springs, CO, OCT 2014.

[74] Wikipedia, "Orthogonal frequency-division multiplexing" (last edited on 18 August 2017). [Online]. Available: https://en.wikipedia.org/wiki/Orthogonal_frequency-division_multiplexing

[75] N. R. Van and R. Prasad. *OFDM for wireless multimedia communications*. Artech House, Inc., 2000.

[76] R. Prasad, *OFDM for wireless communications systems*. Artech House, 2004.

[77] K. Murota, K. Hirade, "GMSK Modulation for Digital Mobile Radio Telephony", *IEEE Trans. on Communications*, vol. 29, no. 7, pp. 1044-1050, July 1981.

[78] P. Amini, *Filterbank multicarrier techniques for cognitive radios*. Dissertation, Department of Electrical and Computer Engineering, University of Utah, 2009.

[79] M. Bellanger, et al. "FBMC physical layer: a primer." *PHYDYAS,* no. 4, Jan 2010. [Online]. Available: http://www.ict-phydyas.org/teamspace/internal-folder/FBMC-Primer_06-2010.pdf

[80] D. W. Matolak, W. Xiong, "Spectrally-Shaped Generalized Multitone Direct-Sequence Spread Spectrum," IEEE Trans. Vehicular Tech., vol. 55, no. 4, pp. 1224-1238, July 2006.

[81] Wikipedia, "Monte Carlo method" (last edited on 8 September 2017). [Online]. Available: https://en.wikipedia.org/wiki/Monte_Carlo_method

[82] D. Qu, S. Lu and T. Jiang, "Multi-Block Joint Optimization for the Peak-to-Average Power Ratio Reduction of FBMC-OQAM Signals," *IEEE Trans. on Signal Processing*, vol. 61, no. 7, pp. 1605-1613, April1, 2013.

[83] R. Fisher. (2004, April 10). Locations of DME stations in the eastern U.S. [Online]. Available: http://www.cv.nrao.edu/~rfisher/DME/dme_sta_map.html

[84] FCC, “CFR 47 Part 90.210, Mask M,” available at: http://www.gpo.gov/fdsys/granule/CFR-2010-title47-vol5/CFR-2010-title47-vol5-sec90-210/content-detail.html

[85] M. G. Bellanger, ”Specification and design of a prototype filter for filter bank based multicarrier transmission,” *Proc. IEEE Int. Conf. Acoustics, Speech, and Signal Processing*, pp. 2417-2420, Salt Lake City, USA, May 2001.

[86] D. W. Matolak, I. Sen, W. Xiong, “The 5-GHz Airport Surface Area Channel—Part I: Measurement and Modeling Results for Large Airports,” *IEEE Trans. Vehicular Tech.*, vol. 57, no. 4, pp. 2014-2026, July 2008.

[87] Yong, Soo Cho, et al. ”MIMO-OFDM wireless communications with MATLAB.” *Singapore: John Wiley & Sons (Asia) Pte Ltd*. p.544, 2010.

[88] R. G. Gallager, Information Theory and Reliable Communication, New York: Wiley, 1968.

[89] IEEE Working Group et al., IEEE 802.22-2011(TM) Standard for Local and metropolitan area networks - Specific requirements - Part 22: Cognitive Wireless RAN Medium Access Control (MAC) and Physical Layer (PHY) specifications: Policies and procedures for operation in the TV Bands, IEEE, 2011.

[90] Y. Wang, “Cognitive radio for aeronautical air-to-ground communications,” *IEEE Aerospace and Electronic Systems Magazine*, vol. 25, no. 5, pp. 18–23, May 2010.

[91] C. Zhang, Y. Zhang, J. Xiao and J. Yu, "Aeronautical Central Cognitive Broadband Air-to-Ground Communications," *IEEE Journal on Selected Areas in Communications*, vol. 33, no. 5, pp. 946-957, May 2015.

[92] J. G. Proakis, Digital Communications, 5th Edition, McGraw-Hill Higher Education, 2007.

[93] S. M. Alamouti, "A simple transmit diversity technique for wireless communications," *IEEE Journal on Selected Areas in Communications*, vol. 16, no. 8, pp. 1451-1458, Oct 1998.

[94] X. Zhang, L. Chen, J. Qiu and J. Abdoli, "On the Waveform for 5G," *IEEE Communications Magazine*, vol. 54, no. 11, pp. 74-80, November 2016.

[95] B. Farhang-Boroujeny and H. Moradi, "OFDM Inspired Waveforms for 5G," *IEEE Communications Surveys & Tutorials*, vol. 18, no. 4, pp. 2474-2492, Fourth quarter 2016.

[96] D. W. Matolak, H. Jamal, R. Sun, "Spatial and Frequency Correlations in Two-Ray Air-Ground SIMO Channels", *IEEE International Conference on Communications* (*ICC*), Paris, France, 21-25 May 2017.

[97] C. R. Stevenson, G. Chouinard, Z. Lei, W. Hu, S. J. Shellhammer and W. Caldwell, "IEEE 802.22: The first cognitive radio wireless regional area network standard," *IEEE Communications Magazine*, vol. 47, no. 1, pp. 130-138, January 2009.

[98] B. Wang and K. J. R. Liu, "Advances in cognitive radio networks: A survey," *IEEE Journal of Selected Topics in Signal Processing*, vol. 5, no. 1, pp. 5-23, Feb. 2011.

[99] Y. C. Liang, K. C. Chen, G. Y. Li and P. Mahonen, "Cognitive radio networking and communications: an overview," *IEEE Transactions on Vehicular Technology*, vol. 60, no. 7, pp. 3386-3407, Sept. 2011.

[100] Q. Wu *et al.*, "Cognitive Internet of Things: A New Paradigm Beyond Connection," *IEEE Internet of Things Journal*, vol. 1, no. 2, pp. 129-143, April 2014.

[101] Wikipedia, "Shannon–Hartley theorem" (last edited on 2 October 2017). [Online]. Available: https://en.wikipedia.org/wiki/Shannon%E2%80%93Hartley_theorem

[102] D. M. Mielke, "C-Band Digital Aeronautical Communication for Unmanned Aircraft Systems", *to appear*, *IEEE/AIAA 36th Digital Avionics Systems Conference* (*DASC*), 17-21 September, St. Petersburg, FL, USA, 2017.